Signature Page

Final Technical Report for: Experimental Determination and Modeling-Informed Analysis of Thermo-poromechanical Response of Fractured Rock for Application to Utah FORGE

DOE Award Number:

Award Recipient Organization: University of Utah (DOE Project DE-EE0007080)

Subrecipient Organization: The University of Oklahoma (Award Number: 5-2615)

Principal Investigator: Ahmad Ghassemi, Ph.D. Geological Engineering

We certify that this report accurately reflects the outcomes of the project and complies with the reporting requirements outlined in the DOE grant agreement.

Name/Title	Signature	Date
Utah FORGE Principle Investigator	Joseph Moore	09/04/2025
DOE Program Manager		

Final Technical Report

Experimental Determination and Modeling-Informed Analysis of Thermo-poromechanical Response of Fractured Rock for Application to Utah FORGE

Award Recipient Organization: University of Utah (DOE Project DE-EE0007080)

Subrecipient Organization:
The University of Oklahoma
DUNS Identifier: 848348348
Norman, OK 73019
Award Number: 5-2615

Project Period:
10/01/2021 – 03/31/2025

Principal Investigator:
Ahmad Ghassemi
Ph.D. Geological Engineering
ahmad.ghassemi@ou.edu | 405-325-4347

Report Submitted By:
Ahmad Ghassemi
Date of Report Submission: June 30, 2025
Reporting Period: 10/01/2021 – 03/31/2025
Total Pages (excluding cover page): 90

Project Partners: None

This material is based upon work supported by the U.S. Department of Energy under Award Number DE-EE0007080.

Abstract

Final Report for Experimental Determination and Modeling-Informed Analysis of Thermo-poromechanical Response of Fractured Rock for Application to Utah FORGE

DOE Award Number:
Award Recipient Organization: University of Utah (DOE Project DE-EE0007080)
Subrecipient Organization: The University of Oklahoma (Award Number: 5-2615)

Principal Investigator: Ahmad Ghassemi, Prof.

Poromechanical and thermo-poromechanical effects are important in many reservoir rock mechanics problems. For example, when analyzing reservoir stimulation, interpretation of micro-seismicity, and interpreting diagnostic fracture interpretation test (DFIT). The project aimed to improve understanding and control of coupled thermo-poromechanical (or thermo-hydro-mechanical- THM) processes in reservoir development, and to examine the processes of hydraulic fracture closure considering the impact of temperature. The project activities consisted of measuring thermo-poroelastic properties of Utah FORGE rocks, laboratory-scale hydraulic fracturing and closure experiments in granitic rocks, and simulating wellbore and fracture response to thermo-poromechanical loading. In phase 1, we measured poroelastic properties of Utah FORGE rocks using core available from different wells. Poromechanical measurements included: (1) rock poroelastic parameters (elastic modulus and Poisson's ratio, Biot's coefficients, Skempton's B, etc.) as well as porosity and permeability. We also conducted micro-frac tests in different rock types and investigated the closure pressure in multiple injection/shut-in cycles to assess the impact of thermal stress and fracture stiffness on the G-plot. In phase 2, we extended the measurements to the realm of thermo-poroelasticity and carried out a campaign to measure/model THM opening/closure response of fractures at elevated temperatures. The measurements included temperature effects on the rock mechanical properties, temperature-dependence of poroelastic coupling coefficients (Biot's coefficient, Skempton's B, elastic moduli), as well as thermal-pore pressure coupling coefficients. We also conducted DFIT tests in heated blocks to assess the impact of THM on the closure response on the G-plot. The experimental data was used in advanced 3D thermo-poromechanical modeling to examine and to demonstrate the role of thermo-poroelasticity on wellbore fracturing and reservoir stimulation, reservoir stress redistribution, and permeability evolution in response to injection and circulation. We evaluated existing closure interpretation methods and introduced an alternative approach based on identifying early deviation on dP/dG vs. G plots. This method yielded more consistent and reliable estimates of fracture closure pressure. Our findings also indicate that the Instantaneous Shut-In Pressure (ISIP) method provides a reasonable upper-bound estimate of S_3, supporting the integrated use of ISIP and closure pressure for improved stress determination. In addition, we explored the influence of cooling on fracture behavior by conducting high-temperature laboratory DFIT experiments. In these tests, we injected cold fluid into heated and stressed fractured rock samples, and monitored pressure and temperature responses during shut-in. These tests revealed that thermal contraction from cold fluid injection lowers both fracture reopening and closure pressures, which may lead to underestimation of the minimum principal stress if not properly accounted for. This part of the study advanced the understanding of hydraulic fracture closure and stress measurements, with relevance to EGS such as Utah FORGE. Our experiments revealed the physical processes governing hydraulic fracture closure and introduced a refined method for determining closure pressure based on the initial slope deviation in the dP/dG curve. Furthermore, the results have highlighted the critical role of cooling on fracturing and stress interpretation during drilling, stimulation and circulation in EGS.

Keywords: Block-scale Hydraulic Fracturing, Biot's Effective Stress Coefficient, Closure Pressure, DFIT, Enhanced Geothermal Systems, Hydraulic Fracture, Poroelasticity, Thermal Stress, Thermo-poroelasticity, Transverse Fractures, Skempton's Pore Pressure Coefficient, Stimulation

Contents

Technical Objectives & Achievements

1. Executive Summary

1.1 Background

Coupled thermo-poromechanical processes are important in enhanced geothermal systems development because they impact pore pressure, stress and rock deformation (Ghassemi, 2010). While poroelastic properties are typically measured at room temperature, it is essential to evaluate them under actual reservoir conditions.

1.2 Project Goals and Objectives

The project goal was to improve understanding and control of coupled thermo-poromechanical (or thermo-hydro-mechanical- THM) processes in reservoir development, and to demonstrate their role in interpretations of fracturing and fracture closure process. To achieve the project goal, we have conducted advanced experiments on Utah FORGE and similar rocks to enable quantification of THM coupling in planned FORGE reservoir creation and monitoring activities, and we have elucidated (via novel laboratory micro-frac test) fracture closure process and demonstrated the role of rock cooling on closure pressure used for determination of minimum in-situ stress. Data from experiments has been used in simulation of wellbore and fracture response to thermo-poromechanical loading.

1.3 Key Findings

The poroelastic behavior of Utah FORGE granitoids demonstrates notable sensitivity to both effective stress and temperature. Biot's effective stress coefficient, α, was observed to consistently decrease with increasing effective stress, reflecting the progressive closure of microcracks and reduced deformability of the pore structure. At lower temperatures (22°C to 90°C), α displayed a more pronounced stress dependence, with values ranging from high to moderate depending on the sample. However, at elevated temperatures (140°C and above), α not only dropped to lower values but also exhibited minimal sensitivity to stress. This behavior suggests that many pore spaces had become effectively isolated and/or sealed, possibly due to thermal sealing of micro-cracks, and that the rock behaved more like a dense, intact matrix. The use of two calculation methods for α—based on the bulk modulus ratio $(1-K/Ks)$ and the poroelastic expansion coefficient (K/H)—produced consistent results, reinforcing the reliability of the observations.

Skempton's B coefficient, which measures the pore pressure response under undrained loading, showed a clear trend of reduction with both rising effective stress and temperature. Under isotropic loading, B values dropped significantly as microcracks closed and the rock matrix stiffened, limiting the rock's ability to generate pore pressure in response to external stress. At higher effective stresses, this decline became less steep, indicating that most compliant pore space had already collapsed. Temperature further amplified this effect: as samples were heated from room temperature to as high as 180°C, B values declined steadily. The thermal expansion of mineral grains is believed to tighten the microstructure, reduce crack apertures, and eliminate void connectivity, resulting in a diminished fluid pressure response. Despite careful saturation procedures—including long-duration water saturation and high back pressure to dissolve any residual air—subtle variations in microstructure (such as grain boundary characteristics and mineral alignment) contributed to sample-to-sample variability in B, especially under high stress or temperature conditions.

Permeability tests further confirmed the rock's strong sensitivity to both mechanical and thermal influences. At room temperature, permeability decreased exponentially with increasing confining pressure, consistent with the closure of pre-existing fractures and pores. Under reservoir-relevant stress conditions (20–30 MPa effective stress), samples A, C, and D generally exhibited permeabilities in the 10 to 50 micro-Darcy range, while Sample B showed substantially lower values, in the nano-Darcy range, reflecting a tighter rock matrix. When temperature was increased under constant effective stress, permeability tended to decrease, especially up to 120°C, due to thermally induced closure of fissures. Interestingly, some samples (notably A and D) showed a slight rebound in permeability at temperatures beyond 140°C, possibly due to the initiation of new thermal cracks or reconfiguration of pore pathways. This nuanced behavior highlights the complex interplay between thermal expansion, microstructural evolution, and pore connectivity in low-porosity crystalline rocks. In fractured granitoids tested, Skempton's B behavior becomes more complex when the rock is conceptualized as a dual-porosity system consisting of a compliant fracture network and a stiff rock matrix. These two domains respond differently to confining pressure changes: fractures, being much more compliant, experience a significantly higher pore pressure increase under undrained loading than the matrix. At low effective stresses, the fluid pressures in both domains tend to equilibrate due to open connectivity and minimal resistance to fluid exchange, resulting in a more unified response for the Skempton's B measurement. However, as stress increases, the pressure responses begin to diverge. The fracture domain, being more compressible, shows a disproportionately larger pressure rise, while the matrix remains relatively unresponsive. This divergence reflects the strong heterogeneity in pore compressibility across the two domains. In some cases, Skempton's B value can appear extremely high and well above 1, as it disproportionately captures the compliant domain's response. Conversely, a matrix-dominated signal would show a much lower B value. At very high temperatures, thermal overclosure can significantly reduce or even seal fracture apertures, leading to a dramatic loss of fracture porosity and permeability. In such cases, the matrix—though initially less permeable—may become the dominant flow and pressure-transmitting domain, effectively reversing the initial dual-porosity dynamics. This transformation under high-temperature, high-stress conditions highlights the importance of considering evolving microstructure and pore network architecture when interpreting Skempton's B in thermally and mechanically stressed fractured crystalline rocks.

It is also important to recognize that Skempton's B is inherently time-dependent, particularly in low-permeability and dual-porosity systems such as fractured granitoids—an effect that becomes even more pronounced when temperature is involved. Upon the application of confining pressure under undrained conditions, the initial pore pressure response (often referred to as the instantaneous or elastic B) may not reflect the true equilibrium value, especially when fluid exchange between the fracture network and the rock matrix is slow. The fracture domain, being more permeable, typically responds rapidly to stress changes, while the matrix, characterized by its tight structure and lower hydraulic diffusivity, adjusts more gradually. This mismatch leads to a transient period in which pore pressure continues to redistribute internally. With increasing temperature, the reduction in fluid viscosity can enhance pressure equilibration; however, this benefit may be counteracted by thermal closure of fractures, which restricts flow between domains. As a result, Skempton's B should not be viewed as a purely static, elastic, or intrinsic material constant, but rather as a dynamic parameter governed by the evolving interplay between pore structure, fluid flow, and measurement timing under changing thermal and mechanical conditions.

Temperature cycling tests on dry samples across a temperature range of 25–190°C revealed the rock samples exhibit varied responses to increased temperatures, some undergo thermal strengthening, others experience thermal weakening, and some remain relatively insensitive to temperature changes. All samples show a decline in permeability with increasing temperature, and drained bulk moduli generally increase with temperature and, for some samples, become less sensitive to effective stress due to the closure of micro-fissures upon heating. The underlying mechanisms governing permeability changes and the thermal strengthening or weakening effects observed in these granitoids have been explored, providing critical insights into their thermo-poroelastic behavior and implications for geothermal reservoir performance.

Micro-frac tests in different rock types were used to investigate the closure pressure in multiple injection/shut-in cycles replicating behaviors frequently noticed during fracture closure analysis in field-scale hydraulic fracturing tests such as non-ideal leakoff and the underestimation of minimum principal stress by the "tangent" method, and the absence of consistent signatures for determining fracture closure via the "compliance" method. The experimental results were also used to investigate the physical process of fracture closure during shut-in. Our findings show that fracture closure during shut-in follows a three-stage process. Initially, in Stage 1, the fracture closes in a "hinge-like" manner, where the fracture width decreases while the fracture radius remains constant, indicating that no contact between the fracture surfaces at this stage. In Stage 2, fracture closure progresses from the fracture tip towards the wellbore in a "zipper-like" manner, as fluid pressure within the fracture declines. Finally, in Stage 3, the fracture reaches full hydraulic closure, with fluid predominantly leaking through the wellbore wall. The wellbore pressure at the end of Stage 1 or the onset of Stage 2 marks the onset of mechanical fracture closure and provides a reliable estimate of the minimum principal stress. The net changes of pressure decline rate, governed by the complex competing process, determine the characteristics of G-function plots, resulting in various possible shapes and features of these plots, as illustrated in our experimental study.

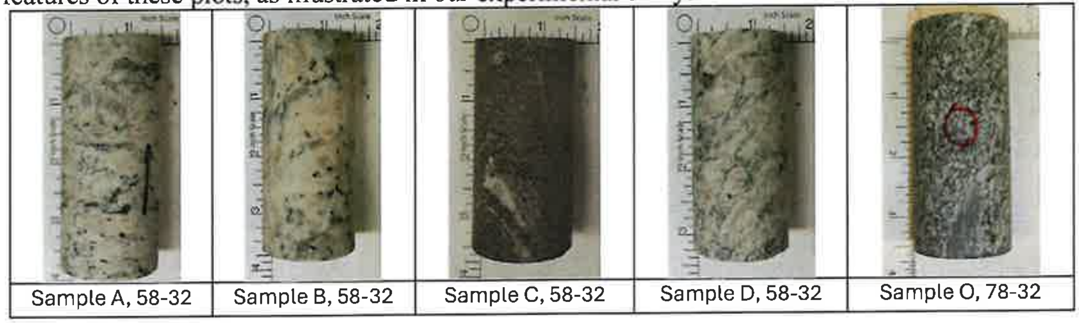

Sample A, 58-32	Sample B, 58-32	Sample C, 58-32	Sample D, 58-32	Sample O, 78-32

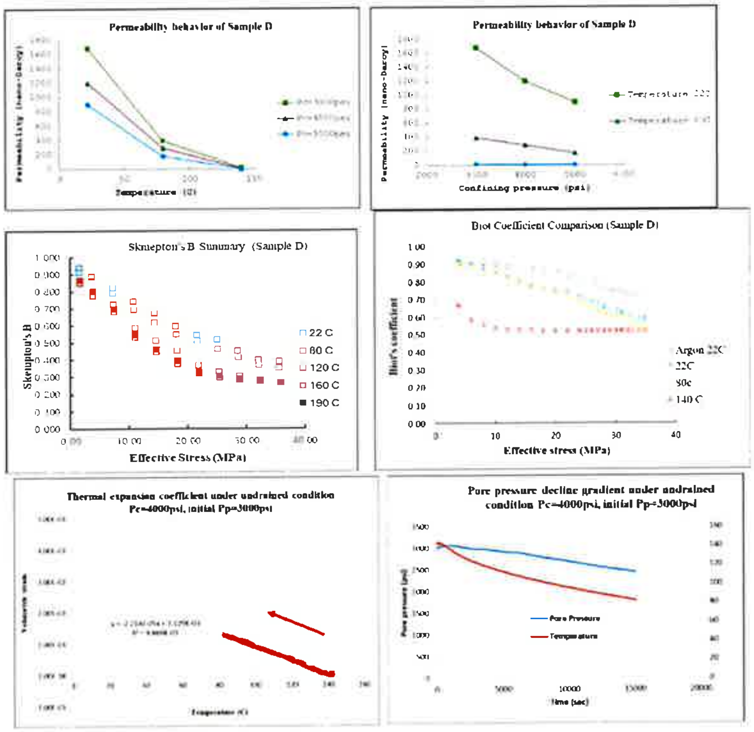

Figure 1. Images of some samples tested in this work (top). Permeability as a function of pressure and temperature. This indicates crack closure and impacts poroelastic properties at elevated temperatures and pressures (middle row): Biot's effective stress coefficient and Skempton's pore pressure coefficient for Sample D from Well 58-32 at 22, 50, 90, 140 C. Bottom row: left: during sample's cooling stage (under a confining pressure of 4000 psi and an initial pore pressure of 3000 psi under an undrained condition, the vol. thermal expansion coefficient was evaluated as $2.214\text{x}10^{-05}$/°C; the pore pressure decline gradient is evaluated as 0.1178 MPa/°C.

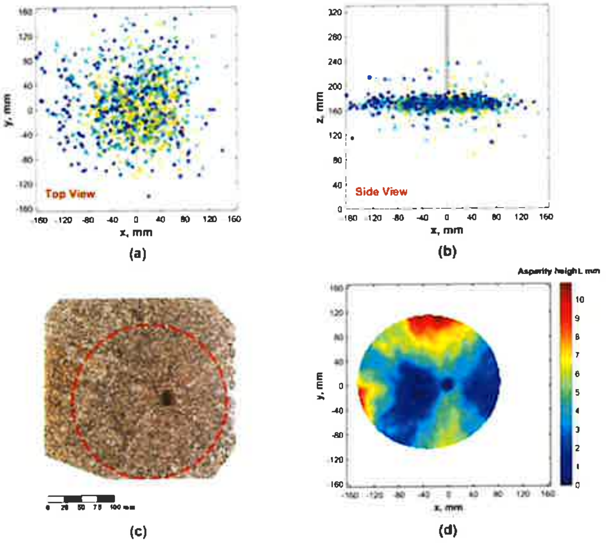

Figure 2. Data from a hydraulic fracturing experiment 1 on Sierra White Granite: (a) and (b) show the top view and side view of Acoustic Emission (AE) events during the fracture initiation and propagation cycles, with yellow dots indicating AE events from the initiation cycle, and cyan and blue dots representing those from the first and second propagation cycles, respectively; (c) depicts the lower portion of the fracture, revealed after trimming and splitting the tested granite block; and (d) is the topographical details of the hydraulic fracture obtained through surface scanning.

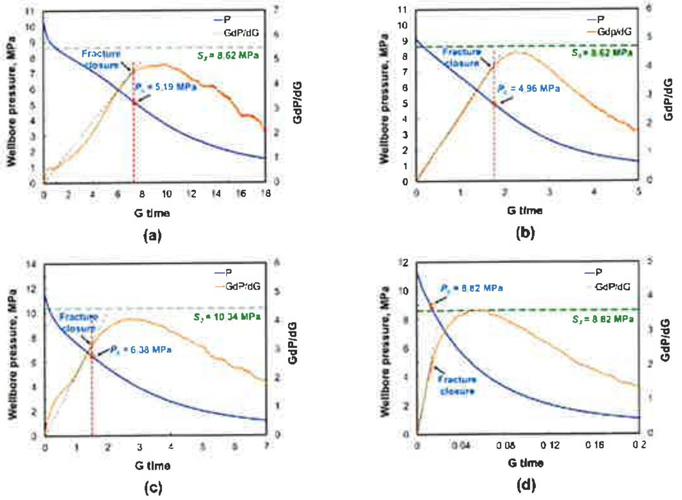

Figure 3. Determination of the fracture closure pressure through the "tangent" method for: (a) Experiment 1 (E1) on Sierra White Granite with mineral oil as the injection fluid; (b) Experiment 2 (E2), also on Sierra White Granite, but with water injection; (c) Experiment 3 (E3) on Crab Orchard Sandstone using oil as the injection fluid; and (d) Experiment 4 (E4) on Scioto Sandstone, utilizing water for injection. E1, E2, and E3 present non-ideal leak-off features with multiple slope deviations, while E4 shows normal leak-off behavior. The green dashed line represents the applied minimum principal stress, serving as the reference stress level for the analysis.

Based on the insights gained from our experimental work, we propose using an early slope change on a dP/dG vs. G curve that deviates from a linear trend for fracture closure identification. Furthermore, our experimental findings suggest that instantaneous shut-in pressure (ISIP) could provide reasonable, albeit higher bound, estimates of the minimum principal stress.

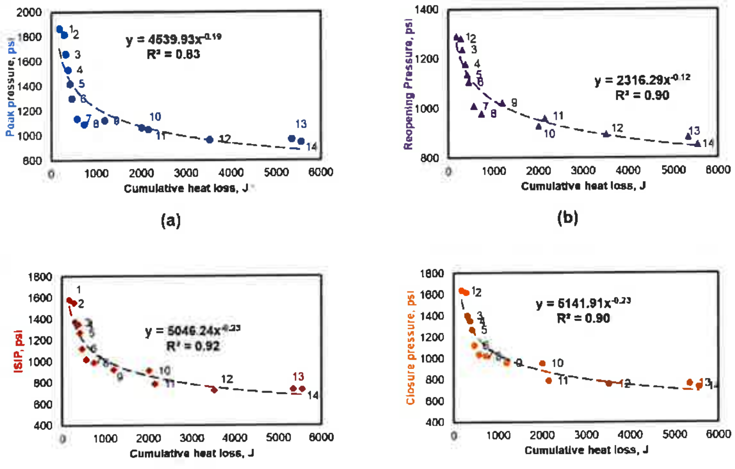

(a)

(b)

(c)

(d)

Figure 4. The relationship between pressure indicators and cumulative heat loss during high temperature DFIT tests of a cuboid Sierra White Granite. (a) peak injection pressure vs. cumulative heat loss; (b) fracture reopening pressure vs. cumulative heat loss; (c) *ISIP* vs. cumulative heat loss; (d) fracture closure pressure vs. cumulative heat loss.

We also focused on investigating the response of Utah FORGE rocks and Sierra White granite to heating and cooling cycles using static and dynamic measurements with AE monitoring and found different types of rocks exhibit different behaviors. While some show thermal strengthening, others exhibit a slight thermal weakening. Understanding these microstructural mechanisms is crucial for predicting the behavior of geothermal reservoirs under thermal cycling conditions. The data will be elaborated on in the final technical report.

Extensive thermo-poromechanical modeling was also performed as part of the project to help determine important properties to be measured as well as to investigate the impact of coupling in stimulation as well as in DAS interpretation of fracturing. A thermo-poroelastic displacement discontinuity (DD) method (for fracture opening and ride, fluid and heat diffusion in the reservoir matrix) coupled with a finite element method (for the fluid and heat convection and conduction inside the fractures) was utilized. The fracture response to pressurization and cooling during stimulation and circulation processes was simulated and analyzed. It was observed that for a net stress loading (mode I), crack opens with applied load, and for a pore pressure increase (mode II) crack closes due to the induced back stress caused by pore pressure diffusion. Cooling of the fracture (mode III) significantly increases the aperture depending on the rock thermal properties, the temperature difference, and time. The results indicated that although for shorter injection times, mode I induced stresses are dominant, during long term injection/extraction operations, cooling effects become much more significant when compared to applied mode I and mode II loadings. These stress variations potentially lead to transient deformations and failure and induced micro-seismic events as shown in (Ghassemi and Tao, 2016; Safari and Ghassemi, 2015). In addition, the results suggest that in FORGE stimulation where multiple cycles of injection are implemented both the poroelastic and thermoelastic effects occur and their impact on interpretations needs to be considered. These effects will likely play a more predominant role during multiple injection/flowback and circulation operations. Our results also show the impact of temperature on viscosity and density can also become significant in some circumstances.

3. Theoretical Framework and Methodology

3.1 Overview of Poroelasticity and Thermo-Poroelasticity Theory

3.1.1. Poroelasticity

Poroelasticity describes the mechanical behavior of fluid-saturated porous rocks, where the deformation of the solid matrix is coupled with fluid flow within the pores. This theory is essential for understanding the response of geothermal reservoirs, as changes in stress, pressure, and temperature influence both rock deformation and fluid movement. The concept of poroelasticity is particularly significant in enhanced geothermal systems (EGS), where fluid injection and extraction alter the stress state and permeability of the reservoir rock. Biot (1941, 1955) developed the foundational theory of poroelasticity. Biot's theory states that the total stress applied to a porous medium is shared between the solid matrix and the pore fluid, with the degree of coupling described by Biot's effective stress coefficient (α). This coefficient defines how much of the applied stress is transferred to the pore fluid and is given by:

$$\alpha = 1 - \frac{K_d}{K_S} \qquad (3.1)$$

where K_d is the bulk modulus of the dry rock or drained bulk modulus, and K_s is the bulk modulus of the solid grains. A Biot's coefficient close to 1 indicates that most of the applied stress is carried by the fluid, while a value close to zero suggests that the rock matrix bears most of the load.

Another key parameter in poroelasticity is Skempton's coefficient (B), which quantifies the pore pressure response to an applied stress under undrained conditions. It is defined as:

$$B = \frac{\Delta P_P}{\Delta\sigma} \qquad (3.2)$$

where ΔP_P is the change in pore pressure and $\Delta\sigma$ is the applied mean stress. This parameter is crucial for understanding fluid pressure buildup during injection or production in geothermal reservoirs. B and α are related by the following equation with Ku as the undrained bulk modulus.

$$\alpha = \frac{K_u - K}{BK_u} \qquad (3.3)$$

3.1.1 Governing Equations (Stress-Strain Relationships, Fluid Flow Coupling)

Poroelasticity is governed by a set of coupled equations that describe the mechanical deformation and fluid flow within the porous rock (see Cheng, 2016 for full details) rock. According to Biot's theory, the porous medium is composed of a solid matrix and a fluid phase, both of which interact under mechanical loading. The governing equations that link the deformation of the solid matrix to the pore pressure of the fluid include:

- *Stress-Strain Relationship (Mechanical Deformation)*

The poroelastic constitutive equations extend Hooke's law by incorporating pore pressure effects:

$$\sigma_{ij} - \alpha p\delta_{ij} = C_{ijkl}\varepsilon_{kl} = 2Ge_{ij} + \frac{3K-2G}{3} e\delta_{ij} \qquad (3.4)$$

$$\zeta = \alpha\varepsilon_{kk} + \frac{1}{M} p \qquad (3.5)$$

$$K = K_u - a^2 M \qquad (3.6)$$

where σ_{ij} is the stress tensor in the solid phase, C_{ijkl} is the stiffness tensor (elastic moduli), ε_{kl} is the strain tensor, p is the pore pressure, α is Biot's coefficient, B is Skempton's B coefficient, ζ is the water content, δ_{ij} is the Kronecker delta, K is the bulk modulus, and G is the shear modulus, M is the Biot's modulus.

These equations highlight how pore pressure contributes to the overall stress state of the material, influencing deformation and potential failure mechanisms in geothermal formations.

- *Fluid Flow Equation (Darcy's Law and Mass Conservation)*

Fluid flow in a porous medium follows Darcy's law, which relates the fluid velocity to the pressure gradient:

$$q = -\frac{k}{\mu} \nabla p \qquad (3.7)$$

where:

- q is the Darcy velocity, representing the fluid flux,

- k is the permeability of the rock,

- μ is the fluid viscosity, and

- ∇p is the pore pressure gradient driving the flow.

Combining Darcy's law with the mass conservation equation for a compressible fluid results in the governing equation for fluid flow in a poroelastic medium.

3.1.2 Thermo-Poroelasticity

Thermo-poroelasticity extends poroelastic theory by incorporating the effects of temperature changes on fluid-saturated porous media. In many geological and engineering applications, such as geothermal reservoirs, petroleum extraction, and underground waste storage, thermal effects significantly influence both fluid flow and mechanical deformation of the solid matrix. The constitutive equations including thermal effects are shown in the following (Cheng, 2016):

$$\sigma_{ij} = 2Ge_{ij} + \delta_{ij}(K\varepsilon_{kk} - \alpha p - \beta K T) \qquad (3.8)$$

$$\zeta = \alpha\varepsilon_{kk} + \frac{1}{M} p + \beta_f \, T \qquad (3.9)$$

$$s = \beta K \varepsilon_{kk} + \beta_f p + \frac{C}{T_0} T \qquad (3.10)$$

$$\Lambda = \frac{a-\phi}{K_s} \beta + \phi\beta_f - \beta = \frac{\Delta p}{\Delta T} \qquad (3.11)$$

In which T is the Temperature change (from reference T_0), β is the linear thermal expansion coefficient of the solid matrix, and β_f is the thermal expansion coefficient of the fluid, C is the volumetric heat capacity of the saturated medium, s refers to the entropy change (thermodynamic coupling), and Λ is the undrained thermal pressurization coefficient.

Table 3.1. Key Differences Between Poroelasticity and Thermal-Poroelasticity.

Feature	Poroelasticity	Thermal-Poroelasticity
Governing Variables	Includes only mechanical and pore pressure effects	Includes additional thermal expansion terms
Constitutive Law	Stress depends on strain and pore pressure	Stress also affected by thermal expansion of fluid and matrix
Fluid Flow	Darcy's law (∇p only)	Modified Darcy's law ($\nabla p - \beta_f \nabla T$)
Additional Physics	None	Heat transport (Fourier's law, energy balance)
Applications	Hydraulic fracturing, reservoir compaction, fluid-induced deformation, induced seismicity	geothermal reservoirs, thermal recovery, nuclear waste disposal, thermal fracturing

Overall, thermo-poroelasticity provides a comprehensive framework for understanding the coupled effects of thermal, hydraulic, and mechanical processes in fluid-saturated porous media. Properly accounting for these effects is crucial for the safe and efficient operation of geothermal reservoirs, petroleum extraction, and other subsurface energy applications.

3.1.3 Dual Porosity Medium

Naturally fractured rock was firstly characterized by Warren and Root (1963) as a dual-porosity model in their study of reservoir flow, since micro-cracks and fine fissures are often naturally present in rock samples at both mesoscale and small scale, causing the rock to possess characteristics as a multi-porosity material. As a commonly used conceptual model to handle the condition of the multi-porosity, the "dual-porosity" model characterizes the fractured rock as two completely overlapping continua, one representing the fractures and the other representing the porous matrix (Barenblatt et al., 1960). A dual porosity medium represents a fractured rock system where two distinct types of porosity coexist: the matrix porosity and the fracture porosity. The rock matrix consists of low-permeability regions that store the majority of the fluid, whereas the fractures provide highly permeable pathways that allow rapid fluid flow. This concept is particularly relevant in reservoirs such as naturally fractured formations, geothermal reservoirs, and unconventional shale plays, where the matrix and fracture domains exhibit vastly different transport properties. The behavior of such systems is governed by fluid exchange between the matrix blocks and fractures. The Warren and Root (1963) model is widely used to describe dual-porosity systems, where the matrix primarily acts as a storage domain and transfers fluid to the fractures, which serve as the primary flow paths to production wells. The interaction between these two domains is characterized by inter-porosity flow, which depends on pressure gradients and rock properties.

Fluid movement in a dual-porosity system occurs through two key mechanisms:

1. Inter-porosity (Matrix-to-Fracture) Flow: The exchange of fluid between the matrix and fractures due to pressure gradients. This is controlled by matrix permeability, block size, and capillary effects.
2. Fracture Network Flow: The bulk movement of fluid through the interconnected fracture system, which is typically orders of magnitude faster than matrix diffusion.

Three primary flow regimes characterize dual porosity systems:

1. Fracture-dominated flow: At early times, fluid flows primarily within the highly permeable fracture network, with minimal contribution from the matrix.
2. Transition flow: As the pressure differential between the matrix and fractures increases, fluid starts transferring from the matrix into the fractures.
3. Matrix-dominated flow: At later times, as fractures deplete, the matrix becomes the primary contributor to production, governed by slow diffusion.

2.3.1 Governing Equations for Dual Porosity Systems
A dual-porosity system is typically modeled using two coupled mass balance equations, one for the matrix and one for the fractures, with an exchange term linking them.

1. *Continuity Equation for Fracture System*

$$\phi_f \frac{\partial p_f}{\partial t} + \nabla \cdot \left(\frac{k_f}{\mu} \nabla p_f\right) = \frac{\S}{\tau}\left(p_m - p_f\right) + q_f \qquad (3.12)$$

where ϕ_f is fracture porosity, k_f is fracture permeability, p_f is fracture pressure, μ is the fluid viscosity, § is the shape factor controlling matrix-fracture interaction, τ is the characteristic time for pressure equilibration, and q_f refers to an external source/sink term.

2. *Continuity Equation for Matrix System*

$$\phi_m \frac{\partial p_m}{\partial t} = \frac{\S}{\tau}\left(p_f - p_m\right) \qquad (3.13)$$

where ϕ_m is matrix porosity, and p_m is matrix pressure.

3. *Fluid Exchange Term (Inter-porosity Flow)*

$$q_{mf} = \frac{\S}{\tau}\left(p_m - p_f\right) \qquad (3.14)$$

which controls the rate of pressure equilibration between the matrix and fractures. The shape factor § depends on the geometry of the matrix blocks.

These equations describe the fluid mass balance within each domain and the pressure-driven interaction between the matrix and fractures. The system is solved numerically or analytically depending on boundary conditions and external influences. Flow regimes in dual porosity systems cover early time (fluid flows only in fractures; matrix is stagnant), transitional (matrix begins feeding fractures); and late time (pressure equilibrates between matrix and fractures).

3.1.4. Methodology for dual porosity medium characterization

Although the governing equations provide the theoretical foundation for dual-porosity media, certain parameters, such as the shape factor, are challenging to measure or determine through laboratory testing. Therefore, it is necessary to develop a methodology that enables the characterization of fractured rock samples using practical and feasible laboratory testing approaches. To investigate a dual porosity medium, we need to start with a single porosity medium. For a single porosity porous medium (rock matrix without fractures) (Figure 3.1), the poroelastic constitutive equations are (Wang, 2000):

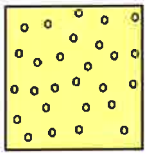

Figure 3.1. Single porous medium I.

$$\begin{pmatrix} \delta\varepsilon \\ \delta\zeta^{(I)} \end{pmatrix} = \begin{pmatrix} a_{11} & a_{12} \\ a_{12} & a_{22} \end{pmatrix} \begin{pmatrix} \delta p_c \\ \delta p_f^{(I)} \end{pmatrix} \qquad (3.15)$$

where ε is the volumetric strain, p_c is the confining pressure, $\zeta^{(I)}$ is the increment of fluid content in the porosity of the whole domain of concern, and $p_f^{(I)}$ is the pore pressure. Superscript *(I)* indicates that this is the medium *I*, which can be distinguished from another material *II* in the next step. From the standpoint of a laboratory test, the strain and pressure (either pore pressure or confining pressure) can all be measured with relatively high accuracy, while the pore fluid content (volume change in the order of 0.1 ml or even less) is difficult to measure, or the accuracy is low due to fluid compressibility in response to the different pressure conditions. However, a boundary condition of undrained condition ($\zeta^{(I)} = 0$) can be easily set.

For a drained jacketed hydrostatic compression test where the pore pressure is maintained constant:

$$a_{11} = \left.\frac{\delta\varepsilon}{\delta p_c}\right|_{\delta pf=0} = \frac{1}{K^{(I)}} \quad > \quad 0 \qquad (3.16)$$

where $K^{(I)}$ is the drained bulk modulus of this rock material *I.*

For a fluid depletion test under a constant confining pressure but with pore pressure variation, there is

$$a_{12} = \left.\frac{\delta\varepsilon}{\delta p_f}\right|_{\delta pc=0} = \frac{1}{H^{(I)}} \quad < \quad 0 \qquad (3.4.3)$$

H is called poroelastic expansion coefficient (Wang, 2000). For an undrained test with $\delta\zeta^{(I)}=0$, there is

$$B^{(I)} = \left.\frac{\delta p_f^{(I)}}{\delta p_c}\right|_{\delta\zeta=0} = -\frac{a_{12}}{a_{22}} \quad \rightarrow \quad a_{22} = -\frac{a_{12}}{B^{(I)}} = -\frac{1}{H^{(I)}B^{(I)}} \qquad (3.17)$$

where $B^{(I)}$ is Skempton's B coefficient of this single porosity material.

For an unjacketed test with $p_f^{(I)} = p_c$, there is:

$$a_{11} + a_{12} = \left.\frac{\delta\varepsilon}{\delta p_c}\right|_{\delta pf=\delta pc} = \frac{1}{K_s^{(I)}} \quad > \quad 0 \quad \rightarrow \quad a_{12} = \frac{1}{K_s^{(I)}} - \frac{1}{K^{(I)}} \qquad (3.18)$$

There is also the following equation under an undrained condition:

$$\frac{1}{K_u^{(I)}} \equiv \left.\frac{\delta\varepsilon}{\delta p_c}\right|_{\delta\zeta=0} = a_{11} + a_{12}\frac{\delta p_f^{(I)}}{\delta p_c} = a_{11} + a_{12}B^{(I)} \qquad (3.19)$$

In which $K_u^{(I)}$ is the undrained bulk modulus of this material. Thus, for a single porosity medium, we need to measure its *K, Ks, B, H* in order to establish this matrix as follows:

$$\begin{pmatrix} \delta\varepsilon \\ \delta\zeta^{(I)} \end{pmatrix} = \begin{pmatrix} a_{11} & a_{12} \\ a_{12} & a_{22} \end{pmatrix} \begin{pmatrix} \delta p_c \\ \delta p_f^{(I)} \end{pmatrix} = \begin{pmatrix} \dfrac{1}{K^{(I)}} & \dfrac{1}{K_s^{(I)}} - \dfrac{1}{K^{(I)}} \\ \dfrac{1}{K_s^{(I)}} - \dfrac{1}{K^{(I)}} & \dfrac{\dfrac{1}{K_s^{(I)}} - \dfrac{1}{K^{(I)}}}{B^{(I)}} \end{pmatrix} \begin{pmatrix} \delta p_c \\ \delta p_f^{(I)} \end{pmatrix} \tag{3.20.1}$$

$$= \begin{pmatrix} \dfrac{1}{K^{(I)}} & \dfrac{1}{H^{(I)}} \\ \dfrac{1}{H^{(I)}} & -\dfrac{1}{H^{(I)}B^{(I)}} \end{pmatrix} \begin{pmatrix} \delta p_c \\ \delta p_f^{(I)} \end{pmatrix} \tag{3.20.2}$$

$$= \begin{pmatrix} \dfrac{1}{K^{(I)}} & \dfrac{\dfrac{1}{K_u^{(I)}} - \dfrac{1}{K^{(I)}}}{B^{(I)}} \\ \dfrac{\dfrac{1}{K_u^{(I)}} - \dfrac{1}{K^{(I)}}}{B^{(I)}} & \dfrac{\dfrac{1}{K^{(I)}} - \dfrac{1}{K_u^{(I)}}}{(B^{(I)})^2} \end{pmatrix} \begin{pmatrix} \delta p_c \\ \delta p_f^{(I)} \end{pmatrix} \tag{3.20.3}$$

Note other quantities such as Biot's coefficient (α) which is derived from the measured moduli are not the primary quantities as *K, Ks, Ku, H, B* in the sense that these quantities are directly measurable from a lab test. Also note that in the above equation, the solution is present in three forms (3.20.1-3.20.3) with different sets of parameters, with one set of *K, Ks* and *B* for Equation 3.20.1, one set of *K, H* and *B* for Equation 3.20.2, and the other set of *Ku, K,* and *B* for Equation 3.20.3. Note the set based on *K, H, B* gives the most concise form (3.20.2). This is actually also the simplest form when considering the dual porosity scenario. Currently, our technique to measure *K, Ks, H, B* is mature for a homogeneous rock, thus the equation for a single porosity material can be well established. Similarly, for another single porosity medium *II* (Figure 3.2), the constitutive equation is the following (only one form of solution is present for brevity):

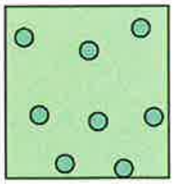

Figure 3.2. Single porous medium II.

$$\begin{pmatrix} \delta\varepsilon \\ \delta\zeta^{(II)} \end{pmatrix} = \begin{pmatrix} \dfrac{1}{K^{(II)}} & \dfrac{1}{H^{(II)}} \\ \dfrac{1}{H^{(II)}} & -\dfrac{1}{H^{(II)}B^{(II)}} \end{pmatrix} \begin{pmatrix} \delta p_c \\ \delta p_f^{(II)} \end{pmatrix} \tag{3.21}$$

Now, consider a mixture of these two rock materials to obtain a dual porosity rock as presented in Figure 3.3.

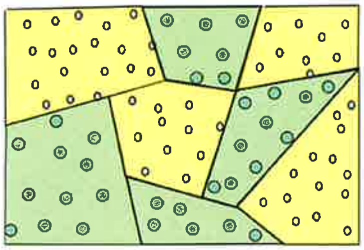

Figure 3.3. Conceptual model for a dual porosity rock in a general sense. Rock with embedded fracture can be treated as a specific case when the second medium can be well observed, thus can be well separated from the first medium in terms of strain measurement.

For a dual porosity medium in a three-dimensional space, each type of medium has its own domain completely connected, and the two types of media can also exchange pore fluids through their contact surfaces. In addition, their contact surfaces are "perfectly" bonded that deformation consistency is guaranteed. This will allow us to present the constitutive equations as follows (Lewallen and Wang, 1998):

$$\begin{pmatrix} \delta\varepsilon \\ \delta\zeta^{(I)} \\ \delta\zeta^{(II)} \end{pmatrix} = \begin{pmatrix} a_{11} & a_{12} & a_{13} \\ a_{21} & a_{22} & a_{23} \\ a_{31} & a_{32} & a_{33} \end{pmatrix} \begin{pmatrix} \delta p_c \\ \delta p_f^{(I)} \\ \delta p_f^{(II)} \end{pmatrix} \qquad (3.22)$$

Since this matrix is completely symmetric (Berryman and Wang, 1995), it can be simplified as:

$$\begin{pmatrix} \delta\varepsilon \\ \delta\zeta^{(1)} \\ \delta\zeta^{(II)} \end{pmatrix} = \begin{pmatrix} a_{11} & a_{12} & a_{13} \\ a_{12} & a_{22} & a_{23} \\ a_{13} & a_{23} & a_{33} \end{pmatrix} \begin{pmatrix} \delta p_c \\ \delta p_f^{(I)} \\ \delta p_f^{(II)} \end{pmatrix} \qquad (3.23)$$

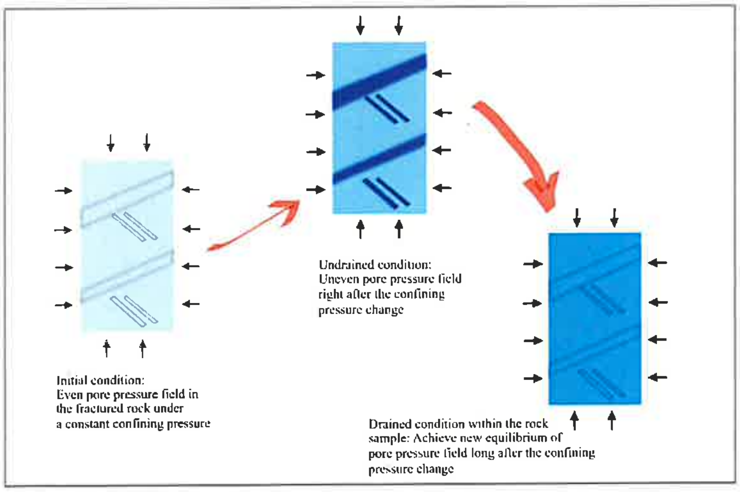

Figure 3.4. Pore pressure behavior for a dual-porosity rock (for example, a fractured rock sample) during the measurement of Skempton's B (right after the change of the confining pressure, the pore pressure field is uneven with different pressures in different domains because of the different pore stiffness for different domains. Overtime, the pore pressure will reach an even condition after a drained condition within the rock sample is established). This phenomenon has been observed during Skempton's B measurement in the laboratory test and can also be visualized from a numerical modeling approach.

There are altogether six parameters in Equation 3.23 for fully understanding a dual-porosity medium, which are $a_{11}, a_{12}, a_{13}, a_{22}, a_{23}, a_{33}$. The main difference between the single-porosity and dual-porosity formulation is that the pore pressure $p_f^{(I)}$ in the first type of porosity can be different from that of pore pressure $p_f^{(II)}$ in the second type of porosity over a relatively long-time scale. This phenomenon has been observed during Skempton's B measurement and can be described in Figure 3.4. By conducting a few laboratory tests, the correlation of the measurable quantities and the coefficients can be established, thus the matrix of Equation 3.23 can be resolved.

A very simplified case of a dual-porosity medium is a low permeability rock with a fracture (or a fractured zone), especially when this fracture is in a horizontal direction to allow an easy measurement on the strain for the two different domains (i.e., the rock matrix and the fracture zone). Figure 3.5 shows the sample configuration. For such a sample, the two domains (the rock matrix and the fracture zone) can be clearly identified and separated. Two biaxial strain gauges are attached on the rock matrix (one on the upper part above the fracture, and another on the bottom part , and a pair of axial LVDT is installed on the sample to cover the fracture zone, thus the axial strain in the fracture zone can be estimated as the difference between the axial strain measured by LVDT (for the whole rock sample) and the axial strain measured by the strain gauge (for the rock matrix only). Two pressure transducers are attached to the sample, with one to monitor the pore pressure inside the fracture and another to monitor the pore pressure inside the rock matrix.

According to Equation 3.23, altogether there are six parameters that need to be resolved ($a_{11}, a_{12}, a_{13}, a_{22}, a_{23}, a_{33}$) in order to be able to fully reveal a dual-porosity medium. Therefore, at least six independent tests are needed.

Test 1 a_{11}: This test can be conducted on the whole rock sample.

This is a drained hydrostatic compression test (long time, maintain constant pore pressure, change (usually increase) the confining pressure). Based on the equation $\delta\varepsilon = a_{11}\delta p_c + a_{12}\delta p_f^{(I)} + a_{13}\delta p_f^{(II)}$, under a fully drained condition that ensures pore pressure equilibrium at a reference status (such as to open the pore connection to the atmosphere) over a long time, $\delta p_f^{(I)} = \delta p_f^{(II)} = 0$. Assuming the superscript $^{(I)}$ refers to the rock matrix and $^{(II)}$ refers to the fracture zone. Such that:

$$\delta\varepsilon = a_{11}\delta p_c + a_{12}\delta p_f^{(I)}(=0) + a_{13}\delta p_f^{(II)}(=0) \quad \to \quad a_{11} = \frac{\delta\varepsilon_v}{\delta p_c} = \frac{1}{K} \qquad (3.24)$$

where K is the drained bulk modulus of the whole rock. The volumetric strain can be taken as the summation of the average axial strain measured by the two axial LVDTs and the two radial strains by the two radial strain gauges, .i.e., $\delta\varepsilon_v = \delta\varepsilon_{axial(by-axial-LVDT)} + \delta\varepsilon_{radial(by-radial-gauge-1)} + \delta\varepsilon_{radial(by-radial-gauge-2)}$.

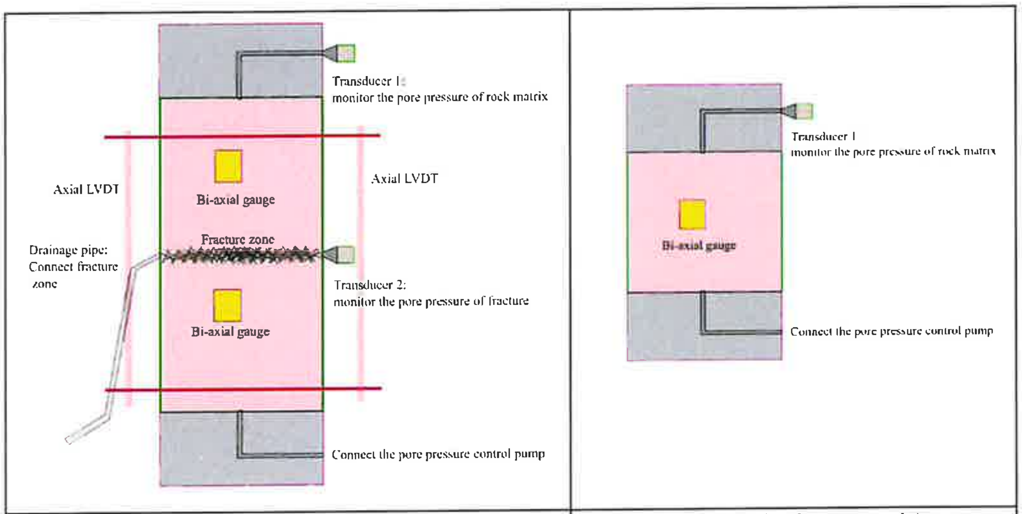

Whole rock sample (rock matrix + fracture) | *Intact rock sample (rock matrix only)*

Figure 3.5. Sample configuration (A very simple case of dual porosity rock is a sample with a horizontal fracture). **Left:** whole sample setup: Two pressure transducers are attached on the sample with one to monitor the pore pressure in the fracture, and another one to monitor the pore pressure in the rock matrix. A drainage pipe is connected to the fracture zone from the syringe pump; this pipe can be removed for some tests if an undrained condition is needed. Two sets of biaxial strain gauges are attached on the sample's surface, with two axial LVDTs installed on the sample across the fracture. Two sets of bi-axial gauges, which can give four strain measurements by gauge (axial strain by axial gauge 1 and 2; radial strain by radial gauge 1 and 2). Two axial LVDTs yield the whole sample axial strain by averaging these two LVDTs' readings. **Right:** intact part of the sample setup: after the tests on the whole sample, half of the sample can be further processed for a better measurement on the rock matrix. In case there are some other intact sample with similar rock matrix properties, it might also be feasible to use that sample for the intact rock matrix measurement.

Test 2 $a_{12}+a_{13}$: This test can be conducted on the whole rock sample.

This test is to measure the grain bulk modulus of the rock, which is an unjacketed drained hydrostatic compression test (long time, the pore pressure and the confining pressure are the same during the test; or practically, keep the pore pressure lower than the confining pressure at a constant difference). Since the pore pressures in both domains are in the equilibrium with the confining pressure, there is $\delta p_f^{(I)} = \delta p_f^{(II)} = \delta p_c$, then:

$$a_{11}+a_{12}+a_{13}=\frac{\delta\varepsilon_v}{\delta p_c}=\frac{1}{K_s} \quad \to \quad a_{12}+a_{13}=\frac{1}{K_s}-a_{11}=\frac{1}{K_s}-\frac{1}{K} \tag{3.25}$$

where K_s is the grain bulk modulus of the whole rock. The volumetric strain should be totally based on the strain gauge measurements, excluding the LVDT measurement, i.e., $\delta\varepsilon_v = \delta\varepsilon_{axial(average-axial-gauge-1/2)} + \delta\varepsilon_{radial(by-radial-gauge-1)} + \delta\varepsilon_{radial(by-radial-gauge-2)}$. The next step is to resolve either a_{12} or a_{13}.Since their summation is known from this step, once one quantity is solved, another one can be determined.

Test 3a a_{13} : This test can be conducted on the whole rock sample.

This test is to measure the poroelastic expansion coefficient of the fracture that is embedded in the whole rock sample. Consider this equation $\delta\varepsilon = a_{11}\delta p_c + a_{12}\delta p_f^{(I)} + a_{13}\delta p_f^{(II)}$. If the confining pressure p_c and the pore pressure inside the rock matrix $p_f^{(I)}$ can be kept constant, then a_{13} can be resolved by changing the fluid pressure inside the fracture. In this case, we perform a test to measure $H^{(II)}$ on the fracture by using the whole rock sample. In this test, maintain a constant confining pressure and pore pressure in the rock matrix, but quickly change (usually decrease) the pore pressure inside the fracture. Then there is

$$\delta p_c = \delta p_f^{(I)} = 0 \text{, and } \delta\varepsilon = a_{13}\delta p_f^{(II)} \quad \rightarrow \quad a_{13} = \frac{\delta\varepsilon_v}{\delta p_f^{(II)}} = \frac{1}{H^{(II)}}. \tag{3.26}$$

The volumetric strain is the summation of the difference axial strain between axial LVDT and axial strain gauge measurements and the two radial strains by the two radial strain gauges, i.e., $\delta\varepsilon_v = (\delta\varepsilon_{axial(by-LVDT)} - \delta\varepsilon_{axial(average-axial-gauge-1/2)}) + \delta\varepsilon_{radial(by-radial-gauge-1)} + \delta\varepsilon_{radial(by-radial-gauge-2)}$. Once a_{13} is known, a_{12} can be resolved by using Equation 3.25 , $a_{12} = \frac{1}{K_s} - a_{11} - a_{13} = \frac{1}{K_s} - \frac{1}{K} - \frac{1}{H^{(II)}}$. However, compared with Test 1 and 2, this test (Test 3)'s accuracy might be lower because the boundary condition $\delta p_f^{(I)} = 0$ may not be strictly preserved due to the fluid exchange between fracture and rock matrix. Therefore, another test to directly measure a_{12} is suggested as follows.

Test 3b a_{12} : This test can be conducted on an intact rock sample.

This test is to measure the poroelastic expansion coefficient of the rock matrix (intact rock plug). Again, revisit the equation $\delta\varepsilon = a_{11}\delta p_c + a_{12}\delta p_f^{(I)} + a_{13}\delta p_f^{(II)}$. If the confining pressure p_c and the pore pressure inside the fracture $p_f^{(II)}$ can be kept constant, then a_{12} can be resolved by changing the pore pressure inside the rock matrix. In this case, we perform a test to measure $H^{(I)}$ on the rock matrix by using the solid rock plug. In this test, maintain a constant confining pressure, but change the pore pressure inside the rock matrix. Then there is

$$\delta p_c (= \delta p_f^{(II)}) = 0 \text{, and } \delta\varepsilon = a_{12}\delta p_f^{(I)} \quad \rightarrow \quad a_{12} = \frac{\delta\varepsilon_v}{\delta p_f^{(I)}} = \frac{1}{H^{(I)}}. \tag{3.27}$$

In which $\delta\varepsilon_v = \delta\varepsilon_{axial(by-axial-gauge-1)} + 2\cdot\delta\varepsilon_{radial(by-radial-gauge-1)}$. So a_{12} is the inverse of poroelastic expansion coefficient (as in the single porosity case) which describes the volumetric strain change due to pore pressure change in one domain (i.e., the rock matrix). Since $a_{12} + a_{13}$ is known in the Test 2, a_{13} can be resolved by $a_{13} = \frac{1}{K_s} - a_{11} - a_{12} = \frac{1}{K_s} - \frac{1}{K} - \frac{1}{H^{(I)}}$.

Note that Test 3a and 3b are parallel, and only one test is needed to resolve the problem. However, with one more test, one can take advantage of further verification on the test results. The next step is to resolve a_{22} , and there are two different approaches, one is on the whole rock sample and another one is on the intact rock sample.

Test 4a a_{22} : This test can be conducted on the whole rock sample.

This test is to measure Skempton's B on the rock matrix. Now check the equation $\delta\zeta^{(1)} = a_{12}\delta p_c + a_{22}\delta p_f^{(I)} + a_{23}\delta p_f^{(II)}$. $\zeta^{(1)}$ refers to the fluid content, which is difficult to measure but relatively easy to handle if setting a boundary of undrained condition ($\zeta^{(1)} = 0$). In this test, the fluid pressure inside the fracture is maintained constantly to ensure $\delta p_f^{(II)} = 0$, and the rock matrix part is kept in an undrained condition ($\zeta^{(1)} = 0$) by closing the valve between the pore pressure control pump and the rock sample. Then, there is

$$0 = \delta\zeta^{(1)} = a_{12}\delta p_c + a_{22}\delta p_f^{(I)} + a_{23}\delta p_f^{(II)}(=0)$$

$$\rightarrow \quad a_{12}\delta p_c + a_{22}\delta p_f^{(I)} = 0 \quad \rightarrow \quad a_{22} = -a_{12}\frac{\delta p_c}{\delta p_f^{(I)}} = \frac{-1}{H^{(I)}B^{(I)}} \qquad (3.28)$$

Again, this test (Test 4a)'s accuracy might also be low because the boundary condition $\delta p_f^{(II)} = 0$ may not be strictly preserved due to the fluid exchange between fracture and rock matrix. Therefore, another test to directly measure a_{22} is suggested as follows.

Test 4b a_{22} : This test can be conducted on the intact rock sample.

This test is to measure Skempton's B on the rock matrix by using the intact rock sample instead of the whole rock sample with the embedded fracture. In this case, the equation $\delta\zeta^{(1)} = a_{12}\delta p_c + a_{22}\delta p_f^{(I)} + a_{23}\delta p_f^{(II)}$ is reduced to $\delta\zeta^{(1)} = a_{12}\delta p_c + a_{22}\delta p_f^{(I)}$ because there is no fracture (the second domain) in this case. And by isolating the sample from the pore pressure control pump to ensure $\zeta^{(1)} = 0$, then there is $0 = a_{12}\delta p_c + a_{22}\delta p_f^{(I)} \rightarrow a_{22} = -a_{12}\dfrac{\delta p_c}{\delta p_f^{(I)}} = -a_{12}\dfrac{1}{B^{(I)}} = -\dfrac{1}{H^{(I)}B^{(I)}}$. Thus a_{22} can also be resolved at this step.

Similarly, as that of Test 3a and 3b, Test 4a and 4b are in parallel, and only one test is needed to resolve a_{22}. However, with one more test, one can take advantage for further verification on the test results.

Test 5 and 6. a_{23}, a_{33} : These two tests can be conducted on the whole rock sample. The pipe that connects to the fluid pressure control pump with fracture zone needs to be removed to ensure an undrained condition. These two tests involve Skempton's B measurements for the whole rock sample (short time frame (Test 5) versus long time frame (Test 6)).

For an undrained test to measure the Skempton's B, the total fluid mass is conserved, thus the boundary conditions are $\delta\zeta^{(I)} + \delta\zeta^{(II)} = \delta\Sigma\zeta = 0$. Then making a summation of the last two equations in the matrix of the Equation 3.23, we can get the following equation:

$$0 = \delta\zeta^{(I)} + \delta\zeta^{(II)} = (a_{12} + a_{13})\delta p_c + (a_{22} + a_{23})\delta p_f^{(I)} + (a_{23} + a_{33})\delta p_f^{(II)} \qquad (3.29)$$

In this test, right after the confining pressure Pc increases, the pore pressure inside the rock matrix and the fracture zone can be recorded, and they are supposed to be not similar. Note in this equation, there are only two unknowns, a_{23}, a_{33}. Other quantities, a_{12}, a_{13}, a_{22}, have all been acquired from the previous tests, while the confining pressure and pore pressure in the rock matrix and fracture are also known values as they are all recorded during the test.

Overtime, the pore pressure in the two domains will eventually reach equilibrium, which will give $\delta p_f^{(I)} = \delta p_f^{(II)} = \delta p_f$. Then the above Equation 3.29 can be written as

$$0 = (a_{12} + a_{13})\delta p_c + (a_{22} + a_{23})\delta p_f + (a_{23} + a_{33})\delta p_f \tag{3.30}$$

Since Equations 3.29 and 3.30 are two different equations, thus the two unknowns, a_{23}, a_{33}, can be resolved. This finishes all the tests. The following Table 3.2 presents a summary of the testing methodology.

Table 3.2. Laboratory testing methodology summary.

Test ID		Parameter	Sample type	Theoretical background
1		a_{11}	whole rock sample	$a_{11} = \frac{\delta \varepsilon_{v(whole-domain)}}{\delta p_c} = \frac{1}{K}$
2		$a_{12} + a_{13}$	whole rock sample	$a_{12} + a_{13} = \frac{1}{K_s} - a_{11} = \frac{1}{K_s} - \frac{1}{K}$
3	3a	a_{13}	whole rock sample	$a_{13} = \frac{\delta \varepsilon_{v(fracture-zone-domain)}}{\delta p_f^{(II)}} = \frac{1}{H^{(II)}}$
	3b	a_{12}	intact rock sample	$a_{12} = \frac{\delta \varepsilon_{v(rock-matrix-domain)}}{\delta p_f^{(I)}} = \frac{1}{H^{(I)}}$
4	4a	a_{22}	whole rock sample	$a_{22} = -a_{12}\frac{\delta p_c}{\delta p_f^{(I)}} = \frac{-1}{H^{(I)}B^{(I)}}$
	4b	a_{22}	intact rock sample	
5		a_{23}, a_{33}	whole rock sample	$0 = (a_{12} + a_{13})\delta p_c + (a_{22} + a_{23})\delta p_f^{(I)} + (a_{23} + a_{33})\delta p_f^{(II)}$
6				$0 = (a_{12} + a_{13})\delta p_c + (a_{22} + a_{23})\delta p_f + (a_{23} + a_{33})\delta p_f$

In this research, the most complicated parameter is a_{23}, as it characterizes the correlation between the two domains of intact rock and the fracture zone.

3.2 Experimental Methodology

This section outlines the experimental approach for characterizing the thermo-poromechanical (TPM) properties of Utah FORGE core samples, building on established methods from prior work (Zhou & Ghassemi, 2015–2024). The methodology integrates sample preparation, testing setup, and procedures tailored to granite under reservoir-relevant conditions.

3.2.1 Overview of Testing Setup and Procedures

The experiments were conducted using a triaxial loading system (Figure 3.6) equipped with pore pressure and temperature control, following protocols refined in Zhou et al. (2015, 2022, 2024). Key components include:

MTS 810/816 Triaxial Cell with the confining pressure that can be held up to 70 MPa by using hydraulic oil medium; the axial load is applied by the servo-controlled actuator, up to 15KN to 100KN. The pore pressure system is configured based on the ISCO syringe pumps (±0.01 MPa accuracy). The thermal control system comprises resistive heating jackets rated for temperatures up to 200 °C (and up to 250 °C on a newly developed in-house pressure vessel). Temperature regulation is achieved via PID (Proportional-Integral-Derivative) controllers interfaced with thermocouples, enabling closed-loop feedback control for precise and stable thermal management throughout the experiment.

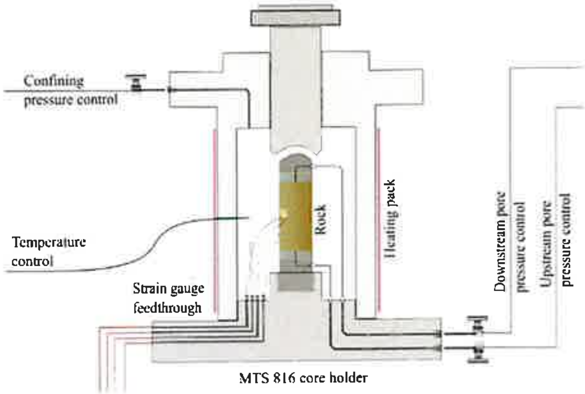

Figure 3.6. The schematic diagram of the testing system.

The laboratory setup consists of a high-pressure, high-temperature triaxial testing system integrated with pore-fluid control, temperature regulation, and acoustic emission monitoring. The experimental procedures include the following key steps:

1. **Initial Sample Characterization:** Density, porosity, mineralogical composition, and ultrasonic velocity measurements are conducted to establish baseline rock properties.
2. **Mechanical Testing:** Triaxial compression tests are performed to determine elastic moduli, UCS, and Mohr Coulomb failure envelope governing the Utah FORGE rocks.
3. **Poroelastic Testing:** Hydrostatic tests are performed to obtain stress-strain response under drained and undrained conditions to extract Biot's effective stress coefficients and Skempton's B, as outlined in Zhou et al. (2015, 2017, 2019).
4. **Thermal Testing:** Controlled heating experiments are conducted to evaluate thermal expansion, thermal pressurization, and permeability evolution with temperature. Also evaluate the Biot's coefficient and Skempton's B at different temperatures.
5. **Fluid Flow and Permeability Testing:** Permeability variations are assessed under different confining pressures and temperatures to understand fluid transport behavior in fractured and intact rock samples.

The integration of these tests provides a comprehensive assessment of the coupled thermo-poromechanical response of Utah FORGE core samples, facilitating a better understanding of stress evolution, thermal effects, and fluid transport in deep geothermal reservoirs.

3.2.2 Sample Preparation Techniques

Rock samples were prepared following standardized protocols to ensure reproducibility and consistency in experimental results. The preparation process included the following steps:

1. **Core Extraction and Cutting:** Cylindrical cores (typically 1.5-inch or 1-inch diameter) were extracted from Utah FORGE rock blocks using a diamond-core drilling system. The core orientation was preserved to maintain in-situ stress references.
2. **Surface Grinding and Polishing:** The ends of each sample were precision-ground to achieve parallel surfaces within ±0.01 mm (per ASTM D4543), reducing end effects during hydrostatic compression and/or triaxial testing.
3. **Drying and Saturation Protocols:** Samples were oven-dried at 40~60°C for 48 hours before saturation with deionized water or formation brine to replicate reservoir fluid conditions.
4. **Strain Gauge and Acoustic Sensor Installation:** Strain gages were attached for localized deformation measurements, and acoustic sensors were mounted for micro-seismic event detection during loading. An ultra-thin copper jacket (0.076 mm thickness) was employed to isolate the pore fluid from the confining fluid. A confining pressure of 500 psi was applied to ensure a tight fit of the jacket around the specimen prior to the installation of strain gauges and acoustic emission (AE) sensors.
5. **Thermal Conditioning:** For thermal testing, samples were preheated at controlled rates (usually slow enough) to prevent thermal shock and to allow for uniform temperature distribution before testing.

This rigorous sample preparation ensures the accuracy and reliability of mechanical, hydraulic, and thermal property measurements, aligning with established protocols from previous poroelastic studies (Zhou and Ghassemi, 2015, 2017, 2019, 2022, 2024). By integrating advanced experimental techniques with robust sample preparation, this study provides valuable insights into the thermo-poromechanical behavior of Utah FORGE rocks, aiding in the development of predictive models for enhanced geothermal systems (EGS).

4. Determination of Biot's Effective Stress Coefficient

4.1. Geological and Petrophysical Characteristics of Core Samples

The Utah FORGE reservoir is dominated by diorite, granodiorite, quartz monzonite, syenite, and granite ranging in age from 25.4 Ma to 8 Ma (Aleinikoff et al., 1987; Nielson et al., 1986; Coleman and Walker, 1992). Intergrown plagioclase, K-feldspar, and quartz are the major minerals within the granitoid (Jones et al., 2019). These minerals are accompanied by minor amounts of biotite, hornblende, clinopyroxene, apatite, titanite, zircon, and magnetite-ilmenite. Illite and chlorite are the dominant clay minerals. Other secondary minerals include carbonates, anhydrite, chlorite and epidote. During Phase 2, Well 58-32 was drilled to a total depth of 2290 m (7515 ft) GL. The well is located just west of the Mineral Mountains, northeast of Milford, Utah, to characterize the mechanical properties and stress framework of the rock and the fracture network (Handwerger and McLennan, 2019). Granite, quartz monzonite and monzonite are the dominant lithologies encountered in this well. Despite their mineralogic variations, the rocks are believed to have low permeabilities and similar mechanical properties. The matrix permeability within the reservoir rocks is low and fluid movement or storage are fracture-controlled. These samples were retrieved from different depths from Well 58-32 (Sample A~D) and Well 78-32 (Sample O). Some basic information is summarized in Table 4.1, and their images are shown in Figure 4.1. These samples show different textures. These samples can be classified into three groups based on their appearance: granodiorite (Sample A and D); granite (Sample B); diorite (Sample C and O) (Jones et al., 2019).

Table 4.1. Sample information

Sample ID		A	B	C	D	O
Depth	ft	6800.2	6807.1	7446.8	7449.7	8532.8
	m	2072.7	2074.8	2269.8	2270.6	2600.8
Length (mm)		88.08	85.63	79.81	74.71	85.33
Diameter (mm)		38.24	37.96	38.29	37.98	37.87
Weight (g)		265.86	253.60	258.38	222.97	270.98
Density (g/cm3)		2.63	2.62	2.81	2.63	2.82
Hardness		859	871	799	779	766
Std. Dev		11.08	21.9	49.84	63.45	47.15

Note: The hardness was tested by the Proceq Piccolo 2 Hardness Tester that yields the Leeb rebound hardness. There were ten tests on each sample with five on each end surface, thus the results are the average of these tests with a standard deviation.

Sample A | Sample B | Sample C | Sample D | Sample O

Figure 4.1. Sample image (these four samples appear to be three types of rock: granodiorite (Sample A and D), granite (Sample B) and diorite (Sample C and O) (Jones et al., 2019)).

It is very important to be able to accurately measure the strain of the sample during the test. We used four strain gauges on each sample with two axial strain gauges and two radial strain gauges. The volumetric strain is calculated by adding the averaged axial strain and the two radial strains (Figure 4.2).

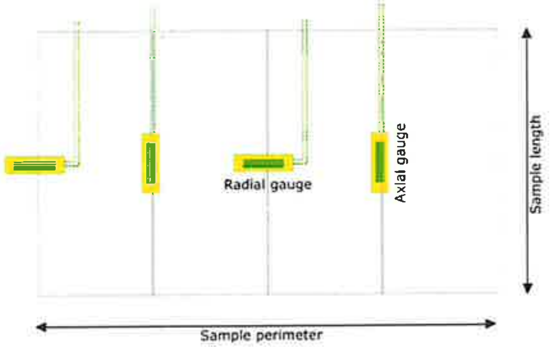

Figure 4.2. Layout of strain gauges on the sample surface.

Based on the pressure gradient of 1.13psi/ft (S_v), 0.74 psi/ft (S_{hmin}), 0.83~0.98psi/ft (S_{Hmax}) and 0.433 psi/ft (Pp) (Moore et al., 2020; Ye and Ghassemi, 2022; 2024), the in-situ effective stresses for these samples are in the range of 20 to 26 MPa. The in-situ temperatures of these samples are likely in a range of 140°C to 180°C (Di Drill, 2021).

4.2. Experimental Setup and Test Components

The tests were performed on MTS 810 for the Biot's coefficient. All these samples were tested following a similar test protocol. Distilled water was used as a pore fluid for all these measurements. The confining pressure and pore pressure were controlled by Teledyne ISO syringe pumps. Mineral oil was used for applying the confining pressure control. To achieve full saturation of the samples with water, a de-airing procedure was implemented after sample installation. This involved using a vacuum pump as the downstream pump to remove air from the pore system, while the upstream pump flooded the sample over an extended period of several days. For a more detailed description of the operational process, refer to Zhou and Ghassemi (2024). There are several methods to find the Biot's coefficient (Zhou and Ghassemi, 2015). Grain bulk modulus (*Ks*), drained bulk modulus (*K*), poroelastic expansion coefficient (*H*) are measured, and Biot's coefficient is obtained by the formula $\alpha=1-K/Ks$ and $\alpha=-K/H$. The rock sample is instrumented with strain measurement components for *Ks*, *K* and *H* measurements.

Grain bulk modulus, *Ks*, is the effective bulk modulus of the solid phase, which is free from the influence of the pore deformation (Cheng, 2016). In an unjacketed test (or a simulated unjacketed test with pore pressure (Pp) very close to the confining pressure (Pc) as in the case of this study), once the pore pressure inside the sample reaches equilibrium with the chamber pressure, every part of the solid surface, external or internal (surface of the interconnected pores), are subjected to the same uniform pressure. Thus, the time for the sample's pore pressure to reach equilibrium can be estimated from $t_c = L_c^2/c$ where c is the diffusivity coefficient that is directly proportional to the intrinsic permeability of the rock, and L_c is the largest distance that the pore pressure diffusion front needs to travel, which is the half length of the specimen in this work. For very porous rock such as Berea sandstone, the time to reach pore pressure equilibrium is in the order of seconds; but for low permeability rock (including granitoid), this is in many hours or longer. The test procedure is to increase both confining pressure and pore pressure concurrently and stepwise with pore pressure always lower (100 psi) than the confining pressure. A more detailed measuring method for the grain bulk modulus on low permeability rock can be found in Zhou and Ghassemi (2017; 2019). This stress path generally took a few days because of the low permeability of the samples. The waiting time for every increment must be long enough to allow pore pressure equilibrium in the sample. A way for detecting minimum waiting time is to observe the strain gauge readings, until these readings remain stable without any further change over the elapsed time. It was also noticed that different pore fluids or similar pore fluid at different temperatures (thus with different viscosities) could yield different grain bulk modulus.

Drained bulk modulus, *K*, is the ratio of confining pressure change over the volumetric strain under the boundary condition of constant pore pressure. When a sample is deformed, the reduction in its volume is contributed both by the compression of the solid phase and by the compaction of porous space due to the structural rearrangement of the rock skeleton. This relation satisfies the statement of the generalized Hooke's law between stress and strain. Since fluid is not participating in the mechanical response under drained condition, drained bulk modulus is a property of the solid phase only (Cheng, 2016). Drained bulk modulus is stress dependent, because during the hydrostatic compression test, the loading curve usually shows non-linear behavior for these rock samples. The non-linear macroscopic response of the porous medium is generally assumed to be related to the existence of a network of microcracks in the solid phase, and the progressive closure of cracks during loading is believed to control the material non-linearity.

Poroelastic expansion coefficient, *H*, is the ratio of pore pressure change and the volumetric strain under constant confining pressure (Wang, 2000). *H* is the counterpart of *K* and is less investigated in the past. *K* is measured under constant pore pressure by varying the confining pressure, while *H* is measured under constant confining pressure by varying the pore pressure. In fact, *H* has a similar unit as that of *K*, so it is another kind of modulus to evaluate the pore pressure effect on the rock deformation. *H* is a negative number because when the pore pressure is increased under constant confining pressure, the volumetric strain will decrease due to the decrease of effective stress by following the convention of rock mechanics with compression as positive. *H* is also stress dependent, similar to *K*. Hereafter *H* means $|H|$ for simplicity. The poroelastic expansion coefficient H can be evaluated along with the changing slope of the curve of the effective stress vs volumetric strain. Generally, these two types of curves share similar features, they exhibit an increasing slope as stress increases.

4.3. Experimental Results and Data Analysis

Sample A

The grain bulk modulus (K_s) tested with argon is consistently higher than that tested with water across all temperatures (Table 4.2). Below 100 °C, K_s measured with water tends to increase as temperature rises. This increase may be attributed to the reduced viscosity of water with temperature, allowing more fine pores to become accessible to the fluid. However, at 140 °C, K_s drops significantly, indicating that many pores may become isolated at this temperature. A likely explanation for this is the sealing of fractures, which restricts fluid access and affects the overall modulus.

Table 4.2. Grain bulk modulus of Sample A.

Pore fluid	Temperature (°C)	K_s (GPa)
Argon	22	99.46
water	140	33.66
water	90	68.95
water	50	63.66
water	22	59.87

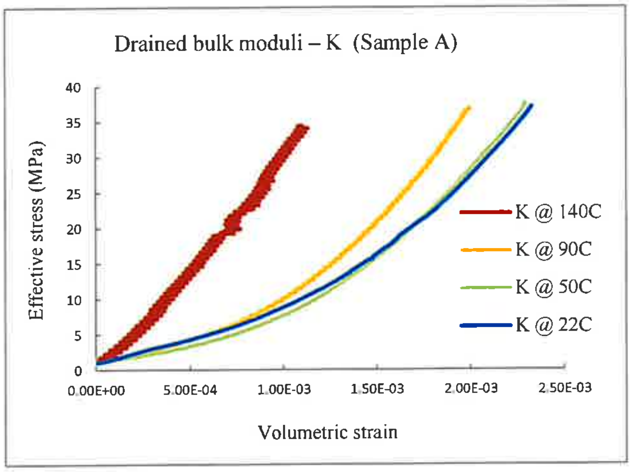

Figure 4.3. Bulk moduli (Sample A).

At room temperature (22°C) and 50°C, the curves of *K* are very close (Figure 4.3). With the increase in the temperature, *K* also shows a trend of increase. At 140°C, the behavior of *K* shows a very different feature from the others. At 22°C, 50 °C, 90°C, *K* show concave curvatures, indicating the gradually closure of micro fissures with the increase of effective stress. At 140°C, *K* follows a straight line, and the slope are basically the same as the high-end slopes of those tested at lower temperatures, indicating the micro-cracks had already been closed even before applying compressive stress. The closure of these micro-cracks appears to be primarily driven by thermal effects at 140 °C, which may have played a key role in the observed response.

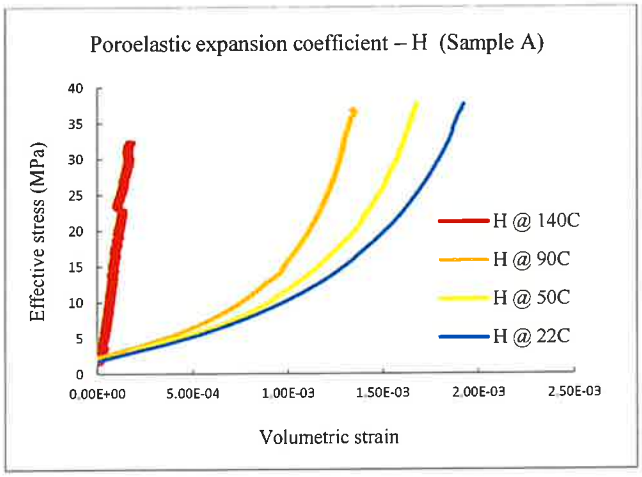

Figure 4.4. Poroelastic expansion coefficient (Sample A).

Similarly, *H* also shows a trend of increase with the increase of the temperature as that of *K* (Figure 4.4). At 140°C, the behavior of *H* shows a very different feature from the others, which has also been found in the measurement of *K*. At 22°C, 50 °C, 90°C, *H* show concave curvatures, indicating the gradually closure of micro fissures with the increase of effective stress. At 140°C, *H* follows a straight line, indicating the sample becomes very intact (due to the closure of micro-fissures) and much less permeable. *H* yields a very high slope as rock shape change (volumetric strain) becomes insensitive to the pore fluid's pressure change.

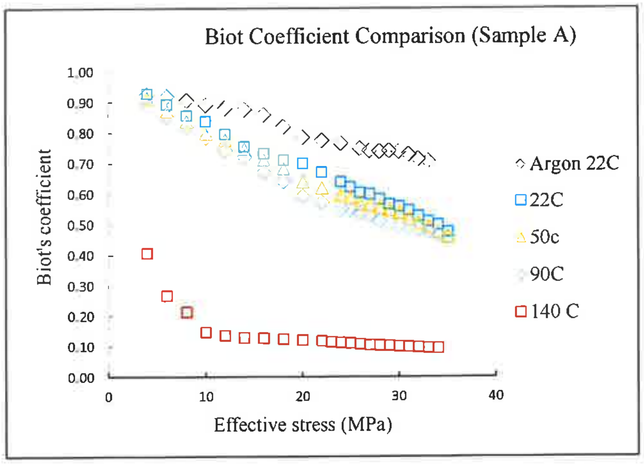

Figure 4.5. Biot's effective stress coefficient (Sample A).

All the tested results show a trend decreasing of Biot's coefficient with the increase of the effective stress (Figure 4.5). The Biot's coefficient as tested by argon is higher than that by water at any temperatures because the grain bulk modulus (*Ks*) as tested by argon is the highest. The results as tested by water at the temperatures of 22°C, 50°C and 90 °C are all very close and show an obviously stress-dependent feature. The result at 140°C is highly different from the other groups. The Biot's coefficient is much lower and much less stress dependent over a large effective stress range. At this temperature, a very low *Ks* indicates many pores are becoming isolated (thus these pores act as part of the solid phase rather than the pore fluid phase). Both approaches ($\alpha=1-K/Ks$; $\alpha=K/H$) well matches across various cases, and the results represent the average of both methods.

Sample B

This sample demonstrates a relatively consistent grain bulk modulus (*Ks*) across different pore fluid types (argon versus water) and various temperatures (Table 4.3).

Table 4.3. Grain bulk modulus of Sample B.

Pore fluid	Temperature (°C)	Ks (GPa)
Argon	22	67.89
water	140	66.87
water	80	68.95
water	22	66.03

The curves for 22°C and 80°C are quite close (Figure 4.6 and 4.7), exhibiting a trend of steeper slopes at the higher temperature. However, the curve for 140°C appears much linear, insensitive to the change of effective stress. At the higher effective stress range, both the K and H curves of 140°C display even lower slopes compared to their counterparts.

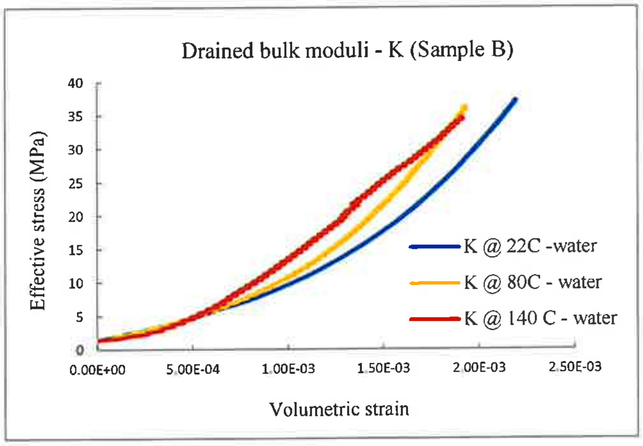

Figure 4.6. Bulk moduli (Sample B).

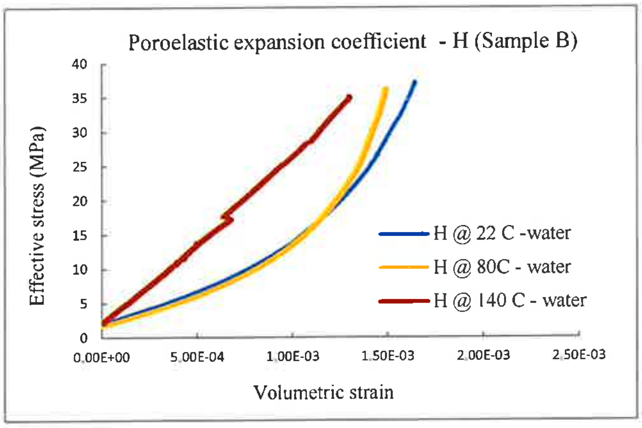

Figure 4.7. Poroelastic expansion coefficient (Sample B).

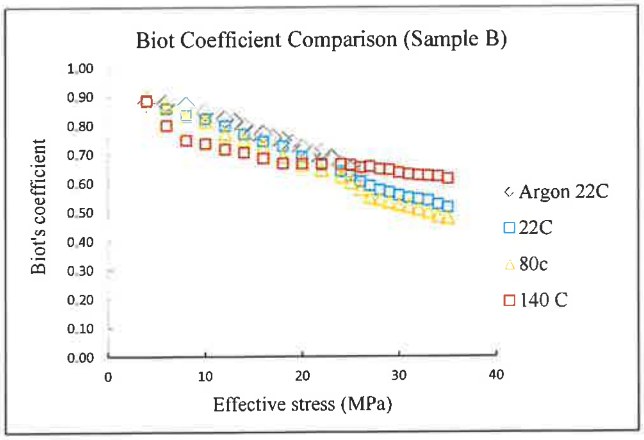

Figure 4.8. Biot's effective stress coefficient (Sample B).

All tested results indicate a decreasing trend of the Biot's coefficient with increasing effective stress (Figure 4.8). Unlike Sample A, Sample B does not demonstrate a stronger change of Biot's coefficient behavior at the higher temperature of 140 °C.

Sample C

This diorite sample shows that its grain bulk modulus (*Ks*) tested with argon is higher than that measured with water at all temperatures, which is consistent with the findings for Sample A (Table 4.4).

Table 4.4. Grain bulk modulus of Sample C.

Pore fluid	Temperature (°C)	Ks (GPa)
Argon	22	85.39
water	120	59.90
water	90	72.43
water	50	75.99
water	22	72.14

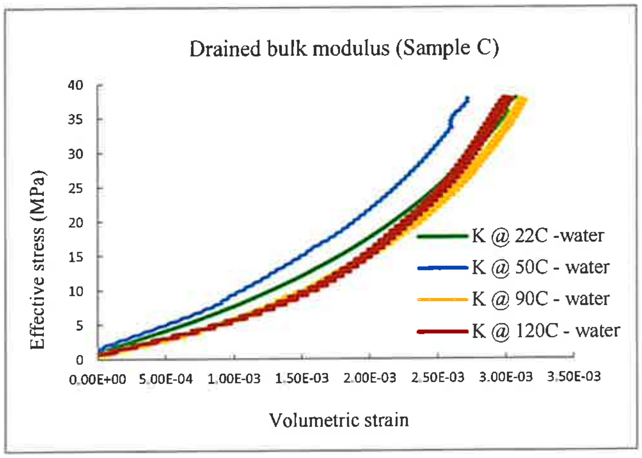

Figure 4.9. Bulk moduli (Sample C).

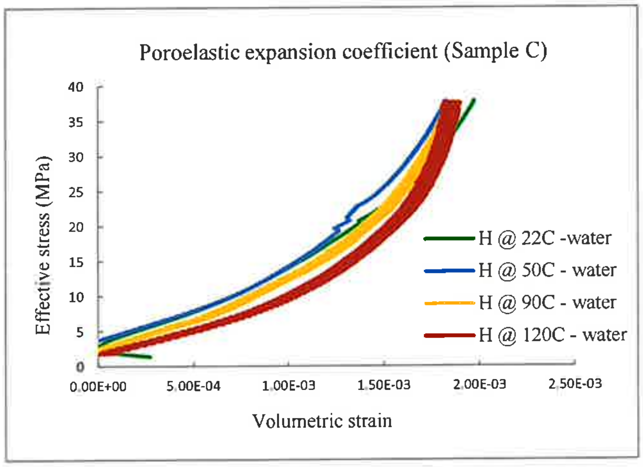

Figure 4.10. Poroelastic expansion coefficient (Sample C).

For this sample, all the *K* and *H* curves are relatively close, with the curves at higher temperatures showing slightly steeper slopes at elevated effective stress levels (Figure 4.9 and 4.10).

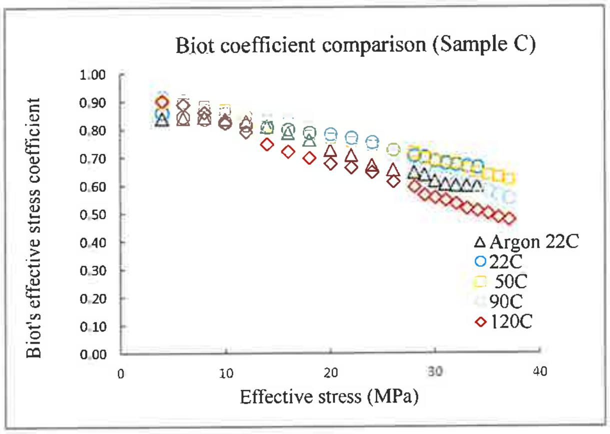

Figure 4.11. Biot's effective stress coefficient (Sample C).

All tested results indicate a decreasing trend with increasing effective stress (Figure 4.11). The Biot's coefficients at 120 °C are the lowest as observed. Overall, the thermal effect on this sample is less pronounced compared to other samples, such as Sample A and Sample D.

Sample D

This granodiorite sample exhibits a grain bulk modulus (*Ks*) tested with argon that is higher than when tested with water at all temperatures, similar to Sample A (Table 4.5). *Ks* shows an increasing trend with rising temperature, which may be attributed to the decrease in water viscosity with temperature, allowing more fine pores to become accessible to the thinner fluid.

Table 4.5. Grain bulk modulus of Sample D.

Pore fluid	Temperature (°C)	Ks (GPa)
Argon	22	104.49
water	22	69.51
water	80	72.20
water	140	72.83

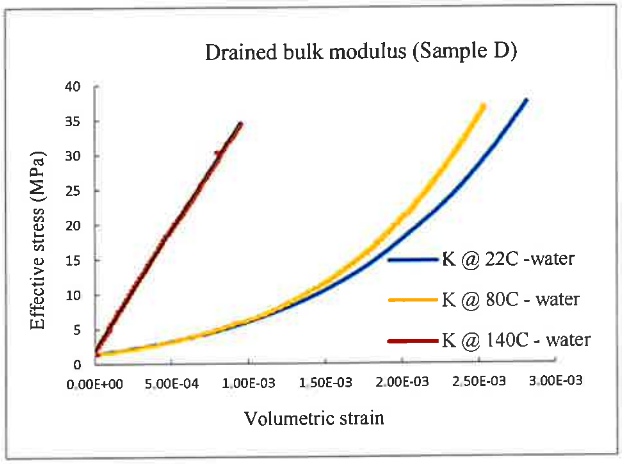

Figure 4.12. Bulk moduli (Sample D).

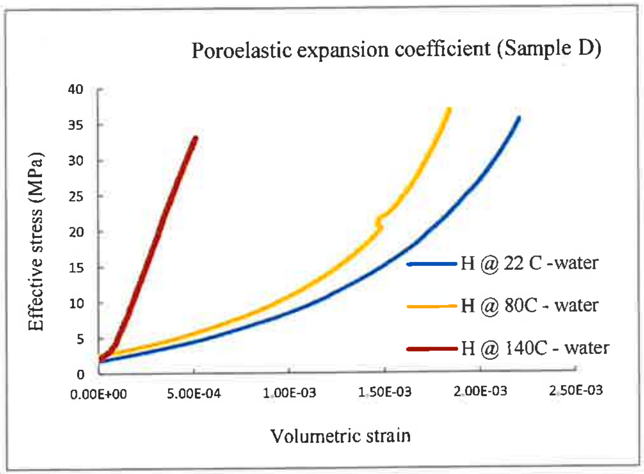

Figure 4.13. Poroelastic expansion coefficient (Sample D).

At room temperature (22°C) and 80°C, the curves of *K* are very similar (Figure 4.12). As temperature increases, the grain bulk modulus (*K*) shows a general upward trend. However, at 140°C, the behavior of *K* differs significantly from the others. At 22°C and 80°C, the *K* curves display concave curvatures, indicating the gradual closure of micro-fissures as effective stress increases. In contrast, at 140°C, the *K* curve follows a straight line, with a slope similar to the high-end slopes observed at lower temperatures. This suggests that the micro-fissures were already closed before the compression loading, likely due to the thermal effect at 140°C, which caused the fissures to have been sealed even before applying the hydrostatic compression.

Similar to *K*, *H* also shows an increasing trend with temperature (Figure 4.13). At 140°C, the behavior of *H* is notably different from the other temperatures, mirroring the pattern observed for *K*. At 22°C and 80°C, the *H* curves exhibit concave curvatures, indicating the gradual closure of micro-fissures as effective stress increases. However, at 140°C, the *H* curve follows a straight line, suggesting that the sample has become very intact—likely due to the closure of the micro-fissures—prior to any compression loading. This further supports the hypothesis that the thermal effect at 140°C has led to the sealing of micro-fissures in the sample.

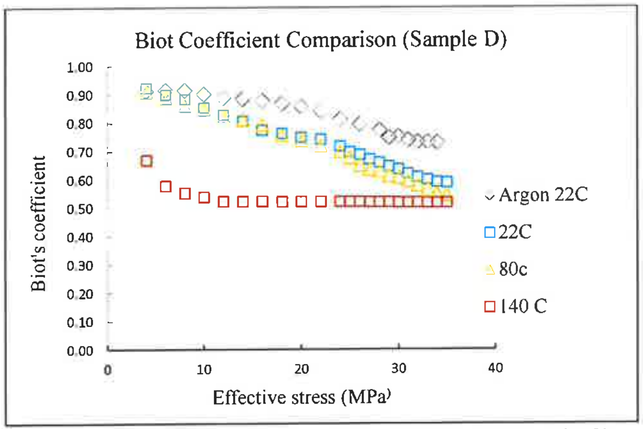

Figure 4.14. Biot's effective stress coefficient (Sample C).

All the tested results show a decreasing trend of the Biot's effective stress coefficients with increasing effective stress (Figure 4.14). The Biot's effective stress coefficient found using argon are higher than those from using water at any temperature, as the grain bulk modulus (*Ks*) measured with argon is the highest. At 22°C and 80°C, the results tested with water are very similar, showing a clear stress-dependent behavior. However, at 140°C, the results differ significantly. At this temperature, the Biot's coefficient is much lower and shows much less stress dependence across a wide range of effective stress, likely because *K* (and *H*) become less sensitive to changes in effective stress. Both approaches for calculating the Biot's coefficient ($\alpha = 1 - K/Ks$; $\alpha = K/H$) provide consistent values, confirming the reliability of the results. One may also note that Samples A and D exhibit very similar characteristics, given that they are the same type of rock.

4.4. Permeability Behavior Under Room and High Temperature Conditions

4.4.1. Permeability Under Room Temperature

In all the permeability tests at room temperature, the pore fluid is argon, and the pore pressure was always kept 1000 psi above argon's supercritical pressure (argon behaves more like a liquid above the critical point of 150K (-123 °C) and 4.863 MPa (705 psi)). The permeability was measured based on Darcy's law by the formula for the compressible fluid (Scheidegger, 1974):

$$k = \frac{q\mu L}{A\Delta P}\frac{P^{o}}{P^{m}} = \frac{4q\mu L}{\pi D^{2}\Delta P}\frac{P^{o}}{P^{m}} \qquad (4.1)$$

where k - permeability, A - cross sectional area, D-diameter of sample, μ – fluid viscosity, ΔP - pressure drop, L - sample length, *pm* - average of inlet and outlet pressures, *po* - outlet pressure, and q - flow rate at outlet pump (Note: *po* and q can also be replaced by the inlet pump data *pi* to yield the permeability based on the inlet pump). The lab measurement error is basically influenced by the pump accuracy and the caliper accuracy for the measurement of the sample's dimension. Note Brace et al. (1968) showed that permeability to water on Westerly granite was similar to that to argon gas at high pore pressure when the fluid is not in the gas status but in supercritical status.

In this work, the tests are conducted under conditions varying from low confining pressure (2MPa) to high confining pressure (around 30 MPa) covering the stress condition of interest (in-situ reservoir condition) by considering the samples depths (2070m ~ 2270 m). Using a stress gradient of 16.7~17.6 MPa/km for σ_{hmin}, 19MPa/km for σ_{hmax}, 25.6 MPa/km for σ_{v}, 9.8 MPa/km pore pressure (Pp), the effective mean stress of interests is in the range of 20 to 30 MPa. Note that the effective mean stress was determined by the formula: effective stress=confining pressure – pore pressure; in the case there is an axial differential stress, the effective mean stress= (1/3axial stress +2/3confining pressure) – (pore pressure).

Figure 4.15 shows the permeability behavior for these samples. Results show that all these samples' permeabilities are stress dependent and decrease with the increase of confining pressure. At high confining pressure, the permeabilities become less stress dependent when most of the fissures are closed. The pore structure appears to be very stiff as evidenced by its insensitivity to the high-level effective stresses. Overall, the permeabilities are in the range of 10 to 50 micro-Darcy for Sample A, C, D under the reservoir condition. Sample B shows a relatively lower permeability in the nano Darcy range. These tested results are generally consistent with the description of interval permeability by Moore, et al (2020). In addition, the permeability is also (highly) stress path/history dependent if compare the results during loading and unloading path (increase and decrease the confining pressure).

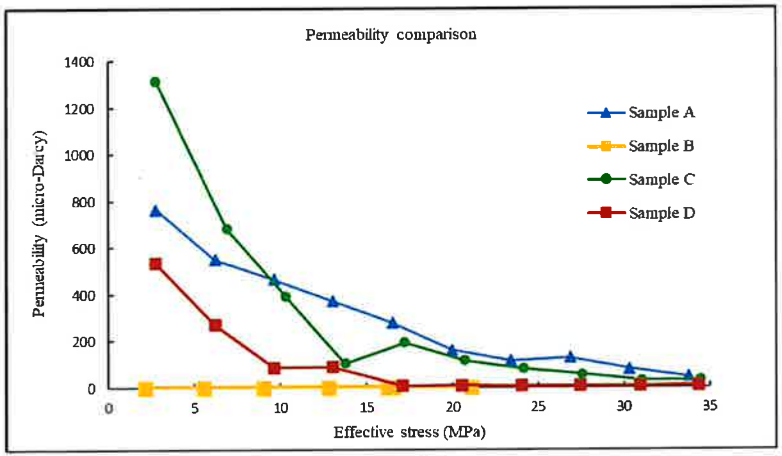

Figure 4.15. Permeability variation with confining pressure test at room temperature.

4.2. The impact of temperature on the permeability

Permeability is not only influenced by effective stress, but also by temperature. In the previous section, it was observed that generally, permeability decreases with an increase in effective stress. At high pressure, the permeabilities become less stress dependent when most of the fissures are closed (Zhou and Ghassemi, 2022). To examine the temperature effect on permeability without the influence of effective stress, the effective stress boundary condition was maintained constantly at a confining pressure of 1000 psi, with upstream and downstream pump pressures set at 500 psi and 490 psi, respectively. Note for these series of tests, distilled water was used as the pore fluid instead of argon. The temperature was the only variable adjusted. The permeability was estimated using Darcy's law. The temperature was increased in a stepwise manner at a slow rate of 3°C per hour, ensuring that the entire system remained in a quasi-stable condition. After reaching each new temperature level, the system was allowed to stabilize overnight. Measurements were taken only after the system reached thermal equilibrium, ensuring reliable data for establishing a correlation between permeability and temperature.

Both temperature and effective stress interact to influence the permeability of rocks, but their effects differ in complexity. The impact of effective stress is relatively straightforward with permeability generally decreasing exponentially with increasing effective stress, as effective stress increases, the rock's pore spaces compress, leading to a reduction in permeability. This occurs because higher effective stress can close pores or fractures, limiting the pathways available for fluid flow.

In contrast, the impact of temperature on permeability is more complex. As temperature rises, fluid viscosity generally decreases, which can enhance the fluid's ability to flow through the pore spaces. Additionally, heating or cooling can induce changes in the rock matrix due to thermal expansion or contraction, which may alter the pore structure and connectivity. In some cases, higher temperatures may lead to thermal cracking or the sealing of existing fractures, potentially increasing or decreasing permeability depending on the specific material and conditions.

Since both effective stress and temperature can influence permeability, it is ideal to isolate the effect of one factor by keeping the other constant. Otherwise, the combined impacts of these two factors may complicate the analysis, making it difficult to determine which factor is more dominant.

In this experimental procedure, effective stress is kept constant while investigating the impact of temperature on permeability. This approach ensures that any observed changes in permeability are attributed solely to temperature variations, as effective stress remains unchanged. The experimental setup includes a constant confining pressure (Pc) of 1000 psi, an upstream pore pressure of 500 psi, and a downstream pore pressure of 490 psi. The temperature starts at 22°C (room temperature) and is increased stepwise to 60°C, 90°C, 120°C, 150°C, and beyond, at a rate of 2°C per hour. The increment from one stage to the next level takes about 10~12 hours, and then the temperature is held constantly overnight for 12~14 hours. The flow rate of the last 3 hours at each temperature stage is taken for permeability measurement, using Darcy's law for the calculation.

By holding effective stress constant and gradually increasing the temperature, this method accurately isolates the impact of temperature on permeability. Using stable flow rates for permeability estimation and applying Darcy's law ensures precise and reliable results. The flow rate is extremely slow (ranging from 10^{-5} to 10^{-7} ml/sec), approximating a quasi-static condition. This allows sufficient time for the water in the pipes to heat up within the cell, ensuring it reaches the same temperature as the rock before interacting with the rock sample. All pressures, including confining pressure and upstream/downstream pump pressures, were kept constant throughout the experiment to maintain system stability and ensure a consistent effective stress boundary condition. The test results can be summarized in the following Figures 4.16-4.19.

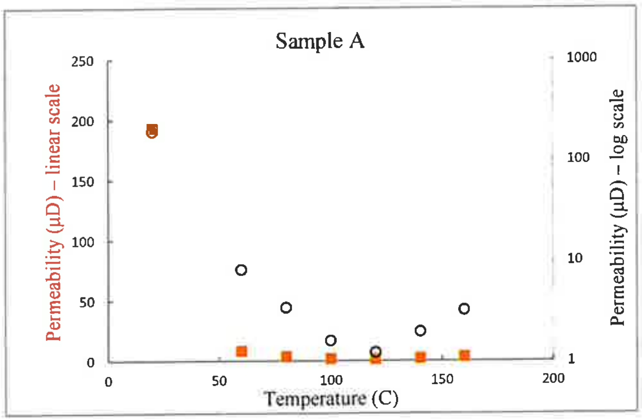

Figure 4.16. Permeability behavior of Sample A.

Upon heating, permeability decreases significantly and then stabilizes at a consistently low level. When viewed on a logarithmic scale, it is clearer to show that permeability continuously decreases as the temperature rises to 120°C, after which it begins to increase slightly (Figure 4.16).

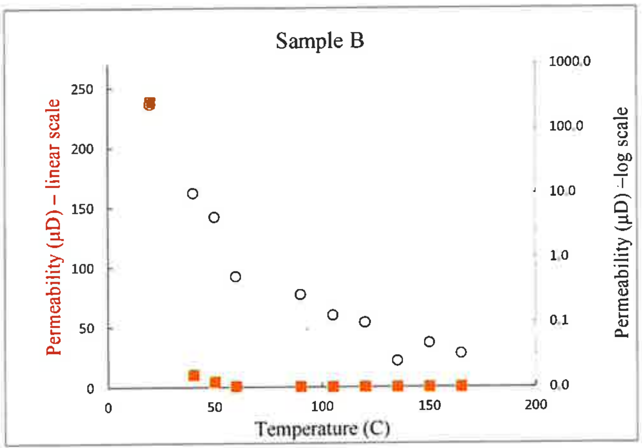

Figure 4.17. Permeability behavior of Sample B.

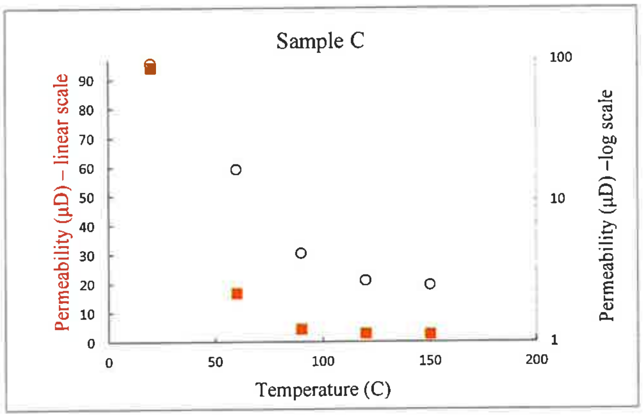

Figure 4.18. Permeability behavior of Sample C.

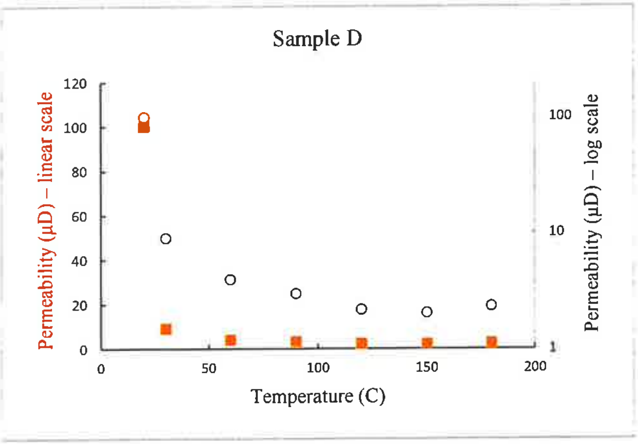

Figure 4.19. Permeability behavior of Sample D.

All samples exhibit a general trend of decreasing permeability with increasing temperature (Figures 4.17 and 4.18), though some show a slight rebound at higher temperatures (Figures 4.16 and 4.19).

5. Skempton's B Behavior Under Room and High Temperature Conditions

5.1. Skempton's B of Intact Rock Under Room and High Temperature conditions

Laboratory measurement of Skempton's *B* requires full saturation of the rock samples. Based on the conventional saturation method and some previous studies (ASTM 2004; Hart and Wang 1995; Mesri et al. 1976; Tarokh et al. 2018), as well as our own experiences, we developed a saturation method with a focus on to minimize the air concentration in the pore water by different approaches at different stages.

For a rock of low permeability, the test of Skempton's *B* is difficult and challenging. Unlike Biot's coefficient, which is a property of the solid rock only, Skempton's *B* is influenced by both rock matrix property and pore fluid property. Using different pore fluids (water, oil, or water with different gas/air concentration) will yield different *B* values. To make the results reliable and more meaningful with respect to the real-world applications, pure water saturation is desired, although this could be quite difficult for rock samples of low permeability and porosity. The workflow we used is described by the following flowchart (Figure 5.1).

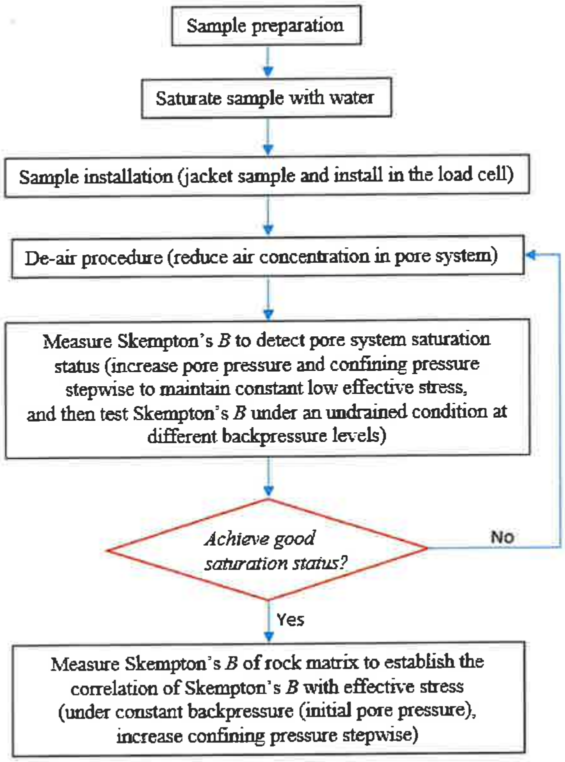

Figure 5.1. Laboratory test procedure flowchart (There are two sections of measuring Skempton's *B*: the first one (the box above the red diamond box of decision) on the impact of pore fluid compressibility to Skempton's *B*, and the second one (the box below the red diamond box) on the impact of rock structure to Skempton's *B*).

To study the dependency of Skempton's B on effective stress, a detailed test procedure was followed. This procedure involved saturating a granite specimen using back pressure and then incrementally increasing the confining pressure to create a range of effective stress conditions. The primary goal was to measure Skempton's B at different effective stresses and establish a correlation.

The saturation process is lengthy and requires patience. For full methodological details, one may refer to Zhou and Ghassemi (2024). In brief, the specimen is first saturated with back pressure for many days until fully saturated. Saturation is confirmed by conducting B-value checks at various pore pressure levels until consistently high values are obtained. The main parts for Skempton's B measurement include an MTS 810 core holder, a vacuum pump (PITTSBURGH, 3 CFM two stage vacuum pump), four Teledyne syringe pumps, a water container, an Agilent data acquisition system, a computer, and two pressure transducers (SMD P571 pressure sensor). They are connected and controlled with the use of pipes and valves (V1~V5 in Figure 5.2). All the pore fluid related parts (drainage lines, pressure transducers, platens, syringe pumps) must be flushed and filled with distilled/deaired water before sample installation in the MTS 810 core holder.

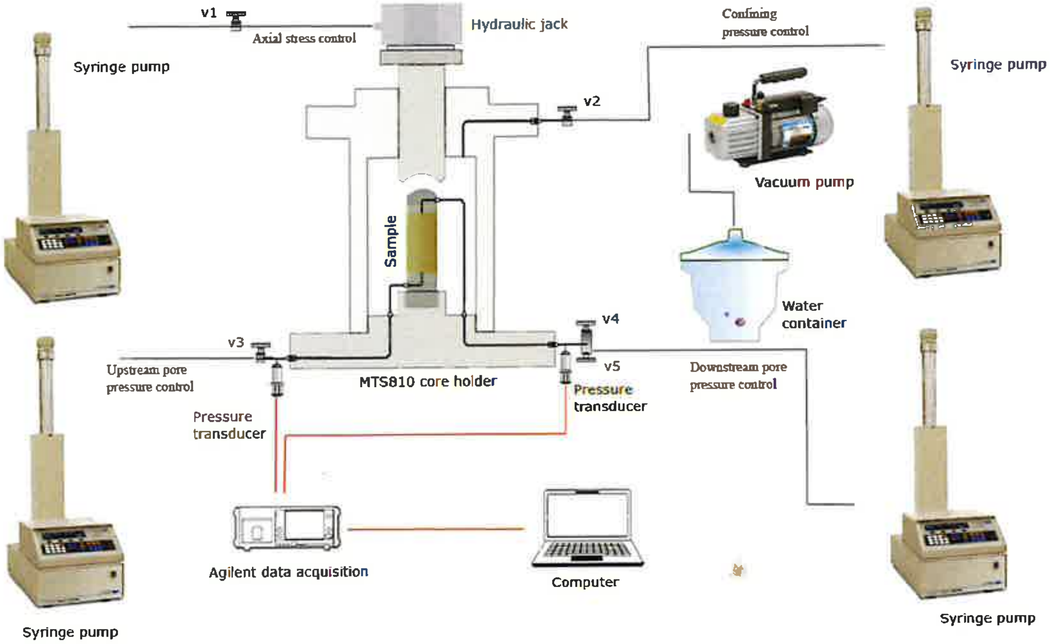

Figure 5.2. Schematic test configuration for Skempton's B measurement.

Once saturation is confirmed, the test procedure begins with setting an initial back pressure—typically 500 psi—and an equal initial confining pressure—typically 800 psi. The back pressure is then maintained constant throughout the entire test. Confining pressure is increased in fixed increments (e.g., 500 psi), and after each increment, the system is allowed to stabilize for at least 2.5 hours. During stabilization, pore pressure changes are recorded. Skempton's B is calculated for each step using the ratio $\Delta p/\Delta\sigma$, where Δp is the change in pore pressure and $\Delta\sigma$ is the change in confining pressure.

A typical loading path is illustrated in Figure 5.3. However, due to the rock's reduced permeability at higher effective stresses, the actual loading path deviates slightly. Waiting time between steps tends to increase progressively, ranging from 2.5 to 12 hours. Minimizing dead volume in the drainage system and allowing adequate stabilization time are critical for accuracy.

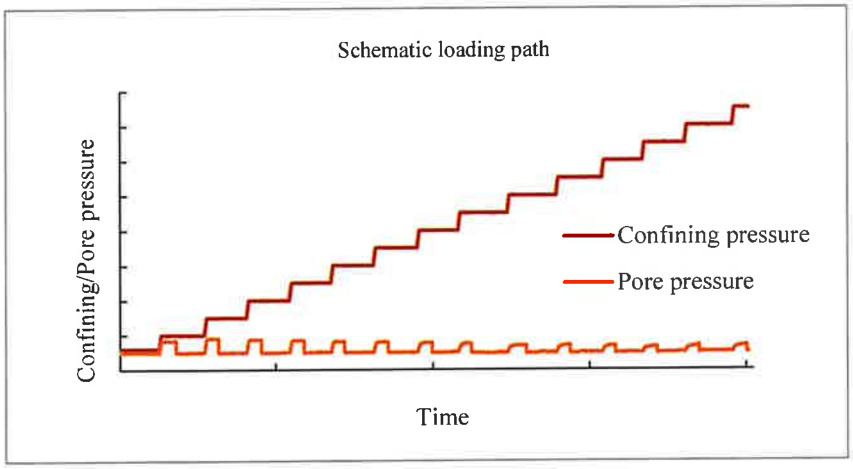

Figure 5.3. Typical loading path for Skempton's B measurement.

The initial pore pressure (set by both upstream and downstream pumps) is fixed prior to each run. This back pressure remains stable and high enough that changes in Skempton's B can be attributed solely to variations in effective stress—not to fluid compressibility, which remains consistent. According to Mesri et al. (1976), the threshold back pressure for a well-deaired sample is around 150–200 psi. In this work, a higher back pressure of 500 psi or more is typically used to eliminate free air in the pore fluid system.

To investigate the stress dependency of Skempton's B, tests can be run from different starting points, each with the same back pressure but varying confining pressures—thus different effective stresses. The average effective stress for each run is calculated as the difference between the confining pressure and pore pressure. Repeating this process across a range of conditions reveals how Skempton's B varies with effective stress.

The laboratory tests results can be summarized in the following Figures 5.4 -5.8.

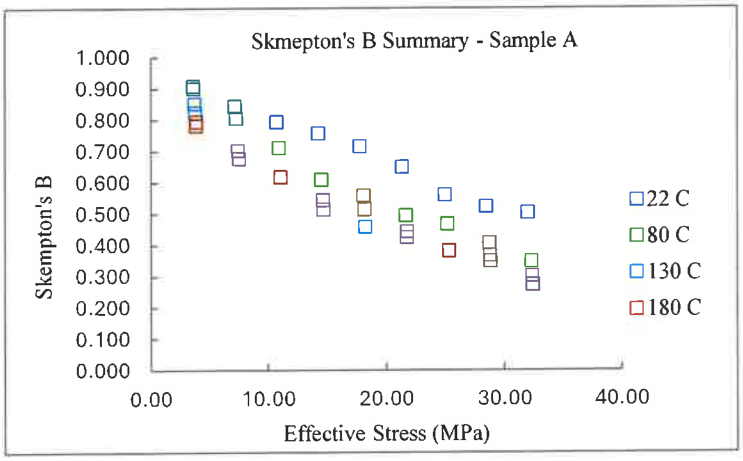

Figure 5.4. Skempton's B of Sample A.

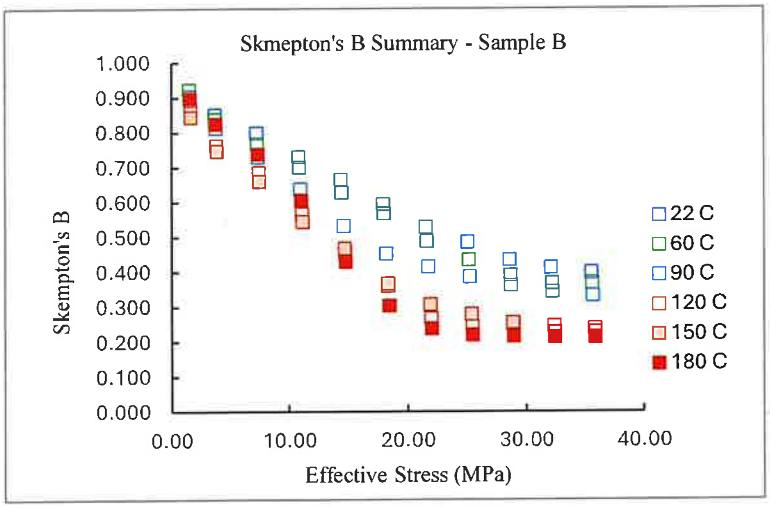

Figure 5.5. Skempton's B of Sample B.

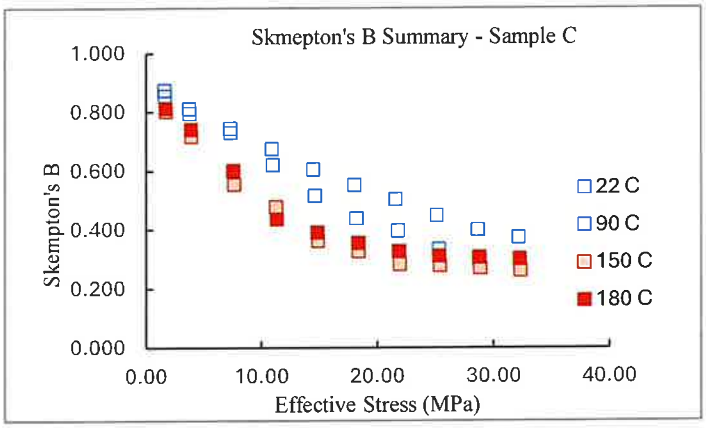

Figure 5.6. Skempton’s B of Sample C.

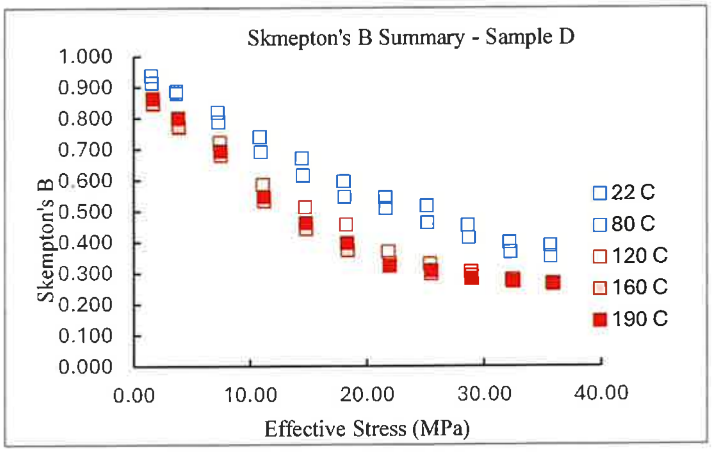

Figure 5.7. Skempton’s B of Sample D.

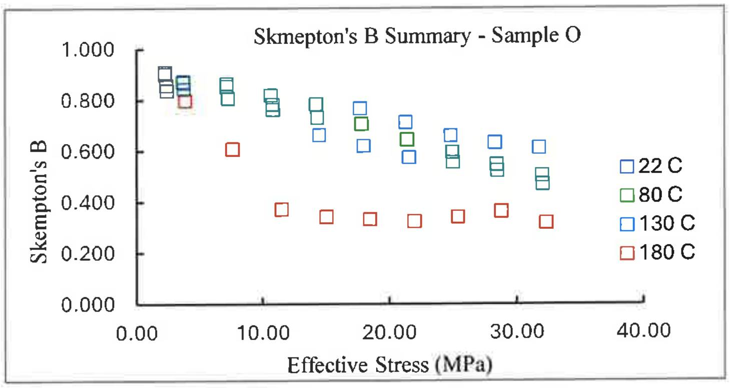

Figure 5.8. Skempton’s B of Sample O.

Note that Samples A through D were all tested after the alpha measurement, meaning they were subjected to the loading path associated with the alpha test prior to subsequent evaluation. In contrast, Sample O was tested before the alpha measurement, following a virgin loading path. As a result, Sample O may exhibit a more detailed or intrinsic representation of behavior B, as it reflects the material response prior to any influence from the alpha loading path. This distinction in loading history could account for differences in behavior observed between Sample O and Samples A–D. Note that in Sample O, the response at 180 °C is markedly different from those at lower temperatures and appears to mimic the alpha behavior seen in Samples A and D. This suggests that fissure closure initiates or becomes more pronounced at elevated temperatures, particularly around 180 °C.

5.2. Note on Viscoelastic Effects During Skempton's B Measurement:

It is important to recognize that either high effective stress or elevated temperature or both can introduce viscoelastic effects in the rock specimen during Skempton's B measurements. These effects manifest as time-dependent mechanical deformation (e.g., creep or stress relaxation) and delayed pore pressure equilibration, even after the initial pressure increment has been applied and an apparent stabilization has occurred. Due to this time-dependent behavior, pore pressure may continue to evolve for several hours following a confining pressure increase. This has a direct impact on how Skempton's B is calculated, as the Δp (change in pore pressure) used in Skempton's B formula can vary depending on when it is measured. For this reason, it is helpful to distinguish between two types of Skempton's B values:

- Elastic B: This is the B-value calculated immediately after the confining pressure increment, reflecting the rock's initial, undrained elastic response. It is most representative of the short-term, purely elastic behavior of the pore-fluid–rock system and assumes negligible fluid flow or viscoelastic deformation has occurred.

- Viscous-Affected B: This is the B-value calculated after a certain time period (e.g., from several minutes to hours), once viscoelastic deformation and any delayed pore pressure redistribution have occurred. This value reflects a more complete response of the system, including both elastic and time-dependent components, and may be lower or higher than the initial B depending on the material behavior.

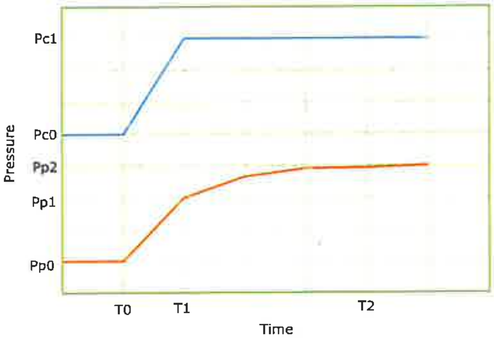

Figure 5.9. From time T_0 to T_1, as the confining pressure increases from Pc_0 to Pc_1, the pore pressure rises from Pp_0 to Pp_1. However, after T_1, the pore pressure may continue to evolve—often increasing—to Pp_2 at T_2, especially under high temperature and/or stress conditions. Therefore, Skempton's coefficient B can be separated into two components: Elastic B = $(Pp_1 - Pp_0) / (Pc_1 - Pc_0)$, and Viscous-affected B = $(Pp_2 - Pp_0) / (Pc_1 - Pc_0)$. Note that Elastic B is relatively unique and instantaneous, while Viscous-affected B is time-dependent and non-unique, reflecting ongoing pore pressure evolution.

Figure 5.9 shows Skempton's coefficient behavior for the explanation. The difference between these two values can be significant in low-permeability rocks or under test conditions involving high effective stresses or high temperatures or both, where viscoelastic and poroelastic coupling effects are more pronounced. As a result, careful documentation of the timing of each B-value measurement is essential, along with clear definitions in reporting whether the B-value represents the immediate (elastic) response or a time-averaged (viscous-influenced) behavior. To ensure reliable results, researchers are advised to:

- Allow sufficient time for stabilization, especially under high stress or temperature conditions.
- Record pore pressure over time following each confining pressure increment.
- Optionally report both elastic and viscous-affected B-values, depending on the test objectives.

This approach provides a more comprehensive understanding of stress-dependent and time-dependent pore pressure behavior and enhances the interpretation of Skempton's B in complex geomechanical environments. Figure 5.10 presents examples demonstrating that the actual Skempton's B-value exhibits more pronounced time-dependent behavior as stress levels, temperature, or both are increased, indicating a coupled thermo-mechanical influence on pore pressure response.

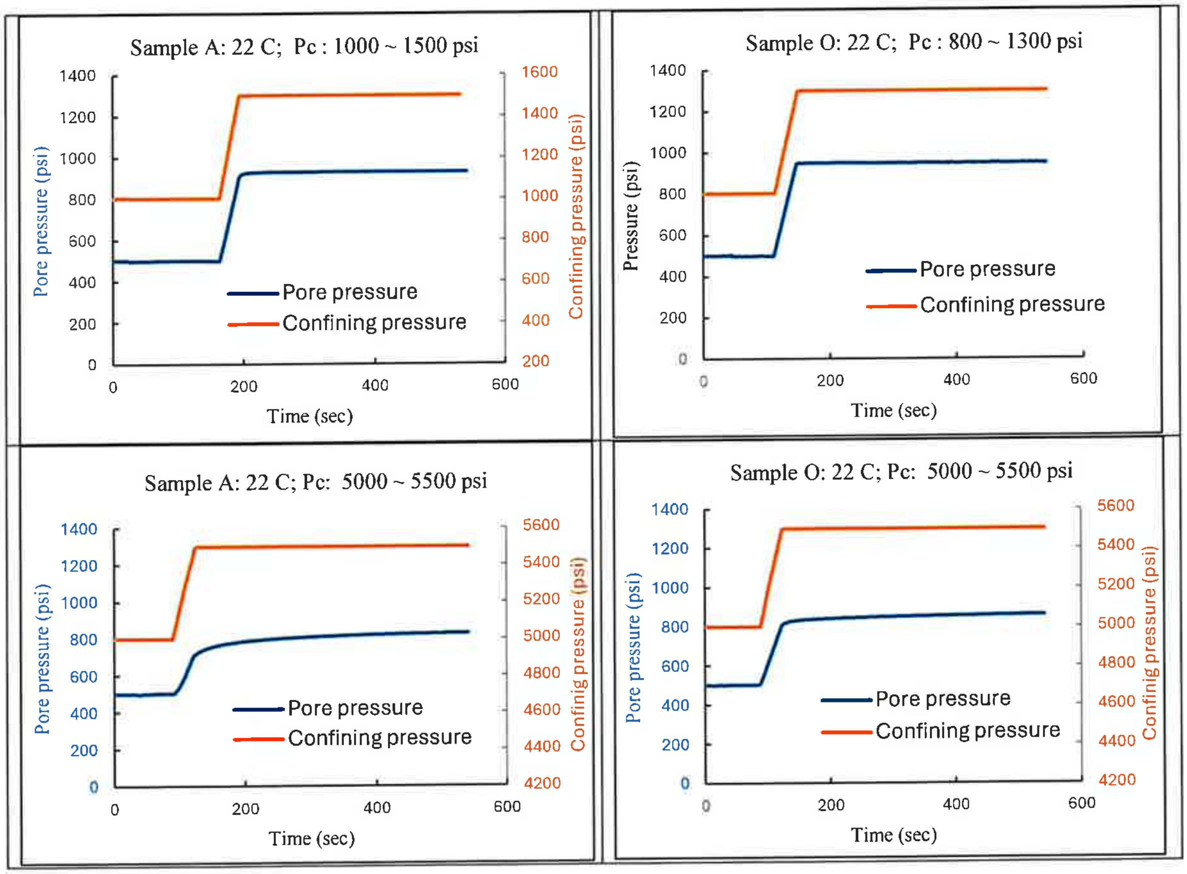

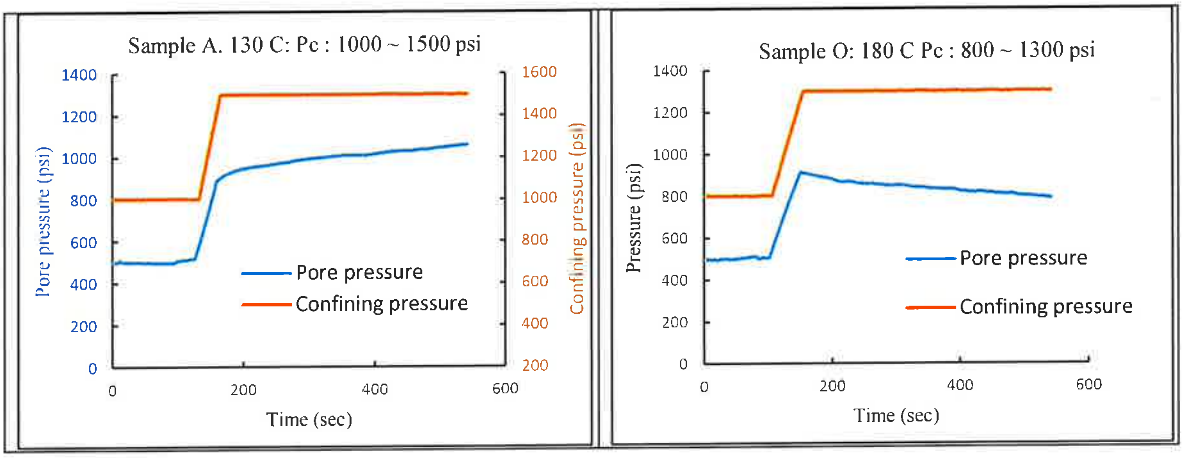

Figure 5.10. Both Samples A and O exhibit nearly perfect elastic responses under undrained conditions at low confining pressure and room temperature. At higher pressures, both samples display time-dependent creeping behavior. Under elevated temperature conditions, Sample A shows more pronounced creep, while Sample O demonstrates stress relaxation. However, creep is more commonly observed and more intuitive, as it involves continued deformation under constant stress. In contrast, stress relaxation may occur under specific conditions due to complex thermo-hydro-mechanical interactions within the rock, such as pore pressure dissipation, fissure closure, or internal stress redistribution at elevated temperatures.

5.3. Skempton’s B of Fractured Rock as Dual Porosity Medium

Fractured rocks often exhibit complex hydro-mechanical responses due to their inherent dual porosity structure, consisting of a porous rock matrix intersected by a network of fractures. This dual porosity significantly influences fluid flow and pore pressure evolution under mechanical loading, making the characterization of their poroelastic behavior challenging. Skempton’s B coefficient, a key parameter describing pore pressure response under undrained loading, provides valuable insight into the coupled behavior of fractured rocks. Unlike intact porous media, fractured rocks can show time-dependent and stress-dependent variations in B due to fluid exchange between the matrix and fractures.

Figure 5.11. Sample E before and after splitting. The fracture is a sub-horizontal, rough tensile fracture.

This section explores the distinctive features of Skempton's B in fractured rock, emphasizing the implications of dual porosity on their undrained response and highlighting the mechanisms driving deviations from classical poroelastic theory. The specimen used is Sample E, the images of this sample before and after splitting are shown in Figure 5.11. Before splitting, the Sample's information and non-destructive dynamic properties can be summarized in the following Table 5.1 and 5.2. The Skempton's B coefficient of the intact rock was measured under room temperature conditions and is shown in Figure 5.12.

Table 5.1. Sample information.

Well UF-(78-32)	Depth		Length	Diameter	Density
Sample ID	ft	m	mm	mm	g/cm^3
E	8522.70	2597.72	85.70	38.10	2.75

Table 5.2. Dynamic test results of Sample E.

Confining Pressure		Bulk Density (g/cm^3)	Ultrasonic Wave Velocity				Dynamic Elastic Parameter			
			Compressional		Shear		Young's Modulus (GPa)	Poisson's Ratio	Bulk Modulus (GPa)	Shear Modulus (GPa)
psi	MPa		m/sec	msec/m	m/sec	msec/m				
1000	6.9	2.75	3327	300.6	2147	465.87	28.97	0.14	13.54	12.67
2000	13.79		3833	260.9	2334	428.52	36.1	0.21	20.42	14.97
3000	20.69		4069	245.8	2440	409.85	39.92	0.22	23.71	16.37
4000	27.58		4128	242.2	2482	402.85	41.23	0.22	24.27	16.94

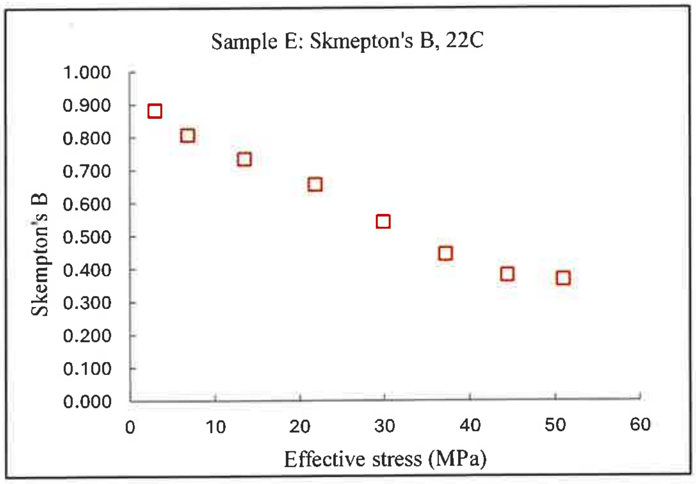

Figure 5.12. Measured Skempton's B coefficient of the intact rock under room temperature conditions.

After splitting, the fracture surfaces were scanned, as shown in Figure 5.13.

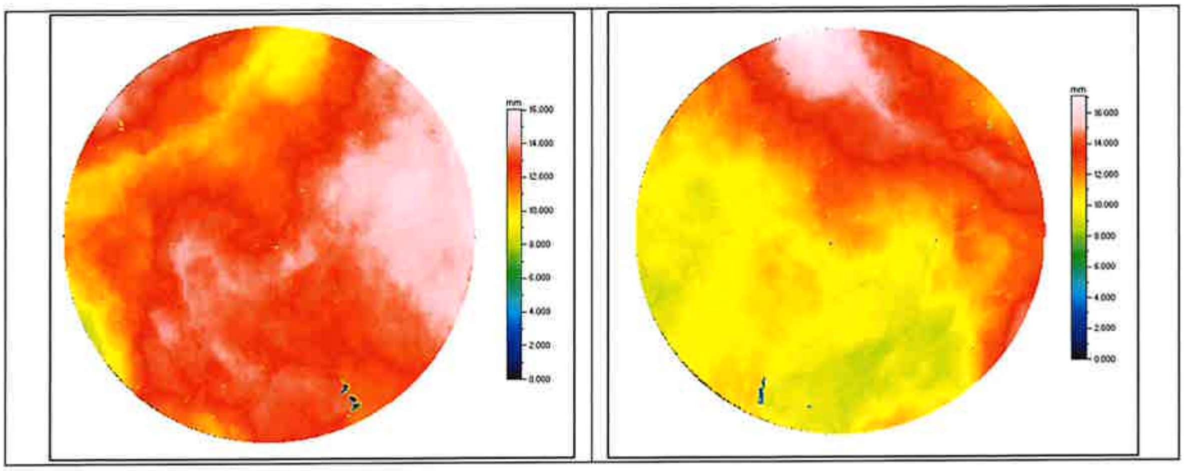

Figure 5.13. Left: long side fracture surface scan / JRC: 24.05; Right: short side fracture surface scan / JRC :22.41. These surfaces exhibit the highest level of roughness according to the Joint Roughness Coefficient (JRC) profiles developed by N. Barton (Barton & Choubey, 1977). The estimated JRC values exceed 20, placing them beyond the calibrated range of Barton's original empirical model. Thus, these fractures can be considered as the roughest ones.

The test configuration can be described in Figure 5.14.

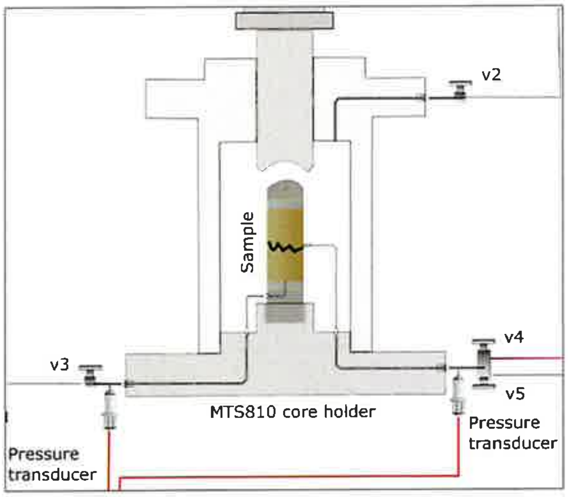

Figure 5.14. Two pore pressure transducers used in the test: one monitoring the pore pressure within the rock matrix and the other monitoring the fracture zone.

During the measurement of Skempton's B coefficient on the fractured rock, both the fracture and the rock matrix initially respond almost identically to increments in confining pressure, suggesting good hydraulic connectivity and pressure equilibrium between the two domains under low stress and room temperature conditions. As confining pressure and/or temperature increase, their responses begin to diverge. At intermediate pressure or temperature levels, the pore pressure response measured in the fracture increases more rapidly than in the matrix, resulting in two diverging curves. Over time, these curves may temporarily converge, implying delayed fluid exchange or partial pressure equilibration between the fracture and matrix. However, at higher stress levels, the divergence becomes more pronounced. This behavior indicates a reduction in permeability between the two domains—likely due to mechanical closure of microcracks or increasing resistance to flow across the matrix-fracture interface. Additionally, the increasing separation may reflect time-dependent deformation (creep) concentrated along the fracture, which further decouples it from the surrounding matrix.

The progression of these behaviors can be clearly observed in the following figures, which highlight the evolving responses of the fracture and matrix under varying stress and temperature conditions.

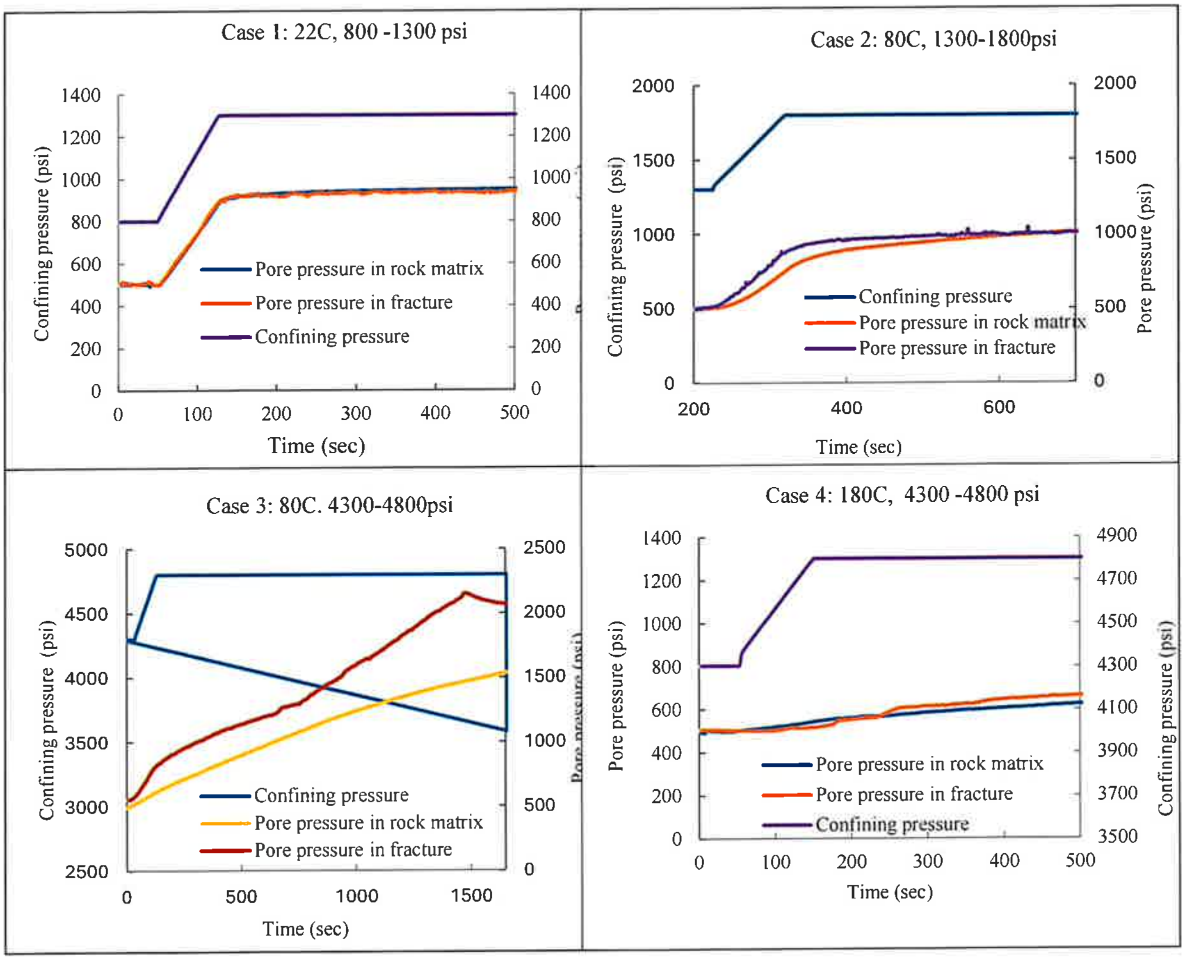

Figure 5.15. The pore pressure responses in the rock matrix and fractures under different temperatures and pressure conditions.

Case 1 (low temperature and low pressure): The pore pressures in the matrix and fracture respond almost identically to the confining pressure increment, indicating good hydraulic communication. Pore pressures remain stable over time, indicating a perfect elastic scenario.

Case 2 (intermediate temperature and pressure): The fracture initially exhibits a greater pore pressure response than the matrix, but the two converge over time. This is the most commonly observed behavior, with Elastic B in fracture consistently higher than Elastic B in matrix.

Case 3 (intermediate temperature, high pressure): The responses of the matrix and fracture diverge over time, suggesting poor hydraulic communication between the two domains. High effective stress effectively reduces the rock permeability.

Case 4 (high temperature and high pressure): The fracture experiences overclosure, resulting in an even lower Elastic B than the matrix. Both domains show minimal pressure response thus very low B due to rock consolidation.

The test results can be summarized in the following Figure 5.16.

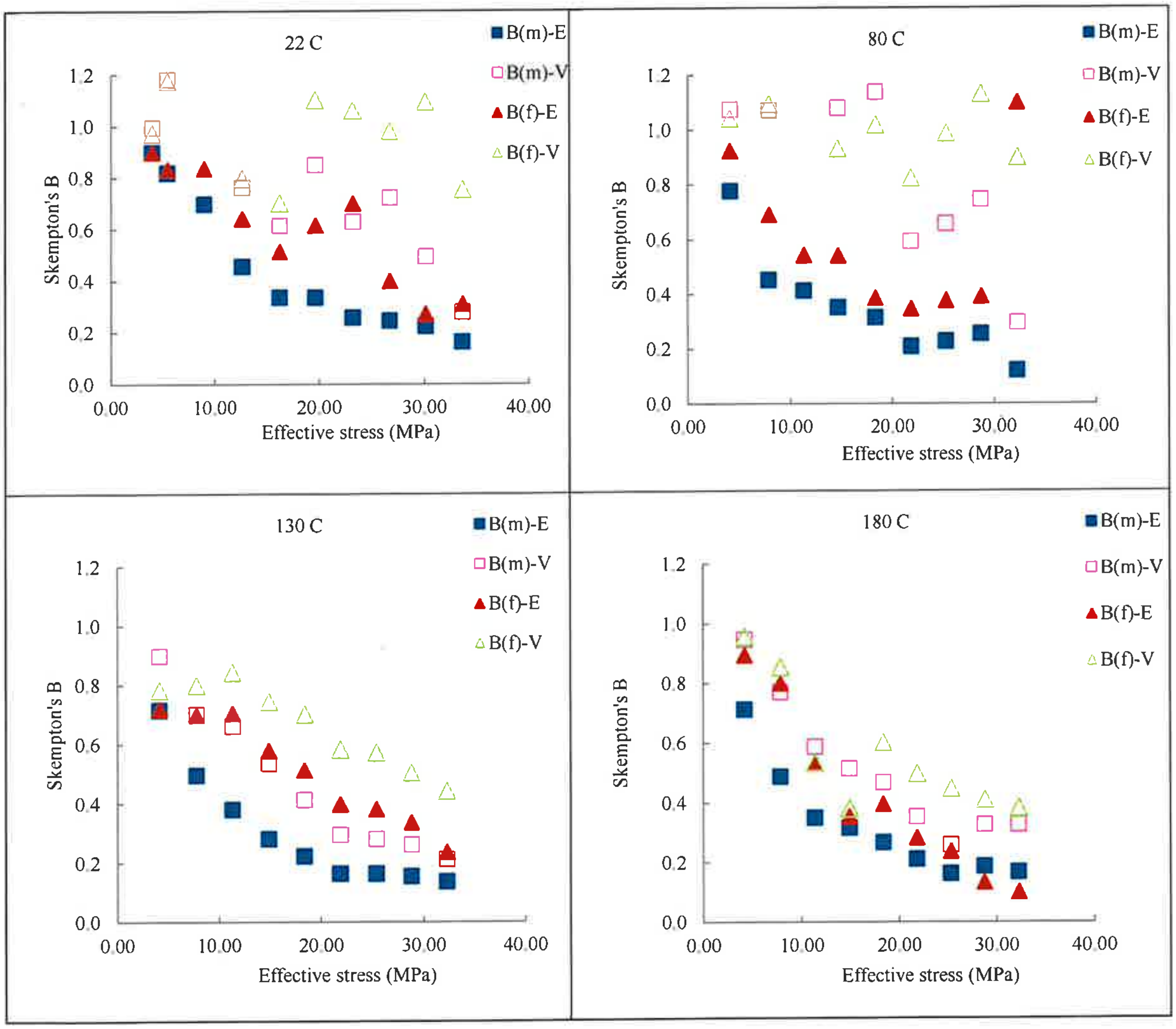

Figure 5.16. Elastic and viscous-affected Skempton's B values at different temperatures for both the rock matrix and fracture domains. B(m)-E refers to the elastic Skempton's B of the matrix, measured immediately after the confining pressure increase. B(m)-V represents the viscous-affected B of the matrix, measured after 5 minutes once the confining pressure has stabilized. B(f) denotes Skempton's B associated with the fracture response. This comparison highlights the influence of temperature on both immediate (elastic) and time-dependent (viscous) pore pressure behavior in different domains.

These results show that: (1) For the rock matrix, poroelastic Skempton's B values are consistently constrained between 0 and 1, as theoretically expected. In contrast, the viscous-affected Skempton's B values can exceed 1, reflecting delayed pore pressure equilibration caused by time-dependent deformation (creep) and fluid redistribution under low-permeability conditions. (2) Skempton's B in the fracture is generally higher than that in the matrix, reflecting the greater compliance of fractures. At 130 °C, the two sets of data—matrix and fracture—exhibit a consistent and well-correlated trend, which may indicate that the two domains are well differentiated due to partial closure of fine fissures. This separation enhances the distinction between matrix and fracture responses while preserving effective hydraulic communication within each domain. (3) At very high temperature (180 °C) and elevated confining pressure, Skempton's B in the fracture becomes even lower than that in the matrix due to fracture overclosure, which reduces compressibility and pore pressure response in the fracture domain. (4) Because the fracture is a cutting through fracture across the sample, thus it is initially highly compliant, its viscous effects are more pronounced at lower temperatures (22 °C and 80 °C). These effects diminish at higher temperatures (130 °C and 180 °C), likely due to thermally induced changes in fracture aperture, historical loading path and fluid mobility, which reduce time-dependent pressure evolution.

6. Thermal Kaiser Effect and Thermo-mechanical Response During Temperature Cycling

Thermal cycling, which involves repeated heating and cooling of rock, induces mechanical stress that can lead to microcrack formation and propagation. These thermal-induced cracks are particularly prevalent in brittle rocks, such as granite, where differential thermal expansion between minerals generates localized internal stresses (Fredrich and Wong, 1986; Tarasov and Ghassemi, 2013). While thermal cycling has been studied extensively, the effects of these cycles on microcrack evolution—especially when combined with mechanical stress—remain less understood (Darot et al., 1992). Also, as mentioned before, it is not always apparent whether cracks formed during heating or cooling. This requires continuous dynamic measurements and AE recording during the heating and cooling cycles (Daoud et al., 2020; Griffiths et al., 2024). Recent research has started to explore the interaction between thermal cycling and stress, but the underlying mechanisms of microcrack formation and propagation in these complex environments are still not fully characterized (Griffiths et al., 2018; Ge and Sun, 2018; Reuschle et al., 2006). AE signals, generated by the rapid release of energy due to crack formation and propagation, provide valuable real-time information about the mechanical response of rocks (Obert, 1977; Wang et al., 1989). AE activity has been shown to correlate closely with temperature changes during thermal cycling; the degradation of macro-properties of the rocks is largely attributed to the generation of grain boundary and intra-grain micro-cracks due to thermal stress (Rong et al., 2018). This makes AE monitoring an essential tool for tracking damage progression and understanding rock failure mechanisms in geothermal systems. For example, Ge and Sun (2018) and Bu et al. (2024) recorded AE in uniaxially loaded samples subjected to heating and cooling and noted microcrack initiation in granite during thermal cycling. These studies observed increased AE during temperature ramps and cycles, highlighting the sensitivity of AE to thermal loading.

In this work we investigate the thermo-mechanical response of the Utah FORGE granitoid under confining pressure. The effects of thermal cycling on triaxially loaded granitoid core plugs are studies using continuous dynamic measurements and AE monitoring. By subjecting the rocks to multiple heating and cooling cycles at varying peak temperatures, while continuously monitoring AE activity and dynamic properties, this research improves the understanding of microcrack development and propagation during thermal cycling under in-situ stress conditions. The findings have practical applications for improving core-based stress measurement techniques, log interpretations and the design of thermal stimulation strategies.

6.1. Sample Preparation and Test Procedures

This sample is retrieved from a depth of 8523 ft of Well 78-32. Its image and thin section are shown in Figure 6.1. Its basic information and minerology are summarized in Table 6.1 and 6.2, respectively. Its quartz composition is lower than expected from a typical granitoid, indicating dilution by secondary minerals.

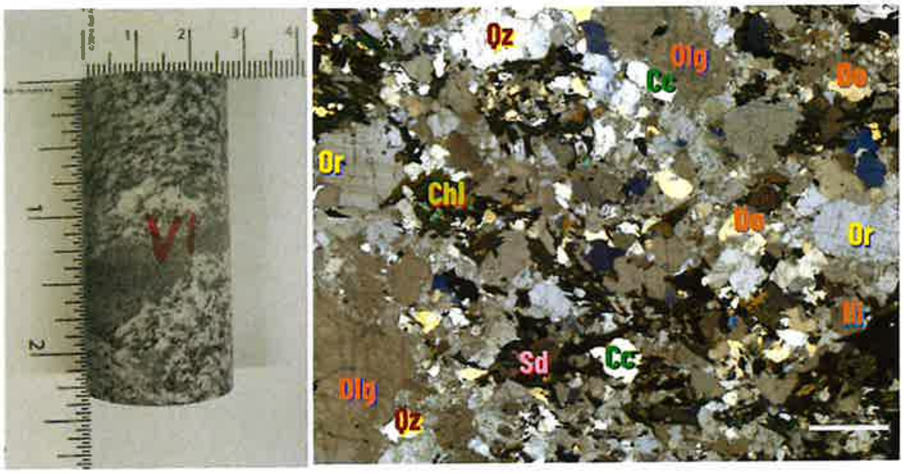

Figure 6.1: Sample image (left) and thin section (right white bar length is 1 mm).

Table 6.1. Sample information.

Well ID	Sample No.	Depth		Length (mm)	Diameter (mm)	Weight (g)	Density (g/cm^3)	Hardness
		(ft)	(m)					
78-32	V1	8523	2598	52.86	25.26	74.64	2.82	721

This sample's mineralogy by FTIR test is summarized in Table 7.2.

Table 6.2. Sample mineralogy in percent.

Quartz	Calcite	Dolomite	Illite	Smectite	Chlorite	Orthoclase	Oligoclase	Siderite
14	8	6	20	3	3	4	40	2

Note the high proportion of plagioclase feldspar (oligoclase), 40%, aligns with a granitoid's classification but suggests a more plagioclase-rich composition, which is consistent with quartz monzonite. The presence of 20% illite is unusual for an unaltered granitoid, suggesting significant alteration or secondary processes, such as hydrothermal activity or weathering. The presence of calcite, dolomite, and siderite totaling 16% indicates secondary mineralization from hydrothermal interactions including chemical alteration. These carbonates are not primary minerals in granitoids. This composition is consistent with a granitoid that has been subjected to hydrothermal fluid activity at depth. The relatively low quartz content and the presence of significant secondary minerals like illite, smectite, chlorite, and carbonates indicate post-magmatic alteration. This aligns with the geothermal environment of Utah FORGE, where deep-seated rocks are altered by circulating hot fluids. The presence of clay minerals introduces unexpected complexities in the rock mechanical response of the sample.

The in-situ stress estimation is based on the understanding that the vertical stress (S_v) gradient is 1.13 psi/ft, the minimum horizontal stress (S_h) is 0.74 psi/ft, the maximum horizontal stress (S_H) is in a range of 0.83 to 0.98 psi/ft, and pore pressure is 0.433 psi/ft (Ye et al., 2022). Based on these data, the effective mean stress at 8522ft depth is 3979 psi (using S_H=0.83) to 4405 psi (using S_H=0.98). In this test, we take the value of 4000 psi as the effective mean stress for this sample and use 2000 psi axial differential stress. For the temperature, based on the literature review, the reservoir temperature at this depth is in a range of 175 to 215°C (Di Drill Survey, 2021), thus 180 ~ 190 °C is taken as the in-situ temperature for this sample during the test. The experiment is conducted using an MTS 810 testing frame, which has a maximum axial load capacity of 250 kN, equivalent to 493 MPa on a 1-inch diameter sample. Control and data acquisition are managed through MTS Series 793™ Control software. Axial displacement of the rock sample is monitored using two LVDT sensors mounted on the sample, while a third LVDT attached to a radial chain measures transverse displacement with an associated error of ±0.05%. Temperature is regulated by a heating element around the cell, with a thermocouple installed inside the chamber to provide real-time temperature readings. Mechanical parameter measurements, including displacement and stress, are recorded throughout the loading process to evaluate the thermo-mechanical coupling behavior of the rock sample (Figure 6.2).

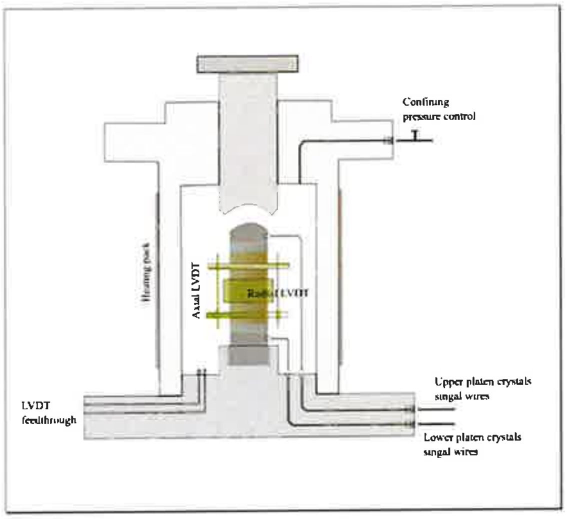

Figure 6.2. Schematic testing configuration.

This test procedure is divided into three main phases: (1) Stress Application, (2) Heating-Cooling Cycling, and (3) Triaxial Multistage Test.

Part 1: Stress Application at Room Temperature

1. Install the rock sample into the cell and verify the signal quality of the LVDTs and acoustic sensors. Only proceed if the signals are acceptable.
2. Close the cell, fill it with mineral oil, and apply an initial confining pressure of 10 psi. Measure the compressional (Vp) and shear wave velocities (Vs).
3. Increase the confining pressure linearly from 10 psi to 1000 psi over 20 minutes, recording acoustic emission (AE) activity and LVDT displacement responses.
4. Hold the confining pressure at 1000 psi and measure Vp and Vs.

5. Gradually increase the confining pressure from 1000 psi to 2000 psi over 20 minutes, recording AE activity, LVDT responses, and bulk modulus changes.
6. Hold the confining pressure at 2000 psi and record Vp and Vs.
7. Repeat steps 5–6, increasing the confining pressure incrementally by 1000 psi until reaching 6000 psi. After recording Vp and Vs at 6000 psi, reduce the confining pressure to 4000 psi.
8. Maintain the confining pressure at 4000 psi, then increase the axial differential stress to 2000 psi. Record AE activity during this loading phase and measure Vp and Vs under these stress conditions, simulating in-situ stress for the sample.

Part 2: Acoustic Emission During Temperature Cycling

9. Maintain a confining pressure of 4000 psi and an axial differential stress of 2000 psi. Gradually heat the sample from room temperature (25°C) to 60°C at a rate of 0.33°C/min, recording AE activity throughout the heating process.
10. Allow the sample to cool back to room temperature, recording AE activity during the cooling phase.
11. Conduct additional heating-cooling cycles: raise the temperature to 90°C and then cool to 30°C, recording LVDT responses, Vp/Vs, and AE signals.
12. Repeat the cycle in Step 11 for maximum temperatures of 120°C, 150°C, and 180°C, completing a total of five cycles. The procedure involves heating the sample during the daytime and allowing it to cool down overnight. This schedule ensures sufficient time for controlled heating and natural cooling, enabling accurate monitoring of the rock's thermal and mechanical responses in each cycle. Based on calculations, the cell temperature is a reliable indicator of the sample's temperature. Given the slow heating rate of 0.33°C/min and the system's high thermal conductivity, the temperature at the center of the granite rock closely aligns with the oil temperature near the wall, ensuring accurate monitoring.

Part 3: Triaxial Multistage Test at 180°C

13. At a constant temperature of 180°C, perform a multistage triaxial compression test starting with a confining pressure of 4000 psi. Use a loading rate of 1×10^{-3} mm/s (adjust if necessary) and unload the sample at the dilation point. Repeat the test at confining pressures of 3000 psi and 5000 psi, unloading at the dilation point for each stage.
14. For the final stage, return the confining pressure to 4000 psi and perform a triaxial compression test, continuing to load until the sample fails.
15. Cool the sample back to room temperature and complete the test. Remove the sample, document its condition with photographs, and clear the test station.

This structured methodology ensures the thorough characterization of the thermo-mechanical and acoustic responses of the sample under controlled laboratory conditions.

6.2. Experimental Results and Data Analysis

6.2.1. Dynamic Properties and AE Behavior During Stress Application

The rock's dynamic properties and initial acoustic emission (AE) behavior were obtained during the first phase, referred to as the stress installation stage. The dynamic test results for the Utah FORGE rock reveal a clear relationship between effective stress and the rock's mechanical properties (Table 6.3 and Figure 6.3). As effective confining stress increases from 0.34 MPa to 41.37 MPa (50 to 6000 psi), the compressional wave velocity (Vp) and shear wave velocity (Vs) consistently rise, reaching values of 5182.35 m/s and 2753.13 m/s, respectively. This increase in wave velocities reflects the rock's densification and reduction in pore/microcrack space under higher stresses, enhancing its stiffness. Correspondingly, the dynamic Young's modulus (Ed) shows a steady increase from 33.27 GPa at low stress to 55.67 GPa at the highest confining pressure, indicating significant improvement in the rock's ability to resist deformation as confining pressure increases. The dynamic Poisson's ratio shows a gradual increase from 0.24 to 0.30, indicating a shift in the rock's elastic response under stress, with greater lateral deformation relative to axial deformation, suggesting less compressibility.

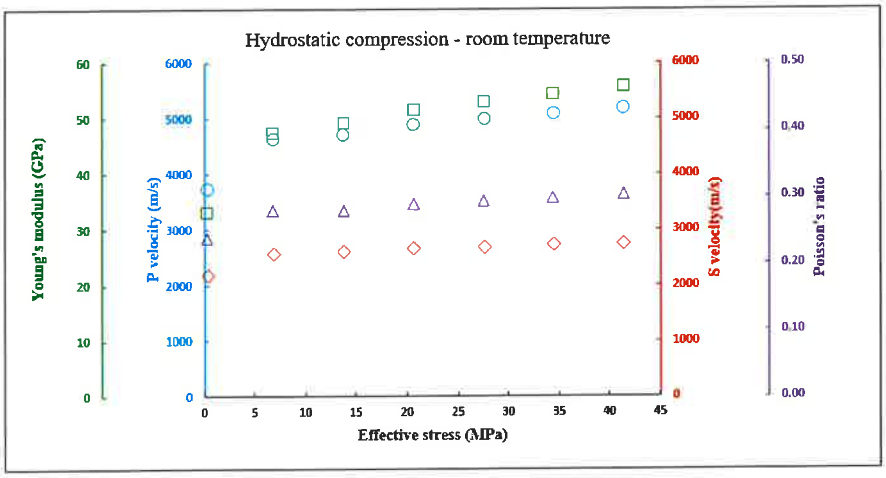

Figure 6.3. Dynamic test results under room temperature with increased effective stress.

Table 6.3. Dynamic test results at room temperature.

Effective stress (MPa)	Effective stress (psi)	Vp (m/s)	Vs (m/s)	Ed (GPa)	Dynamic Poisson's ratio
0.34	50	3722.54	2184.30	33.27	0.24
6.90	1000	4636.84	2566.02	47.47	0.28
13.79	2000	4719.64	2616.83	49.32	0.28
20.69	3000	4894.44	2669.70	51.74	0.29
27.58	4000	4986.79	2696.94	53.01	0.29
34.48	5000	5082.69	2724.74	54.32	0.30
41.37	6000	5182.35	2753.13	55.67	0.30

6.2.2. Acoustic Emission and Deformation Behavior During Thermal Cycling

Under a constant stress boundary condition of 4000 psi confining pressure and an axial differential stress of 2000 psi, thermal cycling was conducted. This part of the test spanned approximately 3.88×105 seconds (about 4.5 days). Heating was performed at a controlled rate of 0.33°C/min, slow enough to ensure thermal equilibrium within the system. Cooling, on the other hand, occurred naturally at an even slower rate. The five thermal cycles corresponded to target temperatures of 60°C, 90°C, 120°C, 150°C, and 180°C, with distinct heating and cooling phases as shown in the lower portion of Figure 6.4.

During thermal cycling, the deformation of the rock sample was predominantly axial, with minimal lateral strain. Axial strain and acoustic emission (AE) activities are illustrated in the upper portion of Figure 6.4. Specifically, the filtered (to eliminate noise) cumulative acoustic emission (CAE) closely mirrored the axial strain behavior. When the axial strain changed, the CAE exhibited a corresponding rise. When axial strain plateaued, AE activity stabilized accordingly.

During these thermal cycles, the axial shortening during the heating stages of 60°C, 90°C, 120°C, and 150°C, indicates progressive compaction. This behavior contrasts with the expected thermal expansion based on the granite's thermal expansion coefficient, which would typically result in elongation (strain decrease). The observed compaction suggests that thermally activated deformation mechanisms such as dislocation glide, grain boundary sliding, or microcrack closure may be dominant, leading to inelastic shortening of the sample under differential stress. However, at the heating stage of 180°C, the strain decreased, possibly reflecting the onset of thermal expansion overcoming the compaction effect or a reduction in creep activity as the creeping effect diminishes after sample became more consolidated.

During the cooling phases, the strain remained constant during cooling from 60°C to room temperature (RT), from 90°C to RT, and from 120°C to RT, suggesting that the compaction observed during heating was not reversible and no further deformation occurred during cooling. However, during the cooling phases from 150°C to RT and 180°C to RT, the strain increased, indicating additional compaction. This behavior may result from thermally induced stress redistribution or further microcrack closure as the temperature decreased, particularly under the influence of the newly increased temperature and the applied triaxial stress. These observations underscore the intricate interplay between thermal expansion, thermal-stress-driven compaction, and temperature-dependent deformation mechanisms in controlling the granite's response under cyclic thermal loading.

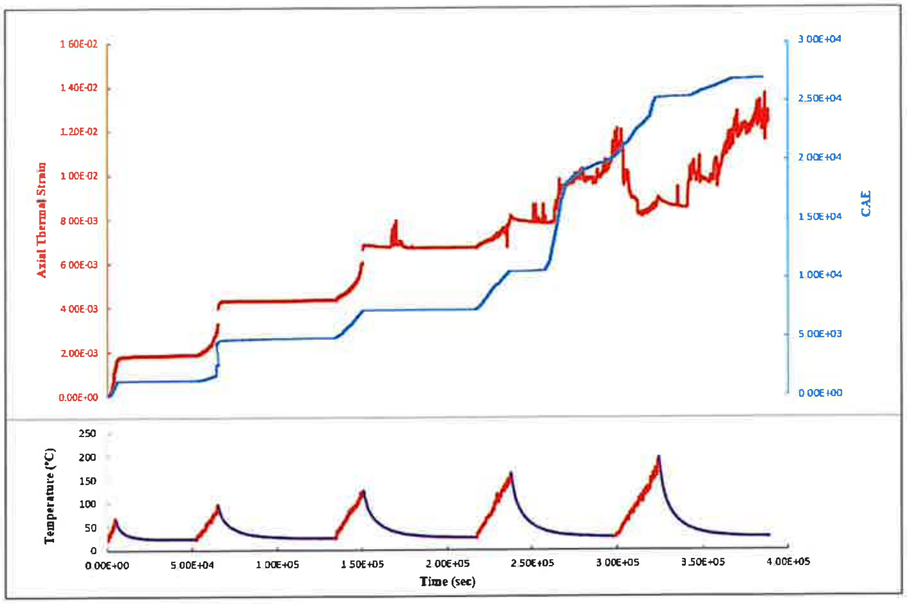

Figure 6.4. Temperature, axial thermal strain and CAE over time.

During the cooling phases after reaching 150°C, AE activity exhibited a pronounced surge, deviating from the quiet behavior observed in the first three cooling cycles. This surge in AE activity coincided with an increase and fluctuation in axial strain, indicating compaction of the rock. In the initial three thermal cycles, AE activity—a proxy for thermal crack development—was predominantly associated with the heating phases, while cooling phases exhibited minimal AE activity. However, in the last two cycles (cooling from 150°C to 25°C and 180°C to 25°C), AE activity significantly intensified. The surge during the first cooling phase (150°C–25°C) was notably stronger than the second (180°C–25°C), since new cracking requires surpassing previously experienced thermal paths. This behavior can be interpreted as a form of the thermal Kaiser effect.

These AE surges were consistently accompanied by axial strain fluctuations, indicating that thermal cracks induced during cooling contributed to measurable changes in the rock's geometry. The shift in behavior during cooling phases highlights a transition in the rock's response to thermal stress. These findings align with the observations of Daoud et al. (2020), who also reported AE surges during cooling phases. Their work demonstrated that thermal cracking predominantly occurs during heating in coarse-grained granophyre but shifts occur during cooling in finer-grained andesite and basalt. Notably, the rock tested in this study exhibits a mixed grain structure, consisting of both coarse and fine grains, or a bimodal texture, which may potentially contribute to the observed behavior.

7.2.3 Dynamic Properties During Thermal Cycling

Compression and shear wave velocities have also been measured during thermal cycling. The dynamic test results of the Utah FORGE rock, while maintaining consistent stress boundary conditions with 4000 psi confining pressure and 2000 psi axial differential stress, reveal a clear temperature-dependent degradation of the rock's elastic properties (Table 6.4 and Figure 6.5). Initially at room temperature (25°C), the compressional wave velocity (Vp) and shear wave velocity (Vs) are highest, at 5286.00 m/s and 2841.94 m/s, respectively, correlating with a high dynamic Young's modulus (Ed) of 59.02 GPa and a dynamic Poisson's ratio of 0.29. As the temperature increases over cycling, both Vp and Vs decline, with Vp showing a more pronounced decrease. By 180°C, Vp has dropped to 4556.90 m/s, Vs to 2381.08 m/s, and the Young’s modulus to 42.92 GPa, representing a substantial reduction in stiffness and wave propagation capacity.

Table 6.4. Dynamic results during thermal cycling.

Temperature	Vp	Vs	Ed	Dynamic Poisson’s ratio	K	S
(°C)	(m/sec)	(m/sec)	(GPa)		(GPa)	(GPa)
25	5286.00	2841.93	59.01	0.29	48.39	22.76
60	5182.35	2872.82	59.44	0.27	44.67	23.25
25	4986.79	2811.70	56.44	0.26	40.37	22.28
90	5182.35	2782.10	56.59	0.29	46.59	21.81
25	4986.79	2811.70	56.44	0.26	40.37	22.28
120	5082.69	2566.01	49.31	0.32	48.05	18.55
25	5182.35	2811.70	57.53	0.29	45.97	22.28
150	4894.44	2470.09	45.69	0.32	44.58	17.19
25	5082.69	2782.10	56.09	0.28	43.71	21.81
180	4556.89	2381.08	41.92	0.31	37.21	15.97
25	5082.69	2782.10	56.09	0.28	43.71	21.81

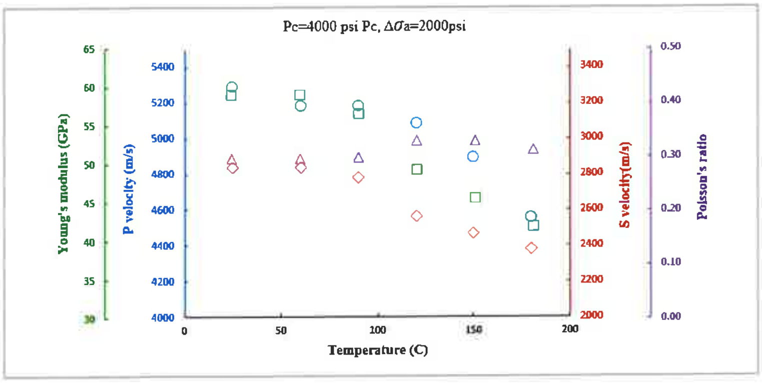

Figure 6.5. Dynamic test results under constant stress boundary conditions with increased temperature.

The observed trends underscore the thermal sensitivity of the rock, likely due to microstructural changes such as thermal expansion, crack initiation, and changes in mineral bonding strength. The shear wave velocity (Vs) displayed a monotonic decrease with increasing temperature. Thus, the shear modulus (calculated by $G = \rho Vs^2$), also diminished. A decreasing shear modulus usually indicates that the rock sample becomes progressively softer over the heating-cooling cycle.

After each cooling phase, the rock strength appears to recover partially, as indicated by the reversely increased Vp and Vs measured under room temperature. This recovery may result from the closing of some thermally induced microcracks due to contraction during cooling, stress redistribution, or structural realignments within the rock. Additionally, the presence of clays could play a role in this process, as their plasticity and potential to swell or contract with temperature changes may contribute to closing or aligning microcracks.

Comparing the final dynamic Young's modulus (Ed) at 180°C (41.92 GPa) with that at room temperature (59.01 GPa initially and 56.09 GPa after the last cooling cycle) shows a significant reduction in stiffness with increasing temperature, indicating irreversible thermal damage despite partial recovery after cooling. Comparing the strength data between room temperature and elevated temperatures would provide greater confidence in the results and offer deeper insights into the extent of structural changes occurring within the rock during thermal cycles.

7.2.3. Multistage test at 180°C

After the thermal cycling test, the temperature was raised to 180°C and maintained consistently, while a multistage test was conducted on the rock. Despite experiencing some thermal damage from the previous cycling, the rock retained significant strength.

During the multistage loading test, confining pressures of 4000, 3000, and 5000 psi were applied sequentially, with axial load increased to the dilation point in each stage before unloading. The dilation point is identified by monitoring the behavior of the volumetric strain curve, specifically when the tangent line of this curve begins to approach a vertical orientation. In the final stage with the confining pressure returned to 4000 psi, the axial load was applied to failure. The stress-strain behavior showed nonlinear elasticity during initial loading for each stage, as microcracks formed by differential thermal expansion closed under pressure, increasing stiffness. In the final stage, rapid and violent crack propagation led to failure, with a significant drop in residual stress. Elevated temperature and pressure activated deformation mechanisms such as grain boundary sliding and crystal plasticity, facilitating plastic deformation prior to failure. A well-developed shear fracture was evident, as marked on the copper jacket (Figure 6.6).

Figure 6.6. Distinct trace of a well-developed shear fracture marked on the copper jacket after rock failure.

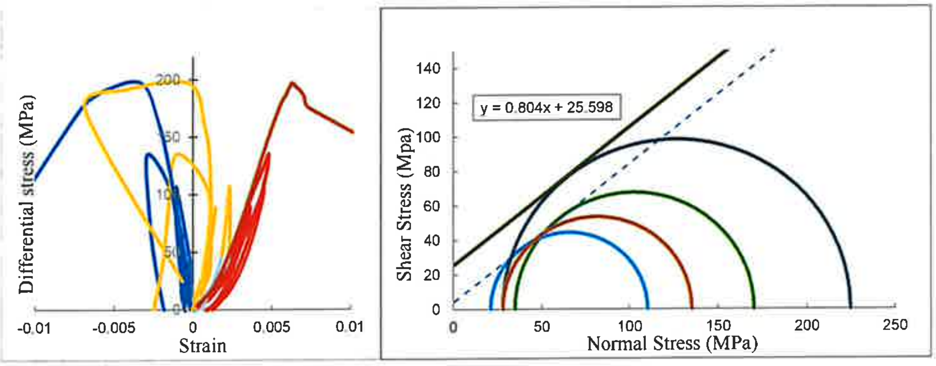

Figure 6.7. Stress-strain curve (left) and Mohr Coulomb analysis (right) of the multistage test.

Overall, this rock exhibits an intermediate Young's modulus and compressive strength, likely due to its texture and mineral composition. There is a strong correlation between the static and dynamic moduli, as well as Poisson's ratio. Both static and dynamic moduli decrease with increasing temperature (Table 6.5). At a 4000psi confining pressure, static Young's modulus was measured under room temperature and 180°C conditions, showing a reduction in both static and dynamic moduli with higher temperature.

Table 6.5. Variation of elastic and Poisson's ratio during multistage test.

Temperature (°C)	Pc (psi)	Es (GPa)	Static Poisson's ratio
180	3000	42.91	0.21
180	4000	42.27	0.24
180	5000	46.17	0.30
180	4000 (failure)	42.16	0.31

The comparison of static and dynamic Young's moduli at room temperature (25°C) and elevated temperature (180°C) reveals notable differences and trends (Table 6.6). Initially, at 25°C and a confining pressure of 4000 psi, the static Young's modulus (48.33 GPa) is significantly lower than the dynamic modulus (59.02 GPa). This difference likely reflects the influence of horizontal fissures and microcracks within this vertical sample, which could usually be caused by the core retrieving process due to the release of overburden stress. Such horizontal fissures typically have a more pronounced impact on static measurements than on dynamic ones. After multiple thermal cycles, both moduli exhibit a noticeable decrease with increasing temperature, indicating thermal damage to the rock. However, although the sample experienced overall thermal damage, its structure appears to compact over several days' triaxial stress conditions due to compaction effect, resulting in a smaller difference between the static (42.27 GPa) and dynamic (42.92 GPa) moduli at 180°C.

Table 6.6. Variation of elastic and Poisson's ratio during multistage test.

Temperature	Pc (psi)	Static E (GPa)	Dynamic E (GPa)
25	4000	48.33	59.02
180	4000	42.27	42.92

6.2.4. Thermal Kaiser Effect

In this experiment, we also observed variations in cumulative acoustic emission (CAE) during the cooling phases at different peak temperatures, which provide insights into the potential manifestation of the Thermal Kaiser effect. After heating the rock to 150°C, a significant increase in CAE was detected during the cooling phase, indicating active microcrack initiation. In contrast, after heating to 180°C, although some CAE was still recorded, the magnitude of the response was much smaller. This reduction in CAE during the cooling phase at higher temperatures aligns with the Thermal Kaiser effect, suggesting that the material "remembers" its previous thermal damage history. The rock's microstructural and mechanical state at elevated temperatures likely plays a crucial role in shaping its behavior during cooling, reducing the reactivation of pre-existing cracks and influencing the overall thermal damage progression.

The Thermal Kaiser effect has broader implications for understanding how rocks behave under cyclic thermal stress. This effect proposes that pre-existing thermal damage influences the rock's response to subsequent heating and cooling, leading to a diminished acoustic response and slower mechanical degradation. As the rock undergoes repeated thermal cycling, its microstructure stabilizes, which can reduce the propagation of microcracks and slow the rate of thermal damage. These findings underscore the complex interplay between thermal history, crack evolution, and the material's long-term behavior, highlighting the importance of considering temperature memory when assessing the durability of rocks in geothermal environments.

6.3. Thermal Kaiser Effect in Rock During Cyclic Heating

6.3.1. Discussion

The experimental results provide a comprehensive understanding of the thermo-mechanical behavior of granitoid cores from the Utah FORGE site under simulated geothermal reservoir conditions. The dynamic properties of the rock sample at room temperature reveal that increasing effective stress significantly enhances the rock's stiffness, which is evidenced by higher compressional (Vp) and shear wave (Vs) velocities, along with an increase in the dynamic Young's modulus (Ed). These changes are attributed to the closure of microcracks and voids under elevated confining pressures, highlighting the rock's potential to maintain mechanical integrity under the in-situ stress conditions typical of geothermal reservoirs.

Thermal cracking in rocks involves complex interactions during both heating and cooling phases. In our thermal cycling tests on the specimen retrieved from core at 8523 ft, the cumulative acoustic emission (CAE) closely mirrored axial strain behavior, reflecting the rock's macro-scale deformation driven by internal micro-scale grain rearrangement and microcrack activities, including crack initiation, propagation, and closure. Notably, CAE increased during changes in axial strain and plateaued when strain stabilized. Acoustic emissions (AEs) were detected throughout all five heating phases and the final two cooling phases.

AEs caused by heating have been widely documented (Fortin et al., 2006; Griffiths et al., 2016, 2024; Jones et al., 1997), with the mechanism being relatively straightforward due to microcrack initiation caused by grain expansion. More recently, studies have highlighted that AEs during cooling, often attributed to thermal cooling microcracks, can be as significant as those observed during heating (Browning et al., 2016; Heap, 2014; Daoud, 2020). For example, Browning et al. (2016) observed that most AE energy results from thermal cracking generated during the cooling phase rather than during the heating phase, and these findings underscore the significance of the cooling phase in thermal cracking studies, as it may contribute more substantially to rock damage than previously recognized. However, the physical mechanisms driving thermal damage-related AE during cooling remain complex and not fully understood. This complexity involves factors such as anisotropy, heterogeneity, pre-existing structural defects, thermal gradients, and heating history (Zhang et al., 2020).

Daoud et al. (2020) observed that coarse-grained granophyre predominantly exhibited thermal crack damage during heating, whereas finer-grained andesite and basalt experienced more damage during cooling. Therefore, the bi-modal texture of the FORGE core tested may contribute to microcracking during both heating and cooling thermal phases, highlighting the complex nature of thermal cracking.

The absence of AE activity during the initial three cooling phases, followed by its emergence in the last two, suggests that heating beyond 15 °C may signify thermal Kaiser effect and the activation of specific mechanisms leading to AE during subsequent cooling phases. However, relying solely on AE monitoring to assess microstructural changes may be insufficient. Griffiths et al. (2018) combined AE monitoring with velocity measurements during thermal cycling of Westerly granite (not loaded) and found that many AEs recorded during cooling might not be associated with the formation of new microcracks but rather with the closing of existing ones. This indicates that AE activity during cooling may not always signify damage but could also represent microcrack closure, akin to the sounds heard both when a door opens (crack initiation/propagation) and closes (crack sealing). In our case, we also observed that partially recovered Vp/Vs after cooling suggests that crack closure, accompanied by AE activity, might also be occurring. If this is the mechanism, the quiet cooling phases in the first three cycles may indicate that cracks produced during the previous heating processes sealed quietly, while further heating at higher temperatures may have triggered more thermal stress driven cracks, causing energy release when such cracks begin to seal.

The disparity in damage observed between the heating and cooling phases may also be attributed to changes in the overall stress state within the sample. Materials typically have a tensile strength that is approximately one-tenth of their compressive strength. As a result, cracks are more likely to form under the tensile stresses induced by cooling and contraction than under the compressive stresses associated with heating and expansion. In our test, although the confining pressure and axial stress maintained a compressive regime throughout, the transition from grain expansion during heating to contraction during cooling likely caused complex stress redistributions. These redistributions may have locally favored the formation of microcracks during the cooling phase. This process highlights how the interplay between thermal expansion, contraction, and stress state can influence microstructural damage evolution.

Studies by Heap et al. (2014) have documented varying AE activity during heating and cooling across different rock types (unstressed), with AE during cooling often attributed to thermal contraction or crack interactions. Since cooling always occurs after heating, the previous crack formation may have impacted the subsequent crack behavior, either with new cracks further developing or old crack being sealed somehow. Therefore, integrating AE monitoring with complementary techniques, such as velocity or permeability measurements, is essential for a comprehensive understanding of thermal damage mechanisms in rocks. This multifaceted approach enables a more accurate interpretation of AE data, distinguishing between crack formation, closure, and sealing processes during thermal cycling.

Furthermore, the unique mineralogical composition of the Utah FORGE rock, characterized by a high proportion of oligoclase and secondary minerals such as illite and carbonates, likely contributes to its distinct thermo-mechanical response. These secondary minerals, products of hydrothermal alteration, may weaken the rock matrix, making it more susceptible to damage under thermal cycling. This finding highlights the importance of considering mineralogical heterogeneity in geothermal reservoir characterization.

6.3.2. Conclusions

This study underscores the critical role of thermal cycling in altering the mechanical and microstructural properties of granitoid rocks under in-situ geothermal conditions. The experimental results highlight the following key findings:

Acoustic emission (AE) activity remained minimal during hydrostatic loading but surged significantly once axial differential stress was applied. The strong correlation between AE activity and axial thermal strain under a constant stress boundary condition is evident throughout all subsequent thermal cycles. Since cumulative acoustic emission (CAE) closely mirrored axial strain behavior, the rock's macro-scale deformation, driven by internal micro-scale grain rearrangement, can be effectively captured by analyzing AE, strain, and dynamic measurements.

AEs were detected during all five heating phases and the final two cooling phases. The mechanism of AE during heating is relatively straightforward, driven by microcrack initiation due to grain expansion/rearrangement. However, the mechanism of AE during cooling is more complex and difficult to interpret. The absence of AE activity during the initial three cooling phases, followed by its emergence in the final two, suggests that heating beyond 150°C may activate specific mechanisms leading to AE during subsequent cooling phases. The bimodal grain structure of the rock likely contributed to this behavior.

On the other hand, the partially recovered Vp/Vs after cooling further suggests that crack sealing, accompanied by AE activity, may also be occurring. If this is the case, the quiet cooling phases in the first three cycles may indicate that cracks produced during previous heating cycles sealed quietly, while further heating at higher temperatures may trigger more rigid cracks, leading to energy release when these cracks begin to seal. However, the physical mechanisms driving thermal related AE during cooling remain complex and not fully understood. These complexities involve factors such as anisotropy, heterogeneity, pre-existing structural defects, and thermal history. Our work provides valuable observations for further investigation into these phenomena.

Overall, repeated heating and cooling cycles induce significant and cumulative microcrack damage, as evidenced by notable axial deformation, AE activity, and reduced Vp/Vs. The damage progressively accumulates with each cycle, particularly at higher peak temperatures. The interplay between thermal damage and mechanical stress plays a crucial role in influencing the rock's failure mechanisms. Multistage triaxial tests reveal that both the dilation point and fracture propagation are sensitive to confining pressure and prior thermal cycling.

The observed variations in cumulative acoustic emission (CAE) during cooling phases at different peak temperatures also suggest the presence of the Thermal Kaiser effect, indicating that the rock "remembers" its thermal history, which influences its subsequent acoustic response. These findings highlight the role of pre-existing thermal damage in shaping the rock's mechanical degradation and emphasize the importance of considering thermal memory in assessing the long-term durability of rocks under cyclic thermal stress.

The presence of secondary minerals, such as illite and carbonates, weakens the rock matrix, likely amplify the effects of thermal cycling on mechanical properties. These minerals contribute to the rock's vulnerability to thermal damage, affecting its overall strength and response to thermal cycling.

Together, these results emphasize the intricate interplay between thermal cycling, thermal memory (thermal Kaise effect), grain structure, and the evolution of thermal cracks in thermally stressed rocks, underscoring the complexity of thermal damage mechanisms in heterogeneous materials. These findings have important implications for the design and optimization of Enhanced Geothermal Systems (EGS).

7. Laboratory Mini-frac Experiments (DFIT)

The magnitude of the reservoir minimum principal stress is generally measured through hydraulic fracturing (HF)-based tests (e.g., Hubbert & Willis, 1957; Haimson & Fairhurst, 1967; McClennan & Roegiers 1981; Hickman & Zoback, 1981), such as minifrac tests, microfrac tests, and diagnostic fracture injection tests (DFITs). During these HF-based tests, a relatively small amount of pressurized fluid is introduced into a segment of the wellbore, which is isolated using a straddle packer system, to initiate and propagate a hydraulic fracture, and then the well is shut in. In general, multiple injection and fall-off cycles are performed after the initial fracturing cycle to obtain stress measurements. During these cycles, the pressure transients in the wellbore during the injection and shut-in phases are monitored. The minimum principal stress can then be determined by interpreting the characteristics of different borehole pressures (or pressure indicators), such as fracture reopening pressure (Bredehoeft et al., 1976; Shlyapobersky, 1989; Ito & Hayashi, 1993), instantaneous shut-in pressure or *ISIP* (Hickman & Zoback,1981; Gronseth & Kry, 1981), and fracture closure pressure (Castillo, 1987; Barree & Mukherjee, 1996; Raaen et al., 2001).

Typically, the pressure decline transience during the shut-in phase of a minifrac test or a DFIT test is analyzed to identify when the fracture closes and to determine the pressure at that time. This pressure is called fracture closure pressure (P_c), also known as fracture closure stress, which is the minimum pressure required to keep a hydraulic fracture open or prevent it from closing. It is commonly assumed that fracture closure pressure is equal to the minimum principal stress, based on the linear relationship between fracture width and pressure (Gulrajani & Nolte, 2000). Accurately estimating fracture closure pressure is essential for determining the net pressure which is the difference between the minimum principal stress and the pressure inside the hydraulic fracture. The net pressure is significant in optimizing hydraulic fracturing treatments, as well as predicting the production potential of a reservoir. The modern methods for determining fracture closure pressure were pioneered by Nolte (1979, 1986) who proposed an analytical approach based on material balance to interpret fracture parameters such as fracture length, fracture width, fluid loss coefficient, and fracture closure time. By assuming a constant fracture compliance and using Carter's leakoff model (Howard & Fast, 1957), the pressure decline can be characterized by using a specific function of time called the *G*-function or *G*-time.

$$P_0 - P(\Delta t_D) = \frac{\pi r_p C_L \sqrt{t_p}}{2c_f} \cdot G(\Delta t_D) \tag{7.1}$$

$$\Delta t_D = \frac{t - t_p}{t_p} \tag{7.2}$$

Where t_p is the pumping time, Δt_D is defined as the ratio of the elapsed time after shut-in $(t - t_p)$ to the pumping time since the start of injection (t_p), $P(\Delta t_D)$ is the wellbore pressure at Δt_D, P_0 is the wellbore pressure at the beginning of shut-in when $\Delta t_D = 0$, r_p is the ratio of the fracture surface area available for fluid loss to the gross fracture area, C_L is fluid loss coefficient, c_f is fracture compliance. Nolte (1979) introduced he $G(\Delta t_D)$ function as a representation of the elapsed time after shut-in normalized with respect to the duration of fluid injection/pumping:

$$G(\Delta t_D) = \frac{4}{\pi}\left(g(\Delta t_D) - g_0\right) \tag{7.3}$$

$$g(\Delta t_D) = \frac{4}{3}\left((1 + \Delta t_D)^{1.5} - \Delta t_D{}^{1.5}\right) \tag{7.4}$$

According to Castillo (1987), under ideal conditions (which include Carter's leakoff, constant fracture area, and constant fracture compliance/stiffness), a Cartesian plot of pressure decline against *G*-time (as defined in Eq. (7.1) would exhibit a linear relationship with a constant slope ($P^* = \frac{\pi r_p C_L \sqrt{t_p}}{2c_f}$) until fracture closure. Accordingly, the departure from linearity on the *G*-function plot would indicate fracture closure. To further enhance the interpretation of fracture closure, Castillo (1987) introduced the use of the derivative of pressure with respect to *G*-time (d*P*/d*G*) to magnify the slope change on the *G*-function plot. Subsequently, the product of *G*-time and the pressure derivative with respect to *G*-time (*G*d*P*/d*G*) was also used to detect fracture closure through the *G*-function plots (Barree & Mukherjee, 1996).

Analyzing pressure transients during a DFIT test based on the *G*-function and its derivatives has become a conventional technique for determining fracture closure pressure. However, in field practices, especially in low permeability formations, plots of pressure derivatives vs. *G*-time often display multiple slope deviations or changes, which are often referred to as non-ideal leakoff or non-ideal fracture closure. These non-ideal leakoff behaviors make fracture closure identification challenging. Therefore, many efforts have been pursued to explain and interpret fracture closure from *G*-function plots with non-ideal leakoff features. Most of these efforts are based on numerical simulations. Several factors have been suggested as possible causes of non-ideal leakoff, including "pressure-dependent leakoff", "fracture height recession", "fracture tip extension", and "opening of natural fissures" (e.g., Nolte, 1991; Barree & Mukherjee, 1996; Barree, 1998; Craig et al., 2000; and more). Barree et al. (2009) attempted to establish a "holistic diagnostic technique" for both normal and non-ideal leakoff situations by using *G*-function plot, $sqrt(\Delta t)$ plot, and log (ΔP) vs. log (Δt) plot. They suggested that the point at which the data starts to show slope deviation from a linear line from the origin tangent to the *G*d*P*/d*G* curve should be used as an indicator of fracture closure. This approach has been called the "tangent" method in McClure et al. (2016), where the deviation from a linear trend close to the peak value on the *G*d*P*/d*G* curve is selected as the signature for fracture closure determination.

Although Nolte's analytical approach (1979, 1986) assumes that fracture compliance/stiffness prior to fracture closure remains constant, he acknowledged that pressure decline behavior during shut-in varies depending on the relative relationship between the fracture's variables and those of the reservoir (Nolte, 1982). Martins & Harper (1985) later demonstrated that the rate of pressure decline during shut-in is related to fracture stiffness and the rate of fluid loss to the formation by using the chain rule. The equation for the rate of pressure decline is given by (Martins & Harper, 1985):

$$\frac{dP}{dt} = \frac{dP}{dV} \cdot \frac{dV}{dt} = -S_f \cdot q_L(t) \tag{7.5}$$

where $\frac{dP}{dt}$ is the rate of pressure decline, $\frac{dP}{dV}$ or S_f is fracture stiffness, $\frac{dV}{dt}$ or $q_L(t)$ represents the rate of fluid loss/leak-off. It is important to note that fracture stiffness is equal to the reciprocal of the product of fracture compliance (c_f) and fracture surface area (A_f), as expressed by the equation $S_f = 1/(A_f \cdot c_f)$.

The stiffness of an open fracture depends on its shape, dimensions, and the deformation properties of the formation. Accordingly, fracture stiffness, which is inversely related to fracture compliance, remains unchanged prior to fracture closure during shut-in, assuming that the fracture length and height remain constant before closure (Nolte, 1979; Martins & Harper, 1985). However, upon fracture closure, its stiffness changes due to the change in fracture length. In addition, contact between the two fracture surfaces leads to added stiffness. Hayashi & Haimson (1991) suggested fracture closure to be a three-stage process through analytical analysis. Initially, the fracture starts closing in a "hinge-like" mode, where the fracture width decreases while the fracture length remains constant, indicating no contact between the fracture surfaces.

Subsequently, closure progresses from the fracture tip towards the wellbore in a "zipper-like" manner. Finally, the fracture achieves complete hydraulic closure, with fluid leaks predominantly occurring through the wellbore wall. Raaen et al. (2001) proposed the "*stiffness*" method to determine closure recognizing that fracture stiffness should change instantly once fracture closure begins at the fracture tip. They proposed a theoretical model to characterize the stiffness change at fracture tip closure and suggested the identification of fracture closure through the observation of the first slope change on a $sqrt(\Delta t)$ plot. McClure et al. (2014) conducted numerical simulations to investigate the change of fracture compliance (equivalently, fracture stiffness) during fracture closure and its effect on pressure decline. Their results indicate that the non-ideal leakoff attributed to "fracture height recession" previously discussed by Barree et al. (2009), may be tied to the change in fracture stiffness (or compliance) caused by fracture closure. Subsequently, following the framework established by Martins & Harper (1985) and Raaen et al. (2001), McClure et al. (2016, 2019) stated that fracture contact occurs when $\mathrm{d}P/\mathrm{d}G$ begins to increase from its minimum value on a $\mathrm{d}P/\mathrm{d}G$ *vs.* G plot, which can then be used to determine fracture closure. This approach with various numerical adjustments has been referred to as the "*compliance*" method (McClure et al., 2016, 2019).

Both the "tangent" method and the "compliance" method are widely used in minifrac or DFIT analysis. However, the interpretations of fracture closure pressure from these two methods often disagree with each other (e.g., Craig et al., 2017; Ehlig-Economides & Liu, 2018; McClure et al., 2019), resulting in large uncertainties in stress estimates. The issue is not trivial, as the outcome controls the net pressure estimate, the difference between the fracturing fluid pressure and the closure pressure, which represents the energy required for propagating fractures and controls fracture growth and geometry. In many field DFIT tests, the "tangent" method tends to underestimate fracture closure pressure (e.g., McClure et al., 2019; Dutler et al., 2020; Bröker & Ma, 2021). In many other cases, the "compliance" method lacks a clear signature, making fracture closure determination ambiguous (e.g., Bröker & Ma, 2021; Virues et al., 2022; McClure et al., 2022). This has led to significant controversy regarding the validity of these two approaches.

The methods for determining fracture closure pressure (P_c), specifically the "tangent" method and the "compliance" method, have seldom been evaluated via controlled physical experiments. Furthermore, there has been a lack of systematic investigation comparing various pressure indicators, such as fracture reopening pressure (P_r), instantaneous shut-in pressure (*ISIP*), and fracture closure pressure (P_c), for stress determination under controlled experimental conditions across different rock types and injection scenarios. To bridge this research gap, we performed a series of controlled laboratory DFIT/minifrac experiments under true-triaxial stress and room temperature conditions. During these experiments, we concurrently monitored and analyzed wellbore pressure and acoustic emissions throughout the injection and shut-in phases of each test cycle, aiming to determine the minimum principal stress (S_3). The findings shed light on: (1) the effectiveness of various HF-based methods in determining S_3; and (2) illustrate the complex physical processes governing fracture closure and their influence on pressure transient behavior during shut-in. Building on these insights, we propose a new approach for determining fracture closure pressure.

7.1 Sample Collection and Experimental Techniques

7.1.1 Sample Preparation

Rock properties such as permeability and mechanical properties can significantly impact the diffusion or leak-off of fluid from a hydraulic fracture, as well as the dynamics of fracture reopening and closure. Furthermore, the elastic moduli of the rock, along with the stiffness and strength of fracture asperities, play a vital role in the evolution of fracture aperture during fluid injection and shut-in, which in turn affects fluid diffusion. As the fracture closure during shut-in depends on the rate of fluid diffusion, the closure process and the signatures used to identify closure are also influenced by rock properties. Therefore, we conducted laboratory scale minifrac experiments on three rock types: Sierra White Granite, Crab Orchard Sandstone, and Scioto Sandstone (Figure 7.1).

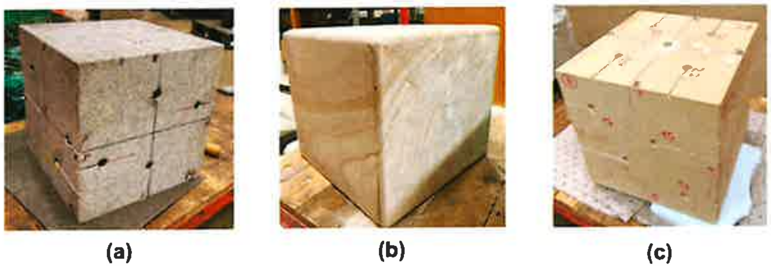
(a) (b) (c)

Figure 7.1. Various rock types with distinct rock properties used in the laboratory hydraulic fracturing stress measurements. (a) Sierra White Granite; (b) Crab Orchard Sandstone; (c) Scioto Sandstone. Among the four experiments in this study, E1 and E2 were conducted on Sierra White Granite, E3 was performed on Crab Orchard Sandstone, and E4 was conducted on Scioto Sandstone.

The relevant geomechanical properties of these rocks were determined by laboratory tests (Table 7.1).

Table 7.1. Relevant geomechanics properties of the rock samples.

Rock Types	**Bulk Density, g/cc**	**Permeability, micro-Darcy**	**Porosity, %**	**Uniaxial Compressive Strength, MPa**	**Young's Modulus, GPa**	**Poisson's Ratio**
Sierra White Granite	2.62	0.5-1	0.6-1	150	68	0.32
Crab Orchard Sandstone	2.52	2-30	1-5	114	35	0.29
Scioto Sandstone	2.24	100-400	16-18	67	24	0.25

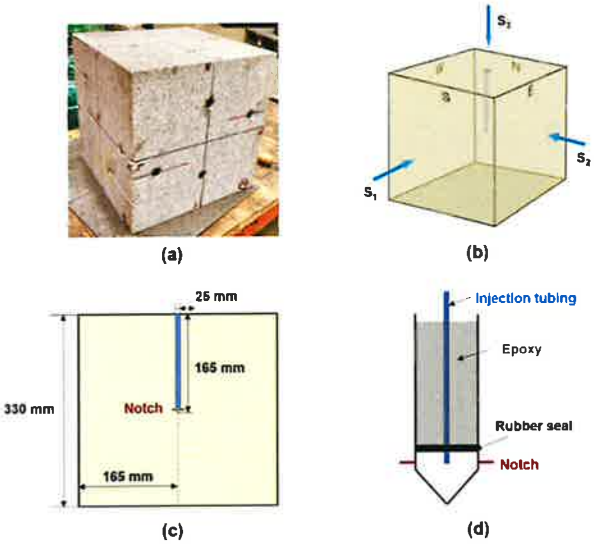

(a) (b) (c) (d)

Figure 7.2. Sample Preparation Process: (a) A cubic rock sample of Sierra White Granite, measuring 330×330×330 mm in size; (b) the cubic rock sample subjected to controlled true-triaxial stress conditions; (c) layout depicting the placement of an injection wellbore within the cubic rock sample; (d) an in-depth view of the assembly components of the injection wellbore.

As depicted in Figure 7.2(a), the samples were prepared as cubic blocks, each with dimensions of 330×330×330 mm (approximately 13×13×13 inches). In the experiments, each cubic rock sample is subjected to true-triaxial stress compression along three orthogonal axes, as shown in Figure 7.2(b). An injection wellbore, 25 mm (about 1 inch) in diameter, was drilled into the center of each block from one of its side surfaces, as illustrated in Figure 7.2(c). This wellbore reached a depth of about 165 mm (roughly 6.5 inches). An open section approximately 0.5 inch was left at the bottom of the wellbore. A circular notch was also made in this section to facilitate fracture initiation perpendicular to the minimum principal stress and to reduce near wellbore tortuosity.

7.1.2 Experimental Setup

The experiments were conducted under controlled true-triaxial stress conditions using a novel, in-house high-temperature, high -pressure true-triaxial testing system, as illustrated in Figure 7.3. This system enables advanced geomechanical experiments that mimic subsurface reservoir conditions in a laboratory setting. It is designed to apply stress independently to a cubic rock sample along three orthogonal directions, as depicted in Figure 7.2(b), by pressurizing flat jacks acting on the sidewalls of the cubic sample. The system can accommodate various sample sizes, up to 432×432×432 mm (approximately 17×17×17 inches), and has been utilized in various experiments to address subsurface engineering problems, such as hydraulic fracturing, in-situ stress, heat extraction, and HF-NF interactions (Hu & Ghassemi, 2020a; 2020b; Ye & Ghassemi, 2023a; 2023b).

Three Teledyne ISCO 100DM syringe pumps were utilized to independently apply the three principal stresses, achieved by pumping mineral oil into flat jacks. Additionally, a Teledyne ISCO 260D syringe pump was employed to inject mineral oil or deionized water, facilitating the creation of a hydraulic fracture and the execution of injection/fall-off tests during each mini-frac experiment. The fluid flow parameters (pressure, flow rate, and pump volume) for each syringe pump were concurrently recorded using LabVIEW-based software. The ISCO D-series pumps are characterized by their high precision in fluid control, exhibiting a pressure error of ±0.5% and a flow rate error of ±0.3%.

Acoustic Emission (AE) technology was employed to monitor fracture initiation and propagation during the fracturing cycle, as well as to assist in identifying fracture reopening and closure during the subsequent injection/fall-off cycles. A total of 20-24 in-house AE sensors, made with compressional wave piezoelectric transducers (PZT-5A, Boston Piezo-Optics, Inc.), were utilized. These sensors, with a 12.5 mm diameter and 500 kHz resonant frequency, were strategically embedded into shallow pockets drilled in the rock to detect AE signals. The AE system used in this study is the Express-8 AE system, supplied by Physical Acoustics Corporation, featuring 24 high-speed channels, each with a 16-bit A/D converter. The Express-8 AE System is integrated with AEwin™ software, facilitating real-time waveform and AE features processing, display, and analysis. During the tests, the radiated wave signals captured by the AE sensors were amplified by 40 dB using PAC 2/4/6 preamplifiers (Physical Acoustics Corporation) and filtered through an analog filter operating between 20 kHz and 400 kHz. The AE signals were recorded if they surpassed a threshold level of 45 dB, using a 10 MSPS sampling rate. For more details about this AE system and its application in laboratory injection experiments, please refer to our previous work (Ye & Ghassemi, 2020; 2023a).

Figure 7.3. In-house high-temperature true-triaxial testing system that replicates subsurface reservoir. This system is designed to independently apply stress to a cubic rock sample along three orthogonal axes and can accommodate samples up to 432×432×432 mm (approximately 17×17×17 inches). It is capable of being employed in various experiments to investigate subsurface engineering challenges, including hydraulic fracturing, in-situ stress measurements, heat extraction, and induced seismicity.

7.1.3 Experimental Procedure for DFIT Experiments Conducted at Room Temperature

The injection scheme involved a hydraulic fracture initiation cycle, a few fracture propagation cycles, and multiple injection/fall-off (or injection/shut-in) cycles. In the fracture initiation and propagation cycles, a nearly planar fracture was initiated and propagated within the cubic rock sample, oriented perpendicular to the applied minimum principal stress (S_3). The wellbore pressure monitored during the subsequent injection/fall-off cycles was analyzed using various methods. This was to determine the fracture reopening pressure (P_r), instantaneous shut-in pressure (*ISIP*), and fracture closure pressure (P_c). These pressure indicators were then compared with the applied minimum principal stress (S_3) to provide insights into hydraulic fracturing (HF)-based stress measurements.

7.2 Interpretation of Injection/Fall-off Cycles from Room-Temperature DFIT Experiments

We present the results of four room temperature DFIT experiments: two on Sierra White granite, one on Crab Orchard Sandstone, and another on Scioto Sandstone. The specific test conditions, including stress states and injection parameters, are detailed in Table 7.2. These rock types, characterized by varying properties such as permeability and elastic moduli, were anticipated to exhibit distinct leak-off behaviors and varied fracture reopening and closure patterns. Furthermore, by employing injection fluids with varying viscosities, both rapid and slow leak-off rates were facilitated across these rocks, each possessing different levels of permeability.

In Experiment 1 (E1) on Sierra White Granite, mineral oil was used as the injectate, so that an extremely slow leak-off was observed during the shut-in phase, with an average pressure decline rate of less than ~1 kPa/s. In Experiment 2 (E2), and also on Sierra White Granite, water was used as the injectate. The leak-off rate during shut-in was somewhat faster than Experiment 1 (E1) but still slow, showing an average pressure decline rate of approximately ~3 kPa/s. Experiment 3 (E3) was conducted on Crab Orchard Sandstone using mineral oil. It demonstrated a medium leak-off rate during shut-in, with an average decline rate of ~10 kPa/s. In contrast, Experiment 4 (E4) on Scioto Sandstone using water displayed an extremely fast leak-off during shut-in, with the pressure decline rate exceeding ~700 kPa/s. The diverse leak-off behaviors observed in these experiments provide an opportunity to systematically examine the physics of fracture closure during hydraulic fracturing stress tests. This variety also allows for a comprehensive evaluation of current stress interpretation methods.

Table 7.2. Specific test conditions for the four laboratory minifrac experiments.

Experiment #	Rock Types	Stress States			Injection Fluid	Injection Rate, ml/min	Leak-off Rate
		Maximum Principal Stress, MPa (psi)	Intermediate Principal Stress, MPa (psi)	Minimum Principal Stress, MPa (psi)			
E1	Sierra White Granite	20.68 (3000)	13.79 (2000)	8.62 (1250)	Mineral Oil	0.5	Extremely Slow
E2	Sierra White Granite	20.68 (3000)	13.79 (2000)	8.62 (1250)	Deionized Water	0.5	Slow
E3	Crab Orchard Sandstone	17.24 (2500)	17.24 (2500)	10.34 (1500)	Mineral Oil	0.6	Medium
E4	Scioto Sandstone	20.68 (3000)	13.79 (2000)	8.62 (1250)	Deionized Water	30-40	Extremely Fast

In the hydraulic fracturing phase of each experiment, our objective was to create a nearly planar fracture perpendicular to the applied minimum horizontal stress (S_3) for accurately representing the stress acting on the fracture. Utilizing a controlled injection strategy, we achieved this goal across all four minifrac experiments. In Experiments 1 and 2, performed on Sierra White Granite, relatively large hydraulic fractures were formed. The fracture areas were approximately 60-80 times larger than the area of the injection wellbore in each case. Conversely, in Experiments 3 and 4, which involved the more permeable Crab Orchard Sandstone and Scioto Sandstone, the hydraulic fractures were smaller, about 30-40 times larger than the wellbore area. Notably, in Experiment 4 on Scioto Sandstone using water injection, a high injection rate of 30-40 ml/min was required to initiate and propagate a hydraulic fracture. However, the resulting fracture had a relatively small area, approximately 30 times larger than the area of the injection wellbore. The primary focus of this study is the investigation of fracture closure processes for stress determination during minifrac or DFIT tests. Using Experiment 1 on the low permeability Sierra White Granite and Experiment 4 on the highly permeable Scioto Sandstone as examples, we briefly describe the hydraulic fracturing process, and the characteristics of the fractures created in each experiment.

In Experiment 1 using Sierra White Granite, the injection of mineral oil at a flow rate of 0.5 ml/min led to the formation of a nearly planar fracture. This outcome was achieved through an initial fracture initiation cycle (Cycle 1) followed by two fracture propagation cycles (Cycles 2 and 3). By adhering to the pressure drop restriction criteria outlined in Section 2.3.1, we effectively prevented runaway fracture propagation, thereby ensuring the development of a contained, nearly planar fracture. The planarity of the fracture was substantiated by the growth pattern of the Acoustic Emission (AE) cloud, as illustrated in Figures 7.4(a) and 7.4(b). Following the completion of Experiment 1, a mixture of deionized water and fluorescent particles was injected into the granite block via the injection wellbore to mark the hydraulic fracture. The block was subsequently trimmed with a diamond saw and split along the fracture plane, allowing for a direct examination of the fracture as depicted in Figure 7.4(c). It should be noted, however, that the actual fracture, exhibiting a near-penny shape as indicated by the AE cloud, is distinct from the rectangular shape of the split fracture, implying that the true fracture area is relatively smaller than that displayed in Figure 7.4(c). The split fracture underwent post-experiment surface scanning and processing, shown in Figure 7.4(d), to characterize the topography of the hydraulic fracture. The fracture area presented in Figure 7.4(d), marked by fluorescent particles, closely corresponds with the estimates derived from the AE cloud (Figure 7.4(a)), with the estimated area being approximately 400 cm^2, around 62 times larger than the wellbore area of 6.45 cm^2. As inferred from both the AE cloud and the surface topography, the fracture geometry is nearly planar and flat, particularly near the wellbore, although some irregularities in topography are observed further from it. Consequently, the normal stress acting on the fracture is expected to be very close to the applied minimum principal stress (S_3, as depicted in Figure 7.2(b)), which was set at 8.62 MPa (or 1250 psi). This reference stress is essential for the analysis of subsequent injection/fall-off tests and for the assessment of hydraulic fracturing (HF)-based stress determination methods.

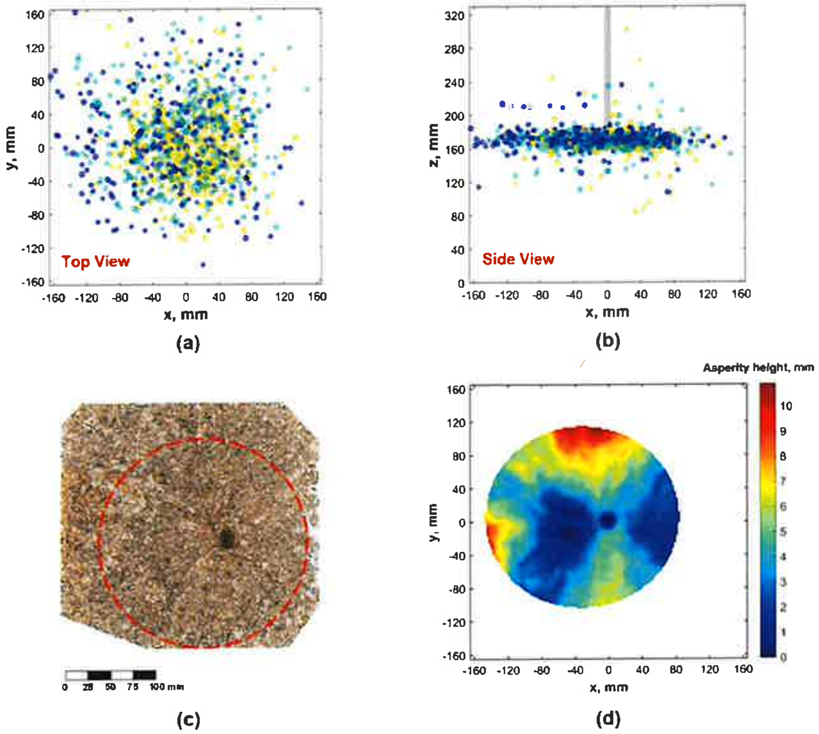

Figure 7.4. Outcomes of Hydraulic Fracturing in Experiment 1 on Sierra White Granite: (a) Top View and (b) Side View show the spatial distribution of Acoustic Emission (AE) events during the fracture initiation and propagation cycles, with yellow dots indicating AE events from the initiation cycle, and cyan and blue dots representing those from the first and second propagation cycles, respectively; (c) depicts the lower portion of the fracture, revealed after trimming and splitting the tested granite block; and (d) displays the topographical details of the hydraulic fracture obtained through surface scanning, providing insights into the planarity and spatial variations of the fracture.

In Experiment 4 on Scioto Sandstone, we utilized a high flow rate of 30-40 ml/min for deionized water injection, necessitated by the sandstone's high permeability, to initiate and propagate a hydraulic fracture. This process involved one fracture initiation cycle and two subsequent fracture propagation cycles, following the controlled fluid injection approach with a pressure drop threshold. However, the hydraulic fracture created in this experiment was relatively smaller compared to the fracture created in the low permeability granite of Experiment 1. Additionally, the Acoustic Emission (AE) activities observed during this phase, as shown in Figures 7.5(a) and 5(b), were notably weaker than those in Experiment 1, as seen in Figures 7.4(a) and 7.4(b). Post-experiment, the fracture was analyzed similarly to Experiment 1. The fracture area, marked by a fluorescent dye (Figure 7.5(c)) and confirmed by surface scanning (Figure 7.5(d)), was about 205 cm^2, approximately 30 times larger than the wellbore area. Despite the differences in AE activity and fracture propagation compared to the granite, the hydraulic fracture in the Scioto Sandstone maintained a nearly flat and penny-shaped geometry, as suggested by the marked fracture area in Figure 7.5(c) and the surface scanning contour in Figure 7.5(d). This observation implies that the normal stress acting on the fracture closely aligned with the applied minimum principal stress (8.62 MPa or 1250 psi), offering a reliable reference point for subsequent stress analysis in the injection/fall-off cycles.

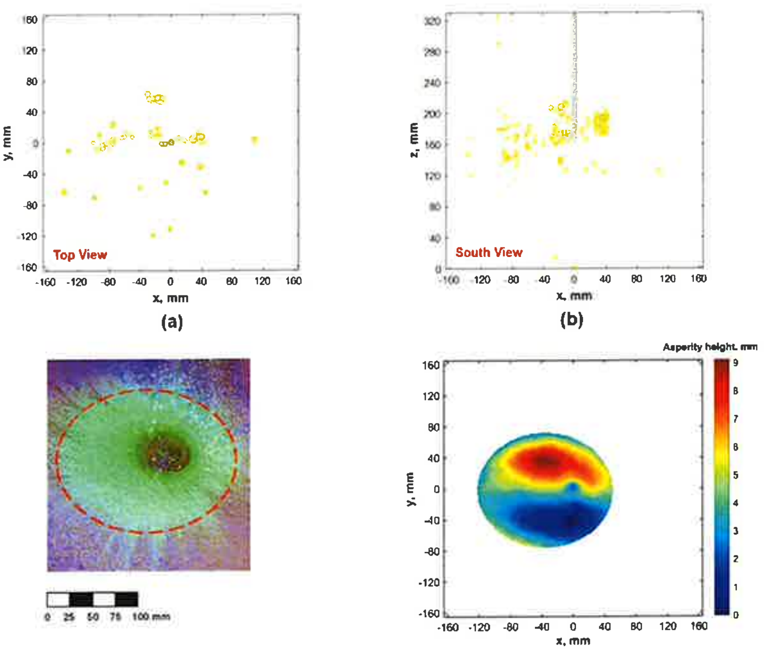

(a) (b)

(c) (d)

Figure 7.5. Outcomes of Hydraulic Fracturing in Experiment 4 on Scioto Sandstone: (a) Top View and (b) Side View show the spatial distribution of Acoustic Emission (AE) events, as represented by the yellow dots, during the fracture initiation cycle; (c) depicts the lower portion of the hydraulic fracture, revealed after trimming and splitting the tested sandstone block; and (d) displays the topographical details of the hydraulic fracture obtained through surface scanning, providing insights into the planarity and spatial variations of the fracture.

Given that the hydraulic fractures produced in each experiment exhibited a nearly planar geometry, particularly near the wellbore area, the normal stress acting on these fractures is anticipated to align closely with the applied minimum principal stress (S_3). As shown in Table 7.2, S_3 was set at 8.62 MPa (1250 psi) for Experiments 1 (E1), 2 (E2), and 4 (E4), while Experiment 3 (E3) was conducted with a higher applied S_3 of 10.34 MPa (1500 psi). These specified stress levels will serve as references for analyzing subsequent injection/fall-off tests, facilitating stress determination and the evaluation of various stress determination methods based on hydraulic fracturing measurements.

After the hydraulic fracturing phase, several injection/fall-off cycles were performed in each experiment to mimic DFIT or minifrac tests in a controlled laboratory setting. These tests aimed to evaluate different stress determination methods and investigate the physics of fracture reopening and closure during the injection and shut-in phases. Typically, one or more out of the three pressure indicators/characteristics—fracture reopening pressure (P_r), instantaneous shut-in pressure (*ISIP*), and fracture closure pressure (P_c)—are interpreted from the pressure transients in a hydraulic fracturing (HF)-based test to determine the minimum principal stress (S_3). However, there is no consensus on which indicator reliably reflects the magnitude of S_3 during in-situ stress determination. Often, inconsistencies and large uncertainties could exist, leading to challenges in determining S_3. In this section, we analyze the pressure transient data from injection/fall-off cycles of each room temperature DFIT experiment to compare and evaluate the three pressure indicators in estimating the minimum principal stress.

7.2.1 Fracture Reopening Pressure

Fracture reopening pressure (P_r) is the minimum fluid pressure necessary to reopen a previously created hydraulic fracture, providing insights into estimating the minimum principal stress (S_3). It is commonly understood that fracture reopening pressure corresponds to the moment when the fracture lip begins to open against the wellbore wall. In the injection phase of an injection/fall-off test, before the fracture reopens, the wellbore pressure usually rises in a linear fashion under a constant-rate injection process (Shlyapobersky, 1989). The reopening pressure (P_r) is identified at the point where the pressure-time curve of the wellbore distinctly deviates from this linear trend. This deviation indicates that the hydraulic fracture has reopened due to injection, permitting increased fluid flow within the fracture from the wellbore.

Figure 7.6 highlights the determination of fracture reopening pressure (P_r) obtained from the four experiments (E1 to E4), showcasing how this pressure varies with different rock types and injection fluids, using the deviation from linearity on the pressure-time curve as an indicator. In Experiment 1 (E1) with Sierra White Granite, characterized by extremely low permeability (0.5-1 micro-Darcy) and using mineral oil as the injection fluid, the fracture reopening pressure (P_r) was determined at approximately 8.73 MPa (1266 psi). This value is slightly higher than the applied minimum principal stress (S_3) of 8.62 MPa (1250 psi). Similarly, Experiment 3 (E3) conducted on Crab Orchard Sandstone (with a permeability range of 2-30 micro-Darcy, which is low but higher than Sierra White Granite) using mineral oil for injection, identified a reopening pressure of 10.49 MPa (1521 psi), which aligns closely with the applied S_3 of 10.34 MPa (1500 psi). On the other hand, Experiments 2 (E2) and 4 (E4), which involved injections of deionized water into Sierra White Granite (extremely low permeability, 0.5-1 micro-Darcy) and Scioto Sandstone (highly permeable, 100-400 micro-Darcy), both exhibited reopening pressure (5.26 MPa and 5.42 MPa, respectively) significantly lower than the applied S_3 of 8.62 MPa (1250 psi).

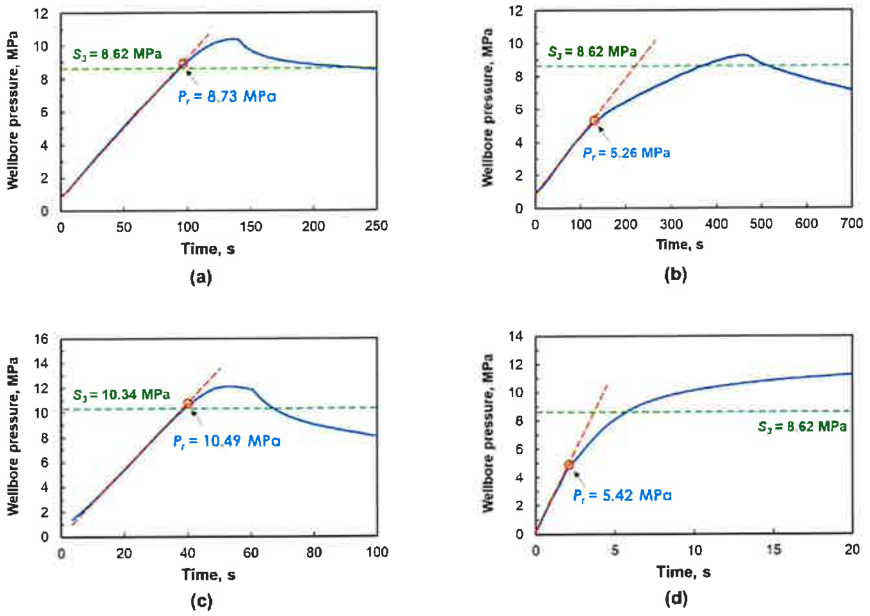

Figure 7.6. Determination of the fracture reopening pressure for: (a) Experiment 1 (E1) on Sierra White Granite with mineral oil as the injection fluid; (b) Experiment 2 (E2), also on Sierra White Granite, but with water injection; (c) Experiment 3 (E3) on Crab Orchard Sandstone using oil as the injection fluid; and (d) Experiment 4 (E4) on Scioto Sandstone, utilizing water for injection. The green dashed line represents the applied minimum principal stress, serving as the reference stress level for the analysis.

Fracture reopening in subsequent injection cycles is governed by several critical factors including the injection flow rate, the characteristics of the injection fluid, the pore pressure within the formation, and the minimum principal stress (Shlyapobersky, 1989; Ratigan, 1992; Ito & Hayashi, 1993). Our observations show a clear variation in reopening pressures, particularly when comparing the effects of mineral oil and deionized water used as injection fluids. This variation highlights the significant role of fluid viscosity in the process of hydraulic fracture reopening. In Experiments 2 and 4, low viscosity deionized water was used as the injection fluid. This facilitated its penetration into the fractures before their mechanical reopening, which resulted in a lower estimation of reopening pressure. On the other hand, in Experiments 1 and 3 where high viscosity mineral oil was used which hindered its entry into the fractures until there was a significant increase in fracture aperture due to its mechanical reopening. These results support the idea that even mechanically closed fractures maintain some hydraulic conductivity, possibly through a residual fracture aperture (van Dam et al., 2000; Fredd et al., 2000). In the case of Experiments 2 and 4, this residual aperture was enough for the infiltration of the low-viscosity water prior to the reopening of the fracture. This highlights the complex relationship between fluid type, fracture aperture (or mechanical deformation), and fracture conductivity during the reopening of a hydraulic fracture by fluid injection.

7.2.2 Instantaneous Shut-in Pressure (ISIP)

Instantaneous shut-in pressure (*ISIP*), or simply shut-in pressure, refers to the pressure in the wellbore at the moment when the hydraulic fracturing pump is abruptly stopped and the fracture begins to close. *ISIP* is frequently utilized in field-scale hydraulic fracturing stress measurements to estimate the minimum principal stress, S_3, although its accuracy and reliability remain topics of discussion in the literature (Hickman & Zoback, 1981; Gronseth & Kry 1981). For determining *ISIP*, various methodologies using the pressure transient data during shut-in phase of hydraulic fracturing tests have been proposed (Doe & Hustrulid, 1981; McClennan & Roegiers 1981; Zoback & Haimson, 1982). In our study, we adopted the method of plotting wellbore pressure P_w against $\log((t+\Delta t)/\Delta t)$ for *ISIP* determination, as introduced by McClennan & Roegiers (1981) and depicted in Figure 7.7. The deviation from a linear relationship in the P_w versus $\log((t+\Delta t)/\Delta t)$ plot serves as the basis for *ISIP* determination. Our findings, derived from four experiments using different rock types and injection fluids, reveal that *ISIP* consistently provides a reliable estimate of the minimum principal stress (S_3), though it tends to slightly overestimate its magnitude.

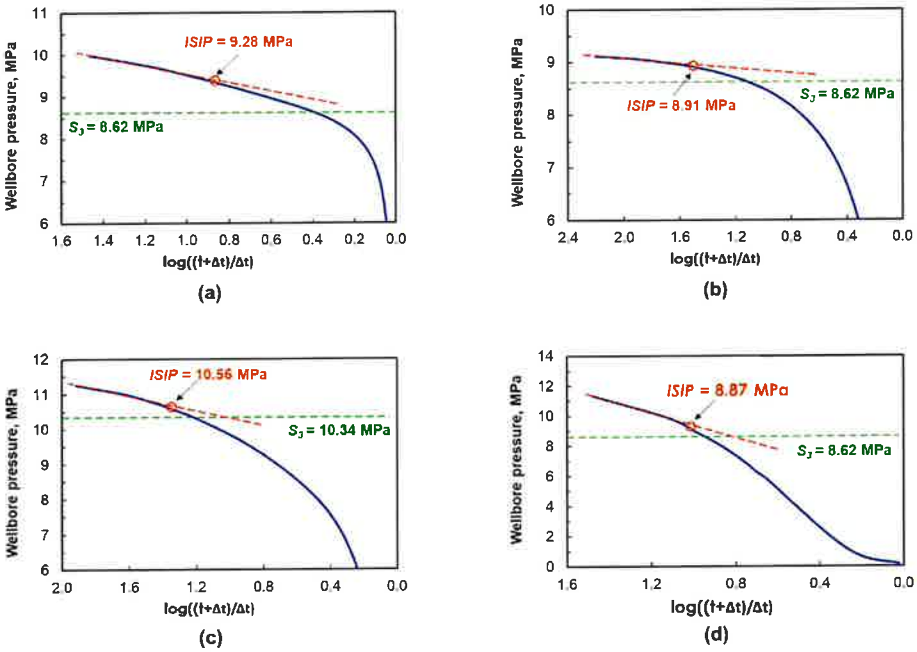

Figure 7.7. Determination of the instantaneous shut-in pressure (*ISIP*) for: (a) Experiment 1 (E1) on Sierra White Granite with mineral oil as the injection fluid; (b) Experiment 2 (E2), also on Sierra White Granite, but with water injection; (c) Experiment 3 (E3) on Crab Orchard Sandstone using oil as the injection fluid; and (d) Experiment 4 (E4) on Scioto Sandstone, utilizing water for injection. The green dashed line represents the applied minimum principal stress, serving as the reference stress level for the analysis.

During hydraulic fracturing-based stress measurements, *ISIP* is often observed to be higher than the minimum principal stress, a phenomenon likely linked to viscous pressure losses and fracture toughness within the hydraulic fracture upon shut-in (Hickman & Zoback ,1981; Shlyapobersky, 1989). Moreover, field-scale studies have noted a gradual convergence of *ISIP* towards the minimum principal stress (S_3) after several repeated injection/fall-off cycles (Hickman & Zoback,1981; Gronseth & Kry 1981). Our laboratory experiments also mirror this trend, showing a tendency for *ISIP* to significantly overestimate S_3 based on pressure data from the hydraulic fracturing phase (fracture initiation and propagation cycles), especially in Experiment 1 conducted on Sierra White Granite with highly viscous mineral oil as the injection fluid. However, after a few injection/fall-off cycles, *ISIP* appears to stabilize and move close to S_3. Our results affirm that *ISIP* can serve as a dependable indicator for determining S_3, provided that an appropriate injection rate and a sufficient number of injection/fall-off cycles are applied during the hydraulic fracturing-based stress measurement process. Furthermore, *ISIP* could often act as the upper boundary for the minimum principal stress (S_3), ensuring the analysis is consistent and reasonable.

7.2.3 Fracture Closure Pressure

The data from our experimental campaign enables us to assess the two commonly used DFIT analysis methods (the "tangent" method and the "compliance" method) and advance insights into the physics governing fracture closure. The leakoff from the fracture to the surrounding rock matrix in experiments E1, E2, and E3 was quite slow during the shut-in phase, resulting in very dense pressure transient data. To manage this, we adjusted the sampling rate to reduce the data density. Additionally, to better interpret the *G*-function plots for E1, E2, and E3, we applied a central moving average algorithm to smooth the data when determining the values of GdP/dG and dP/dG. It is important to note that this smoothing process does not affect the linearity or the determination of slope deviations when utilizing *G*-function plots for fracture closure analysis. In contrast, for experiment E4, where leakoff was rapid, no changes to the data density or smoothing algorithm were needed.

Figure 7.8 illustrates the interpretation of fracture closure through the "tangent" method for the four laboratory DFIT experiments. It can be seen that non-ideal leakoff behavior is clearly demonstrated in E1 and E3, while it can also be detected in E2, although it is not as conspicuous. On the other hand, E4 presents normal leakoff behavior with a perfectly linear trend until the deviation occurs which is used to suggest fracture closure. As previously discussed, the leakoff rate in E1, E2, and E3 is comparatively slow due to the low permeability of Sierra White Granite and Crab Orchard Sandstone, while E4 demonstrates high leakoff due to the extremely high permeability of Scioto Sandstone. The non-ideal leakoff behaviors observed in E1, E2, and E3 are similar to those observations that have been detected in the field-scale DFIT tests conducted in low permeability shale and granite reservoirs (Nolte, 1991; Barree & Mukherjee, 1996; Barree, 1998; Craig et al., 2000). According to the "tangent" method, the point on the GdP/dG curve, which deviates from a linear trend from the origin and is near the peak, should be used as the signature for determining fracture closure (Barree et al., 2009; McClure et al., 2016). As a result, the interpreted fracture closure pressure (P_c) in E1, E2, and E3, which all present with non-ideal leak-off behaviors, are far smaller than the applied minimum principal stress (S_3). This is consistent with observations from many field DFIT tests conducted in low-permeability shale reservoirs, where the "tangent method" tends to underestimate the minimum principal stress (e.g., McClure et al., 2016; McClure et al., 2019; Dutler et al., 2020; Bröker & Ma, 2021). On the other hand, for E4 with normal leakoff behavior conducted in highly permeable sandstone, the "tangent" method yields a reliable fracture closure pressure of 8.82 MPa, which is close to the applied minimum principal stress of 8.62 MPa.

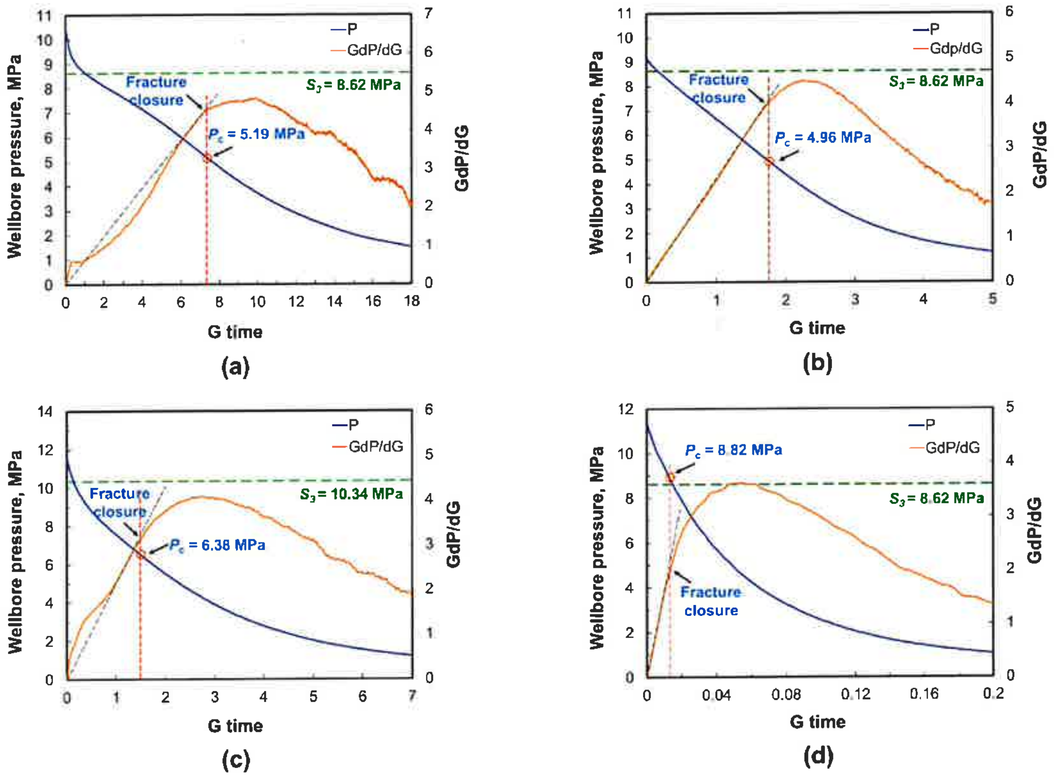

Figure 7.8. Determination of the fracture closure pressure through the "tangent" method for: (a) Experiment 1 (E1) on Sierra White Granite with mineral oil as the injection fluid; (b) Experiment 2 (E2), also on Sierra White Granite, but with water injection; (c) Experiment 3 (E3) on Crab Orchard Sandstone using oil as the injection fluid; and (d) Experiment 4 (E4) on Scioto Sandstone, utilizing water for injection. E1, E2, and E3 present non-ideal leak-off features with multiple slope deviations, while E4 shows normal leak-off behavior. The green dashed line represents the applied minimum principal stress, serving as the reference stress level for the analysis.

Fracture closure was also interpreted through the "compliance" method for the four laboratory DFIT experiments. In the "compliance" method, the increase of dP/dG from its minimum value on a G-function plot is viewed as a signature for determining fracture closure, and then two empirical "rules-of-thumb" were suggested for stress estimation (McClure et al., 2019). As shown in Figure 7.9, E1 and E2, conducted on Sierra White granite, exhibit a clear compliance signature where the minimum value of dP/dG can be identified. According to the first "rule-of-thumb," the contact pressure (or closure pressure) for E1 was determined at the point where there is approximately a 10% increase from the minimum dP/dG value. Subsequently, 0.52 MPa (or 75 psi) was subtracted from the contact pressure to estimate the minimum principal stress (S_3). This approach resulted in a closure pressure of 7.20 MPa and an estimated S_3 of 6.68 MPa for E1. For E2, where the increase from the minimum dP/dG value was less than 10%, the maximum dP/dG value following the minimum dP/dG value, corresponding to a 2% increase from its minimum, was selected to determine the closure pressure. This resulted in a closure pressure of 5.65 MPa and an estimated S_3 of 5.13 MPa after subtracting 0.52 MPa. Both estimated S_3 values for E1 and E2 were notably smaller than the applied minimum principal stress.

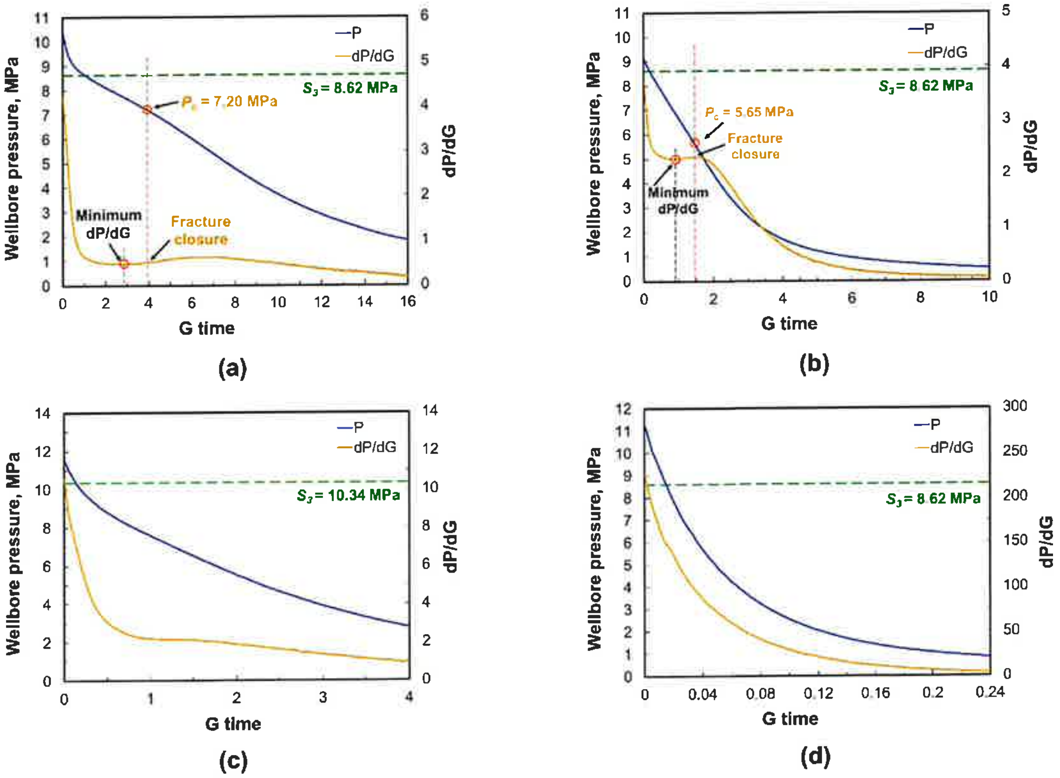

(a) (b) (c) (d)

Figure 7.9. Determination of the fracture closure pressure through the "compliance" method for: (a) Experiment 1 (E1) on Sierra White Granite with mineral oil as the injection fluid; (b) Experiment 2 (E2), also on Sierra White Granite, but with water injection; (c) Experiment 3 (E3) on Crab Orchard Sandstone using oil as the injection fluid; and (d) Experiment 4 (E4) on Scioto Sandstone, utilizing water for injection. E1, E2, and E3 present non-ideal leak-off features with multiple slope deviations, while E4 shows normal leak-off behavior. E1 and E2 have a clear signature, as the minimum value of d*P*/d*G* can be detected, while E3 and E4 lack a clear signature as they both present a monotonic declining trend on the d*P*/d*G* curve. The green dashed line represents the applied minimum principal stress, serving as the reference stress level for the analysis.

On the other hand, there is a lack of a clear signature for determining fracture closure via the "compliance" method in E3 (conducted on Crab Orchard Sandstone) and E4 (performed on Scioto Sandstone), because both E3 and E4 present a monotonic declining trend on the d*P*/d*G* curve. The "compliance" method often fails to provide reliable stress estimates in cases where a clear signature for fracture closure at the minimum value on the d*P*/d*G* vs. *G* plot is absent (e.g., Virues et al., 2022; McClure et al., 2022). This is observed in our experimental results, where no clear compliance signature was observed in E3 and E4. Some rules of thumb for handling such cases where no clear "compliance" signature has been suggested (McClure et al. 2022) where E3 could be categorized as an "adequate contact point" case, where stress estimates can still be made with "adequate" confidence if an inflection point exists on the d*P*/d*G* vs. *G* curve. However, the validity of this approach has not been established. Given these uncertainties, we treated E3 and E4 as cases where the compliance method cannot be reliably applied in this study.

7.3 Results of DFIT Experiments in Heated Blocks: Impact on ISIP, Closure and Reopening Pressures

In EGS reservoirs, the injection of cold fluids during stimulation or production can significantly cool both the rock matrix and the fracture network. This sudden temperature change triggers a phenomenon called thermoelastic stress, which is a mechanical response of the rocks and fractures to varying temperatures. Consequently, the cooling effect can result in the variation of fracture aperture and permeability in a fracture network (e.g., Ghassemi et al., 2007; Ghassemi & Zhou, 2011; Huang et al., 2019). However, the effect of rock cooling on fracture reopening and closure for stress determination has rarely been studied. Therefore, we also conducted several laboratory-scale DFIT experiments under high-temperature and high-stress conditions. During each experiment, we first injected pressurized fluid into a cuboid rock sample subjected to true-triaxial stress conditions to create and propagate a hydraulic fracture perpendicular to the applied minimum principal stress. Afterward, the fractured rock block was heated to ~100 °C, and then several cold injection/shut-in cycles using iced water as injection fluid were carried out to examine the cooling effect on fracture reopening and closure. Concurrently, pressure and temperature data within the wellbore were monitored during injection and shut-in phases of an injection-shut-in cycle to determine the minimum principal stress. We report the results of high-temperature DFIT experiments conducted on granite (low permeability) and sandstone (high permeability) cubic samples to examine: (1) the cooling effect on fracture reopening and closure pressure; and (2) the influence of injection rate on pressure evolution and fracture closure interpretation.

7.3.1 Rock Types & Experimental Techniques

The overall experimental procedure followed the same three-phase structure as the room temperature experiments, with additional steps for heating and thermal control. Following the room-temperature injection/fall-off (DFIT) cycles, experiments E2 (Sierra White Granite) and E4 (Scioto Sandstone)—both using deionized water as the injection fluid—were subjected to elevated temperature conditions using our custom-designed heating unit integrated with the true-triaxial loading frame. This system enabled uniform heating of large rock samples to approximately 100 °C within 1 to 3 days while maintaining stable true-triaxial boundary conditions. Once thermal equilibrium was achieved, iced water was injected into the hot and stressed blocks to reopen the previously generated hydraulic fractures, followed by shut-in periods to monitor fracture closure. During each injection/fall-off cycle, we continuously recorded wellbore pressure and temperature to assess the effects of thermal contraction on fracture mechanics and associated pressure responses.

For each cycle, we analyzed three key pressure indicators relevant to stress determination, including fracture reopening pressure (P_r), instantaneous shut-in pressure (*ISIP*), and fracture closure pressure (P_c), using the same analytical approaches employed in the room-temperature DFIT experiments. Additionally, the heat loss from cold fluid injection was estimated using the expression

$$Q_h = mc_p\Delta T \tag{7.6}$$

Where m is the mass of injected fluid, c_p is the specific heat capacity of water, and ΔT is the temperature difference between injected fluid and the rock.

We then evaluated the relationship between heat loss and pressure indicators. In general, we observed that P_r, *ISIP*, and P_c values obtained under high-temperature conditions were consistently lower than those measured during room-temperature DFIT cycles. This reduction is attributed to the thermoelastic contraction of the rock matrix and fracture surfaces due to the injection of cold fluid into a hot and stressed fracture. Our results also indicate that the extent of pressure reduction is influenced by both injection rate and rock types/properties. These findings underscore the importance of incorporating thermal effects into the interpretation of DFIT data, particularly for stress measurements in Enhanced Geothermal Systems (EGS).

7.3.2 Impact of Cooling on ISIP, Closure and Reopening Pressures from DFIT Experiments in Heated Sierra White Granite

After completing the room-temperature DFIT cycles in Experiment E2, the Sierra White Granite block was heated for high-temperature DFIT experiments involving cold fluid injection. This phase of testing was specifically designed to assess the impact of cooling effects on fracture reopening and closure in a low-permeability, high-strength crystalline rock, mimicking conditions in Enhanced Geothermal System (EGS) reservoirs.

Using the newly developed in-house heating unit integrated with our true-triaxial testing system (Figure 7.3), the cuboid Sierra White Granite sample was successfully heated to temperatures exceeding 100 °C. This custom-designed unit is capable of reaching block temperatures up to 400 °C, making it suitable for simulating geothermal reservoir conditions. In this study, the heating process lasted approximately three days, during which both the block surface temperature and the central wellbore temperature were continuously monitored. Temperature sensors embedded at the block surface and within the central wellbore confirmed a stable thermal gradient. Specifically, the block surface temperature was consistently around 3 °C higher than the wellbore temperature, indicating effective and uniform heat transfer from the outer heating elements to the core. As shown in Figure 7.10, the system reached a near steady-state thermal condition by the end of the heating period, with minimal temperature fluctuation over time. This heating procedure enabled simulation of high-temperature subsurface conditions typical of EGS reservoirs, and provided a thermally stable baseline for subsequent cold fluid injection and fracture response studies.

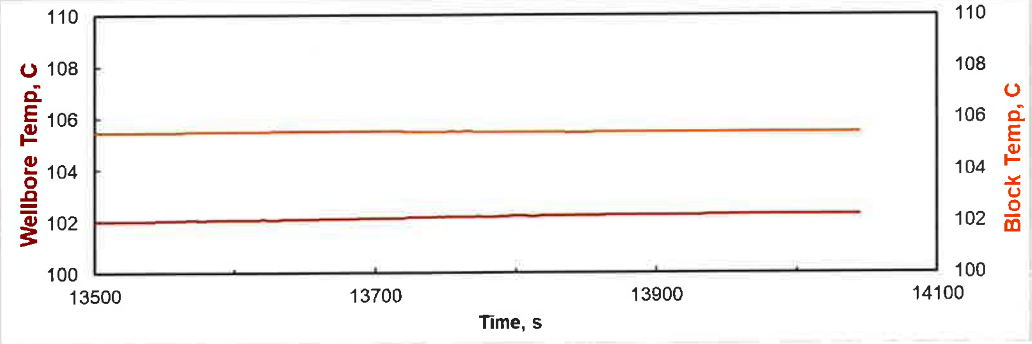

Figure 7.10. Temperature measurements at the block surface and within the wellbore, demonstrating the establishment of a near steady-state thermal condition during the heating phase. The surface temperature remained approximately 3 °C higher than the wellbore temperature, indicating effective and uniform heat distribution throughout the rock sample.

To enhance the cooling effect and evaluate its influence on pressure response, we first increased the minimum principal stress (S_3) to 1750 psi (12.07 MPa), which is 500 psi higher than the minimum horizontal stress applied in the room-temperature DFIT experiments (E2). Following this stress adjustment, we conducted a series of injection/fall-off cycles using iced water at elevated injection rates ranging from 5 to 15 mL/min. These rates were substantially higher than those used in the room-temperature DFITs (0.5–1 mL/min) and were intentionally selected to maximize the thermal contrast between the injected fluid and the hot rock mass. The goal of increasing the applied stress (S_3) and using higher injection rates was to amplify the cooling effect and clearly demonstrate its role in hydraulic stress measurements under EGS-relevant conditions.

Figure 7.11 illustrates the evolution of wellbore pressure, injection rate, and temperature during these high-temperature injection-shut-in cycles. Notably, as the number of cycles increased and the injection rate stepped up from 5 mL/min (Q1) to 15 mL/min (Q3), a consistent decline in peak injection pressure was observed. This decline trend, indicated by the dashed red arrow, indicates increasing thermal contraction around the fracture, leading to easier fracture reopening and more compliant fracture behavior. Simultaneously, the wellbore temperature (dark red) exhibited cyclic reductions corresponding to each cold injection, confirming a cooling-induced mechanical softening of the fracture. Table 7.3 provides quantitative data for each DFIT cycle, including peak pressure, fracture reopening pressure (P_r), *ISIP*, and closure pressure (P_c), along with cumulative heat loss. At lower injection rates (5 mL/min), the reduction in pressure indicators is moderate. However, as the injection rate increased to 10 and then 15 mL/min, a pronounced and nonlinear reduction in all pressure indicators was evident, particularly beyond Cycle 9. For instance, *ISIP* dropped from 1580 psi (Cycle 1) to 735 psi (Cycle 14), and closure pressure (tangent method) fell from 1640 psi to 735 psi—representing more than a 50% decrease.

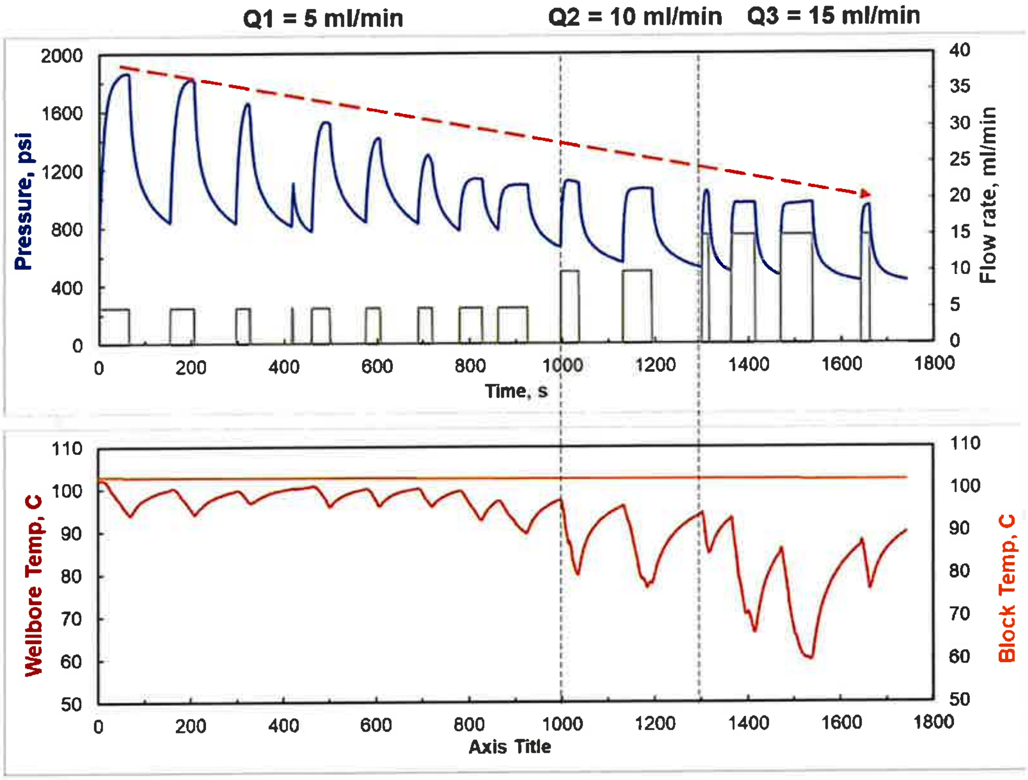

Figure 7.11. The evolution of wellbore pressure (blue), injection rate (gray), wellbore temperature (dark red), and block temperature (orange) during the injection-shut in tests in Phase 2 at high temperature conditions. The arrow indicates the decrease of peak injection pressure during cold fluid injection.

Table 7.3. The results of high temperature injection/falloff cycles of Sierra White Granite (E2).

Injection rate, ml/min	Cycle #	Peak Pressure, psi	Reopen Pressure, psi	ISIP, psi	Closure pressure, psi		Cumulative heat loss, J
					Tangent method	Compliance method	
5	1	1866	1291	1580	1640	/	175
	2	1821	1281	1548	1619	/	282
	3	1661	1237	1367	1400	/	311
	4	1531	1179	1348	1348	/	374
	5	1419	1136	1271	1271	/	414
	6	1300	1107	1121	1121	/	458
	7	1138	1009	1017	1039	/	571
	8	1096	979	989	1019	/	737
10	9	1122	1024	923	957	/	1195
	10	1067	927	913	948	/	2006
15	11	1051	958	789	789	/	2147
	12	969	896	728	758	/	3521
	13	971	884	737	766	/	5333
	14	950	854	735	735	/	5548

"/" indicates the lack of a signature for stress determination through the "compliance" method.

Figure 7.12 quantitatively captures the relationship between cumulative heat loss and the three key stress-related pressures. All four panels—(a) peak pressure, (b) fracture reopening pressure, (c) *ISIP*, and (d) fracture closure pressure—reveal clear inverse power-law relationships. The regression fits (with R^2 values of 0.83 to 0.92) indicate that a strong correlation between cumulative thermal energy loss and each pressure indicator/characteristics. The exponents in these power-law fits reflect the sensitivity of each indicator to cooling (heat loss).

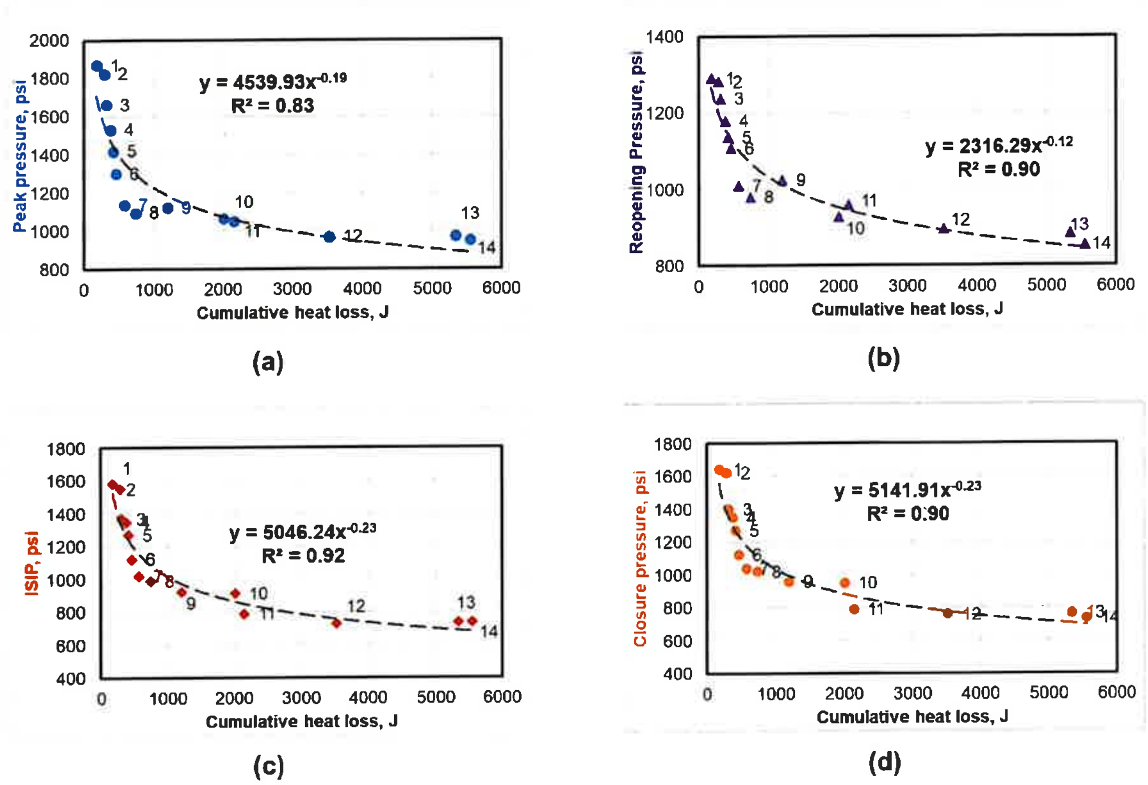

Figure 7.12. The relationship between pressure indicators and cumulative heat loss during high temperature DFIT tests of a cuboid Sierra White Granite. (a) peak injection pressure vs. cumulative heat loss; (b) fracture reopening pressure vs. cumulative heat loss; (c) *ISIP* vs. cumulative heat loss; (d) fracture closure pressure vs. cumulative heat loss.

7.3.3 Impact of Cooling on ISIP, Closure and Reopening Pressures from DFIT Experiments in Heated Scioto Sandstone

Following a similar procedure, we conducted high-temperature DFIT experiments on the high-permeability Scioto Sandstone used in Experiment E4. The sandstone block was heated to approximately 100 °C using the integrated heating system. Subsequently, iced water was injected at a high flow rate of 40 mL/min into the hot and stressed block to reopen the hydraulic fracture previously created during the room-temperature DFIT experiments (refer to Figure 7.5), followed by shut-in. Throughout each injection/fall-off cycle, wellbore temperature and pressure were continuously recorded to assess the impact of cooling on fracture reopening and closure behavior. Figure 7.13 presents the wellbore pressure and temperature data recorded during nine successive injection-shut-in cycles. The results clearly show a drop in wellbore temperature due to cold water injection, followed by gradual thermal recovery during the shut-in periods.

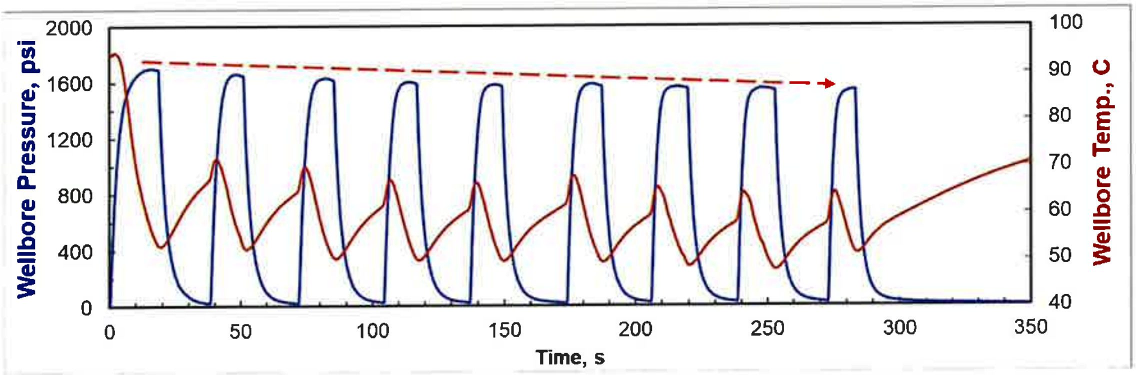

Figure 7.13. Wellbore pressure (blue) and temperature (dark red) measurements of the injection/falloff tests in Phase 2. The arrow shows the decrease of peak injection pressure during the multi-cycle cold injection.

For each cycle, we analyzed the fracture reopening pressure, *ISIP*, and fracture closure pressure using the same procedures applied in previous experiments. Additionally, we calculated the heat loss ($Q_h = mc_p\Delta T$) due to cold fluid injection and correlated it with key pressure characteristics used for stress determination. The results from nine cold fluid injection and shut-in cycles are summarized in Table 7.4. Consistent with observations from the granite tests, the peak pressure, fracture reopening pressure, *ISIP*, and closure pressure in the heated sandstone block progressively declined with successive cold fluid injections. This reduction is attributed to the cooling effect resulting from the injection of cold fluid into a hot, stressed fracture, which induces thermal contraction and alters fracture compliance during reopening and closure.

Table 7.4. The results of injection/falloff cycles in Phase 2 of Experiment 1.

Cycle #	Injection rate, ml/min	Peak pressure, psi	Reopening pressure, psi	ISIP, psi	Closure pressure, psi		Cumulative heat loss, J
					Tangent method	Compliance method	
1	40	1700	1010	1130	1130	/	2040
2		1661	992	1026	1135	/	2597
3		1629	937	1005	1107	/	3049
4		1600	882	978	1079	/	3443
5		1581	804	945	1044	/	3733
6		1586	795	911	1020	/	4112
7		1565	723	895	994	/	4477
8		1552	741	888	989	/	4812
9		1542	763	859	970	/	5055

"/" indicates the lack of a signature for stress determination through the "compliance" method.

The injection of cold fluid into a hot and stressed fracture system induces a significant cooling effect, leading to thermal contraction in the surrounding rock, particularly near the fracture surfaces. This contraction results in localized reductions in the normal stress acting across the fracture, effectively lowering the mechanical resistance to fracture reopening and closure. As a result, the fracture becomes more compliant, and lower injection pressures are required to reopen it. Figures 7.14(a) and 7.14(b) clearly illustrate that both the peak injection pressure and the fracture reopening pressure decrease systematically with increasing cumulative heat loss. The rapid temperature drop from cold water injection generates thermal stress gradients, which reduces the magnitude of compressive stress normal to the fracture. This reduction in compressive stress weakens the mechanical forces that previously kept the fracture closed, leading to progressively lower reopening pressures. Similarly, Figures 7.14(c) and 7.14(d) show that both the ISIP and closure pressure also decrease with increasing cumulative heat loss, following well-defined power-law trends. These results confirm that thermal contraction lowers the stress thresholds associated with both fracture reopening and closure, underscoring the critical role of thermal effects in interpreting hydraulic stress measurements under EGS-relevant conditions.

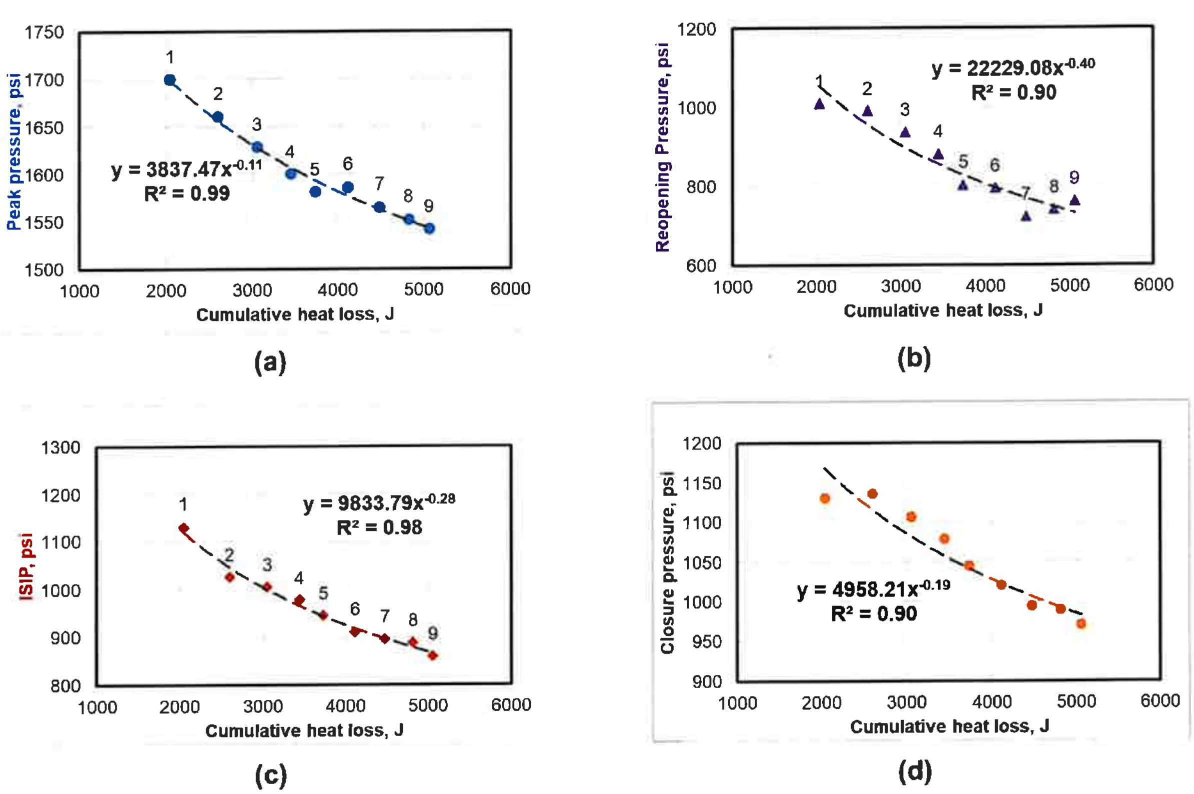

Figure 7.14. The relationship between pressure indicators and cumulative heat loss during high temperature DFIT tests of a cuboid Scioto Sandstone. (a) peak injection pressure vs. cumulative heat loss; (b) fracture reopening pressure vs. cumulative heat loss; (c) *ISIP* vs. cumulative heat loss; (d) fracture closure pressure vs. cumulative heat loss.

8. Conclusions and Recommendations

8.1. Summary of Key Findings

The poroelastic behavior of Utah FORGE granitoid demonstrates notable sensitivity to both effective stress and temperature, especially key parameters such as Biot's coefficient (α), Skempton's B, and permeability. Biot's effective stress coefficient, α, was observed to consistently decrease with increasing effective stress, reflecting the progressive closure of microcracks and reduced deformability of the pore structure. At lower temperatures (22°C to 90°C), α displayed a more pronounced stress dependence, with values ranging from high to moderate depending on the sample. However, at elevated temperatures (140°C and above), α not only dropped to lower values but also exhibited minimal sensitivity to stress. This behavior suggests that many pore spaces had become effectively isolated and/or sealed, possibly due to thermal sealing of micro-fissures, and that the rock behaved more like a dense, intact matrix. The use of two methods for the determination of α—based on the bulk modulus ratio (1 – K/Ks) and the poroelastic expansion coefficient (K/H)—produced consistent results, reinforcing the reliability of the observations.

Skempton's pore pressure coefficient, B, which measures the pore pressure response under undrained loading, showed a clear decreasing trend with both rising effective stress and temperature. Under isotropic loading, B values dropped significantly as microcracks closed and the rock matrix stiffened, limiting the rock's ability to generate pore pressure in response to external stress. At higher effective stresses, this decline became less steep, indicating that most compliant pore space had already collapsed. Temperature further amplified this effect: as samples were heated from room temperature to as high as 180°C, B values declined steadily. The thermal expansion of mineral grains is believed to tighten the microstructure, reduce crack apertures, and eliminate void connectivity, resulting in a diminished fluid pressure response. Despite careful saturation procedures—including long-duration water saturation and high back pressure to dissolve any residual air—subtle variations in microstructure (such as grain boundary characteristics and mineral alignment) contributed to sample-to-sample variability in B, especially under high stress or temperature conditions.

Permeability measurements further confirmed the rock's strong sensitivity to both mechanical and thermal influences. At room temperature, permeability decreased exponentially with increasing confining pressure, consistent with the closure of pre-existing fractures and pores. Under reservoir-relevant stress conditions (20–30 MPa effective stress), samples A, C, and D generally exhibited permeabilities in the 10 to 50 micro-Darcy range, while Sample B showed substantially lower values, in the nano-Darcy range, reflecting a tighter rock matrix. When temperature was increased under constant effective stress, permeability tended to decrease, especially up to 120°C, due to thermally induced closure of fissures. Interestingly, some samples (notably A and D) showed a slight rebound in permeability at temperatures beyond 140°C, possibly due to the initiation of new thermal cracks or reconfiguration of pore pathways. This nuanced behavior highlights the complex interplay between thermal expansion, microstructural evolution, and pore connectivity in low-porosity crystalline rocks.

In fractured granitoid samples, Skempton's B behavior becomes more complex. The rock is conceptualized as a dual-porosity system consisting of a compliant fracture network and a stiff rock matrix. These two domains respond differently to confining pressure changes: fractures, being much more compliant, experience a significantly higher pore pressure increase under undrained loading than the matrix. At low effective stresses, the fluid pressures in both domains tend to equilibrate due to open connectivity and minimal resistance to fluid exchange, resulting in a more unified response for the Skempton's B measurement. However, as stress increases, the pressure response may begin to diverge. The fracture domain, being more compressible, shows a disproportionately larger pressure rise, while the matrix remains relatively unresponsive. This divergence reflects the strong heterogeneity in pore compressibility across the two domains. In some cases, Skempton's B value can appear extremely high and well above 1, as it disproportionately captures the compliant domain's response. Conversely, a matrix-dominated signal would show a much lower B value. At very high temperatures, thermal overclosure can significantly reduce or even seal fracture apertures, leading to a dramatic loss of fracture porosity and permeability. In such cases, the matrix—though initially less permeable—may become the dominant flow and pressure-transmitting domain, effectively reversing the initial dual-porosity dynamics. This transformation under high-temperature, high-stress conditions highlights the importance of considering evolving microstructure and pore network architecture when interpreting Skempton's B in thermally and mechanically stressed fractured crystalline rocks.

It is also important to recognize that Skempton's B is inherently time-dependent, particularly in low-permeability and dual-porosity systems such as fractured granitoids—an effect that becomes even more pronounced when temperature is involved. Upon the application of confining pressure under undrained conditions, the initial pore pressure response (often referred to as the instantaneous or elastic B) may not reflect the true equilibrium value, especially when fluid exchange between the fracture network and the rock matrix is slow. The fracture domain, being more permeable, typically responds rapidly to stress changes, while the matrix, characterized by its tight structure and lower hydraulic diffusivity, adjusts more gradually. This mismatch leads to a transient period in which pore pressure continues to redistribute internally. With increasing temperature, the reduction in fluid viscosity can enhance pressure equilibration; however, this may be counteracted by thermal closure of fractures, which restricts flow between domains. As a result, Skempton's B should not be viewed as a purely static, elastic, or intrinsic material constant, but rather as a dynamic parameter governed by the evolving interplay between pore structure, fluid flow, and measurement time scale under changing thermal and mechanical conditions.

To address some fundamental questions and methodological uncertainties associated with current methods for analyzing fracture closure during hydraulic fracturing stress measurements, we conducted a series of controlled laboratory injection/fall-off experiments under both room-temperature and high-temperature conditions. These experiments were performed across various rock types with distinct mechanical and hydraulic properties and employed different injection fluids to capture a wide range of fracture behaviors. Our laboratory results successfully replicate the behavioral feature frequently noted during fracture closure analysis in field-scale hydraulic fracturing tests, including non-ideal leakoff and the underestimation of minimum principal stress by the "tangent" method, as well as the lack of consistent signatures for determining fracture closure via the "compliance" method.

The experimental results were used to investigate the physical process of fracture closure during shut-in. Our findings show that fracture closure during shut-in follows a three-stage process. Initially, in Stage 1, the fracture closes in a "hinge-like" manner, where the fracture width decreases while the fracture radius remains constant, indicating that no contact between the fracture surfaces at this stage. In Stage 2, fracture closure progresses from the fracture tip towards the wellbore in a "zipper-like" manner. Finally, in Stage 3, the fracture reaches full hydraulic closure, with fluid predominantly leaking through the wellbore wall. The wellbore pressure at the end of Stage 1 or the onset of Stage 2, marks the initiation of mechanical fracture closure and provides a reliable estimate of the minimum principal stress. This is because fracture closure begins when the fluid pressure within the fracture drops to a level equal to the external stress acting perpendicular to it. During Stage 1 and Stage 2, the pressure decline rate, (dP/dG), is governed by two competing mechanisms: (1) the increase in fracture stiffness (S_f), which causes dP/dG to increase, and (2) the decrease in the leakoff rate $q_L(G)$, which causes dP/dG to decrease. The net changes of pressure decline rate, governed by the complex competing process, determine the characteristics of G-function plots, resulting in various possible shapes and features of these plots, as illustrated in our experimental study.

Based on the insights gained from our experimental work, we propose using an early slope change on a dP/dG vs. G curve that deviates from a linear trend as a roust method for fracture closure identification. This approach effectively captures the competing effects of stiffness change and leakoff rate change on the evolution of pressure decline during fracture closure, providing a theoretically sound and practically viable solution for determining fracture closure pressure. The early slope deviation on a dP/dG vs. G curve reflects the onset of mechanical fracture closure, which theoretically offers the most reliable estimate of the minimum principal stress. Our experimental validation, along with successful testing in several field-scale hydraulic fracturing stress measurements, has demonstrated that this method yields consistent and accurate stress estimates. Furthermore, our experimental findings suggest that instantaneous shut-in pressure (ISIP) could provide reasonable, albeit higher bound, estimates of the minimum principal stress suggesting integration of closure pressure and ISIP for more accurate stress measurements across diverse geological settings.

Lastly, our high-temperature DFIT experiments provide important insights into the cooling effects on fracture behavior and stress interpretation under conditions relevant to EGS. By injecting cold fluids into heated, stressed rock samples, we observed consistent reductions in key pressure indicators, including peak injection pressure, fracture reopening pressure, ISIP, and closure pressure, as cumulative heat loss increased. These reductions followed a strong power-law relationship, indicating a direct link between thermal contraction and fracture aperture during HF-based stress measurements. Notably, the magnitude of the cooling effect was more pronounced in low-permeability granite than in high-permeability sandstone, likely due to differences in thermal conductivity, fluid leakoff behavior, and rock stiffness. These findings underscore the critical need to account for thermal effects, particularly in high-temperature environments like EGS reservoirs, when interpreting fracture closure and stress from DFIT data. Failure to do so could lead to significant underestimation of the minimum principal stress.

8.2. Application to Geothermal Energy Development

The characterization of poroelastic properties—particularly Biot's effective stress coefficient (α), Skempton's pore pressure coefficient, B, and permeability—in Utah FORGE granitoid provides critical insights for the design and optimization of enhanced geothermal systems (EGS). These properties govern how the reservoir rock responds to fluid injection, thermal loading, and stress redistribution, all of which are central to sustaining heat extraction and minimizing induced seismicity risks. The observed sensitivity of α and B to both effective stress and temperature highlights the importance of accounting for evolving reservoir conditions over the life of a geothermal project.

The findings show that Biot's coefficient (α) decreases with increasing effective stress and temperature, reflecting a transition from a micro-fractured, compliant structure to a more intact, stiff matrix. This behavior implies that under typical reservoir depths and thermal stimulation conditions, the rock mass becomes less responsive to pore pressure changes, potentially reducing the efficiency of hydraulic stimulation. However, this same stiffening effect can enhance long-term reservoir stability, especially if fracture apertures are thermally sealed and fluid flow is confined to well-connected zones. Understanding the spatial and temporal variability of α is therefore vital for calibrating coupled thermal-hydro-mechanical (THM) models used to simulate reservoir performance.

The time- and temperature-dependent nature of Skempton's B coefficient further supports the need for dynamic reservoir modeling. Skempton's B values decline with both increasing confining pressure and temperature, especially as microfractures close or become isolated from the main pore network. In fractured systems, dual-porosity behavior introduces complexity: at low stress, the fracture domain dominates the pore pressure response, but at higher stress and temperature, thermal overclosure may invert the flow hierarchy, making the matrix the primary storage and transmission domain. This has direct implications for pressure management and fracture reactivation potential, especially during cyclic injection or long-term thermal drawdown. Accurate interpretation of B under varying thermal and mechanical conditions enables better prediction of reservoir pressure evolution and the risk of fault slip or induced seismicity.

Permeability—the most direct control on fluid and heat transport—exhibits a strong dependence on both effective stress and temperature. Experimental results indicate that permeability in Utah FORGE granitoids generally decreases with increasing stress due to fissure closure, and with increasing temperature up to a threshold (~120°C~150°C), beyond which minor increases may occur due to thermally induced microcracking. This nuanced response underlines the importance of stimulation strategy design: thermal stimulation alone may not suffice to enhance reservoir permeability if thermal overclosure dominates; hydraulic or hybrid stimulation may be required to reopen or propagate fractures. The *Thermal Kaiser Effect*, documented in this study, reveals that prior thermal and mechanical loading history can suppress acoustic emission during reheating, suggesting stress memory effects that may influence the rock's fracture reactivation potential during repeated thermal cycling.

Together, these findings reinforce that geothermal reservoir performance cannot be understood through static parameters alone. Instead, a fully coupled, time-evolving understanding of thermo-poroelastic behavior is required—one that integrates changes in α, B, and permeability under in-situ stress and temperature conditions. Such knowledge enables more accurate forecasting of reservoir stimulation effectiveness, sustainable heat extraction, and safe long-term operation of EGS sites like Utah FORGE. These insights can also inform well placement, injection strategy, and long-term monitoring protocols to ensure both energy efficiency and geo-mechanical stability.

Results from the high-temperature DFIT experiments conducted on both the low-permeability Sierra White Granite and the high-permeability Scioto Sandstone clearly show that key pressure indicators, including peak injection pressure, fracture reopening pressure, ISIP, and fracture closure pressure, tend to decrease progressively with continued cold fluid injection. These reductions correlate strongly with the cumulative heat loss and can be effectively described using power-law relationships. Notably, the magnitude of the cooling effect appears to be more significant in the low-permeability granite compared to the sandstone. In the granite test, the peak injection pressure dropped by more than 900 psi, whereas in the sandstone test, the peak pressure decreased by less than 200 psi over a similar cumulative heat loss range. This difference can be attributed to two primary factors: (1) in the high-permeability sandstone, the cold fluid likely infiltrated the surrounding pore space more readily, dispersing heat quickly and reducing localized thermal contraction near the fracture; and (2) the mechanical stiffness of sandstone is lower than that of granite, which reduces the magnitude of thermoelastic strain and, consequently, the degree of stress alteration due to cooling. These results reinforce the importance of accounting for thermal contraction due to cold fluid injection when interpreting stress from DFITs under EGS-relevant conditions. Failure to consider cooling-induced pressure reductions may lead to systematic underestimation of the minimum principal stress, especially in thermally and mechanically stiff formations such as crystalline granites.

However, it is essential to consider the scaling implications and limitations of the experimental setup when translating these findings to field-scale EGS applications. In our laboratory experiments, the injected fluid volume is relatively large compared to the fracture volume and the immediate rock mass, and the injected fluid remains cold throughout the cycle. In contrast, in field scenarios, the injected fluid is likely to be preheated more while traveling down the wellbore and the fracture, limiting the effective thermal contrast on the entire fracture face. Moreover, when the volume of injected fluid relative to the thermal mass of the surrounding rock is much smaller, less significant thermal contraction is expected. Additionally, the reservoir scale thermal expansion coefficient is likely smaller than that of intact rock since small cracks can accommodate volumetric changes, and thermal stress is known to evolve slowly (Ghassemi and Zhang, 2006) so that its full impact could be smaller. Therefore, the magnitude of pressure reductions observed here should be considered an upper bound and larger than that in the field-scale DFIT tests, depending on the number of injection cycles and shut-in times.

8.3. Future Research Recommendations

Despite significant progress in understanding the thermo-poroelastic behavior of Utah FORGE granitoids, the study of dual-porosity rock systems—particularly under elevated temperature and stress conditions—remains in its early stages. Future research should aim to develop experimental methodologies specifically tailored for dual-porosity materials, where fractures and matrix domains can be characterized simultaneously or independently. This includes real-time monitoring of pressure evolution in both domains, spatially resolved imaging of microstructural evolution under load, and the use of tracer tests or acoustic sensors to capture inter-domain fluid communication. Establishing a quantitative framework for fracture-matrix pressure equilibration dynamics will be critical for improving models of fluid flow, heat transfer, and induced seismicity in enhanced geothermal systems.

Another key avenue for future research is the viscoelastic behavior of Skempton's B coefficient. Traditionally, B has been interpreted as an elastic parameter, assuming instantaneous and uniform pore pressure response under undrained loading. However, evidence from these and other experiments suggests that B is time-, rate-, and temperature dependent, particularly in low-permeability, fractured, or thermally stressed rocks. This indicates a viscoelastic component in the pore pressure response—one that may involve both fluid pressure diffusion and matrix time-dependent deformation. Investigating B as a function of strain rate, saturation pathway, and stress history opens a new research space at the intersection of poromechanical, rock physics, and rheology. Coupling these insights with microscale imaging techniques—such as X-ray micro-computed tomography (micro-CT), scanning electron microscopy (SEM) for pore structure, and NMR (Nuclear Magnetic Resonance) for pore-fluid dynamics—could yield new constitutive models that more accurately represent the complex behavior of geothermal reservoir rocks under in-situ thermal and mechanical conditions. While micro-CT and SEM offer high-resolution structural imaging, NMR provides direct information on pore size distribution, fluid saturation, and mobility, making it especially valuable for quantifying the fracture-matrix interactions in dual-porosity systems.

The Thermal Kaiser Effect, recently observed in FORGE granitoids, presents another underexplored frontier. The apparent memory of prior thermal and mechanical loading—evident in the suppression of acoustic emissions upon reheating—suggests that geothermal rocks may undergo history-dependent damage evolution. Understanding how this phenomenon influences fracture reactivation, permeability evolution, and seismic response under cyclic thermal operations is crucial for the long-term sustainability of geothermal energy extraction. Future studies could explore the thresholds for Kaiser effect manifestation under different temperature gradients, confining pressures, and rock types. Experimental results could be used to refine numerical models that simulate thermal fatigue, stress memory, and damage accumulation in geothermal reservoirs over decades of operation.

In addition, the role of chemical-thermal-mechanical coupling in reservoir evolution deserves deeper investigation. At high temperatures and pressures, fluid-rock interactions can alter mineralogy, clog or open pores, and affect mechanical strength. Long-term exposure to hot fluid may also lead to the chemical sealing of fractures or mineral precipitation, permanently altering reservoir flow paths. Laboratory experiments should simulate these reactive transport processes under realistic geothermal conditions, with attention to mineral stability, dissolution kinetics, and their feedback to poroelastic behavior.

From a modeling perspective, there is a growing need for multi-scale, coupled THMC (Thermo-Hydro-Mechanical-Chemical) simulations that can incorporate experimental observations of dual-porosity, viscoelastic B behavior, and the thermal Kaiser effect. This requires new constitutive models and numerical algorithms capable of resolving domain-specific responses within the same rock body—e.g., matrix deformation versus fracture slip. Incorporating history-dependent effects and non-elastic behavior into standard poroelastic frameworks could significantly enhance our predictive capability for geothermal stimulation and long-term performance.

Finally, instrumentation advancements will be pivotal. Future work should focus on developing high-temperature sensors and lab-based testing system components capable of functioning at high temperatures and pressures.

9. Acknowledgements

The principal Investigator would like to thank Drs. Zhi Ye, and Xue Jun Zhou for their contributions.

10. References

1. Aleinikoff, J.N., Nielson, D.L., Hedge, C.E., and Evans, S.H. 1987. Geochronology of Precambrian and Tertiary rocks in the Mineral Mountains, south-central Utah. US Geological Survey Bulletin, 1622, 1-12.
2. Allis, R., Gwynn, M., Hardwick, C., Hurlbut, W., Kirby, S.M., and Moore, J.N. 2019. Thermal characteristics of the Roosevelt Hot Springs system, with focus on the FORGE EGS site, Milford, Utah. In Allis, R., and Moore, J.N. (eds.), Geothermal characteristics of the Roosevelt Hot Springs system and adjacent FORGE EGS site, Milford, Utah. Utah Geological Survey Miscellaneous Publication 169-D, 22 p. https://doi.org/10.34191/MP-169-D.
3. Bear, J., Corapcioglu, M.Y. 1981. A mathematical model for consolidation in a thermoelastic aquifer due to hot water injection or pumping. Water Resources Research, 17(3), 723–736.
4. Bear, J., Sorek, S., Ben-Dor, G., Mazor, G. 1992. Displacement waves in saturated thermoelastic porous media, I: Basic equations. Fluid Dynamics Research, 9(4), 155–164.
5. Biot, M.A. 1941. General theory of three-dimensional consolidation. Journal of Applied Physics, 12(2), 155–164.
6. Biot, M.A., Willis, D.G. 1957. The elastic coefficients of the theory of consolidation. Journal of Applied Mechanics, 24(1), 91–96.
7. Crouch, S.L. and Starfield, A.M. 1981. Boundary Element Methods in Solid Mechanics. London: Allen & Unwin.
8. Brown, R.J.S., Korringa, J. 1975. On the dependence of the elastic properties of a porous rock on the compressibility of the pore fluid. Geophysics, 40, 608–616.
9. Browning, J., Meredith, P., Gudmundsson, A. 2016. Cooling-dominated cracking in thermally stressed volcanic rocks. Geophysical Research Letters, 43(16), 8425. https://doi.org/10.1002/2016GL070532.
10. Bu, M., Guo, P., Jin, X., Wang, M., Zhang, P., Wang, J. 2024. Temperature-dependent acoustic emission characteristics and statistical constitutive model of granite under uniaxial compression. Journal of Rock Mechanics and Geotechnical Engineering. https://doi.org/10.1016/j.jrmge.2024.05.033.
11. Chen, S., Yang, C., Wang, G. 2017. Evolution of thermal damage and permeability of Beishan granite. Applied Thermal Engineering, 110, 1533–1542. https://doi.org/10.1016/j.applthermaleng.2016.09.075.
12. Cheng, A.H.-D. 2016. Poroelasticity: Theory and Applications of Transport in Porous Media. Springer, Berlin, 877 p.
13. Coleman, D.S., Walker, J.D. 1992. Evidence for the generation of juvenile granitic crust during continental extension, Mineral Mountains Batholith, Utah. Journal of Geophysical Research, 97(B7), 11011–11024.
14. Darot, M., Gueguen, Y., Baratin, M.L. 1992. Permeability of thermally cracked granite. Geophysical Research Letters, 19(9), 869–872.

15. David, C., Menéndez, B., Darot, M. 1999. Influence of stress-induced and thermal cracking on physical properties and microstructure of La Peyratte granite. International Journal of Rock Mechanics and Mining Sciences, 36(4), 433–448. https://doi.org/10.1016/S0148-9062(99)00010-8.
16. Daoud, A., Browning, J., Meredith, P.G., Mitchell, T.M. 2020. Microstructural controls on thermal crack damage and the presence of a temperature-memory effect during cyclic thermal stressing of rocks. Geophysical Research Letters, 47, e2020GL088693. https://doi.org/10.1029/2020GL088693.
17. Di Drill Survey Services, 2021. Utah FORGE: Wells Updated Temperature and Pressure Logs (June 2021) [data set]. https://dx.doi.org/10.15121/1812334.
18. Dwivedi, R.D., Goel, R.K., Prasad, V.V.R., Sinha, A. 2008. Thermo-mechanical properties of Indian and other granites. International Journal of Rock Mechanics and Mining Sciences, 45(3), 303–315. https://doi.org/10.1016/j.ijrmms.2007.05.008.
19. Fortin, J., Stanchits, S., Dresen, G., Guéguen, Y. 2006. Acoustic emission and velocities associated with the formation of compaction bands in sandstone. Journal of Geophysical Research, 111(B10), B10203. https://doi.org/10.1029/2005JB003854.
20. Fredrich, J.T., Wong, T.F., 1986. Micromechanics of thermally induced cracking in three crustal rocks. JGR Solid Earth, 91(B12), 12743–12764. https://doi.org/10.1029/JB091iB12p12743.
21. Gassmann, F. 1951. Über die Elastizität poröser Medien (On the elasticity of porous media). Vierteljahrsschrift der Naturforschenden Gesellschaft in Zürich, 96, 1–23.
22. Ge, Z., Sun, Q. 2018. Acoustic emission (AE) characteristics of granite after heating and cooling cycles. Engineering Fracture Mechanics, 200, 418–429. https://doi.org/10.1016/j.engfracmech.2018.08.011.
23. Ghassemi, A. 2012. A review of some rock mechanics issues in geothermal reservoir development. Geotechnical and Geological Engineering J., 10706, Article No. 9508
24. Ghassemi, A and Zhou, X. 2011. A Three-Dimensional Thermo-Poroelastic Model for Fracture Response to Injection/Extraction in Enhanced Geothermal Systems. Geothermics.
25. Ghassemi, A and Tao, Q. 2016. Thermo-poroelastic effects on reservoir seismicity and permeability change. Geothermics Special Issue on EGS. doi:10.1016/j.geothermics.2016.02.006.
26. Ghabezloo, S., Sulem, J. 2009. Stress-dependent thermal pressurization of a fluid-saturated rock. Rock Mechanics and Rock Engineering, 42, 1–24.
27. Gringarten, A.C., Witherspoon, P.A., Ohnishi, Y. 1975. Theory of heat extraction from fractured hot dry rock. JGR, 80(8), 1120–1124. https://doi.org/10.1029/JB080i008p01120.
28. Griffiths, L., Heap, M.J., Baud, P., Schmittbuhl, J. 2017. Quantification of microcrack characteristics and implications for stiffness and strength of granite. International Journal of Rock Mechanics and Mining Sciences, 100, 138–150. https://doi.org/10.1016/j.ijrmms.2017.10.013.
29. Griffiths, L., Heap, M.J., Lengliné, O., Baud, P., Schmittbuhl, J., Gilg, H.A. 2024. Thermal stressing of volcanic rock: Microcracking and crack closure monitored through acoustic emission, ultrasonic velocity, and thermal expansion. JGR, 129, e2023JB027766. https://doi.org/10.1029/2023JB027766.
30. Griffiths, L., Lengliné, O., Heap, M.J., Baud, P., Schmittbuhl, J., 2018. Thermal cracking in Westerly Granite monitored using direct wave velocity, coda wave interferometry, and acoustic emissions. Journal of Geophysical Research: Solid Earth, 123, 2246–2261. https://doi.org/10.1002/2017JB01519.
31. Handwerger, D.A., McLennan, J.D. 2019. Wireline log and borehole image interpretation for FORGE well 58-32, Beaver County, Utah, and integration with core data. In Allis, R., and Moore, J.N. (eds.), Geothermal characteristics of the Roosevelt Hot Springs system and adjacent FORGE EGS site, Milford, Utah. Utah Geological Survey Miscellaneous Publication 169-M, 7 p. https://doi.org/10.34191/MP-169-M.
32. Heap, M.J., Lavallée, Y., Petrakova, L., Baud, P., Reuschlé, T., Varley, N.R., Dingwell, D.B. 2014. Microstructural controls on the physical and mechanical properties of edifice-forming Andesites at Volcán de Colima, Mexico. JGR: Solid Earth, 119(4), 2963. https://doi.org/10.1002/2013JB010521.
33. Heuze, F.E. 1983. High-temperature mechanical, physical and thermal properties of granitic rocks—A review. International Journal of Rock Mechanics and Mining Sciences, 20(1), 3–10.

34. Homand-Etienne, F., Houpert, R. 1989. Thermally induced microcracking in granites: Characterization and analysis. Int. J. Rock Mech. and Min. Sci., 26(2), 125–134. https://doi.org/10.1016/0148-9062(89)90001-6.
35. Huang, K., Cheng, Q., Ghassemi, A., Bauer, A. 2019. Evaluation of shear slip in fractured rock using a 3D coupled thermo–poromechanical FEM. International Journal of Rock Mechanics and Mining Sciences, 120, 68–81.
36. Hayashi, K., & Haimson, B. C. 1991) Characteristics of shut-in curves in hydraulic fracturing stress measurements and determination of in situ minimum compressive stress. J. Geoph. Res.: Solid Earth, 96(B11), 18311-18321.
37. Hayashi, K., & Sakurai, I. 1989. Interpretation of hydraulic fracturing shut-in curves for tectonic stress measurements. In Int. J. Rock Mech. and Mining Sci. & Geomech. Abs. 26, No. 6, pp. 477-482.
38. Hickman, S. H., & Zoback, M. D. 1981. The interpretation of hydraulic fracturing pressure-time data for in situ stress determinations. In Workshop on Hydraulic Fracturing Rock Stress Measurements; National Academy Press: Washington, DC, USA (pp. 103-127).
39. Hu, L., & Ghassemi, A. 2020. Heat production from lab-scale enhanced geothermal systems in granite and gabbro. International Journal of Rock Mechanics and Mining Sciences, 126, 104205.
40. Barree, R. D., & Mukherjee, H. 1996. Determination of pressure dependent leakoff and its effect on fracture geometry. In the SPE Annual Technical Conference and Exhibition., Denver, Colorado, USA.
41. Bredehoeft, J. D., Wolff, R. G., Keys, W. S., & Shuter, E. 1976. Hydraulic fracturing to determine the regional in situ stress field, Piceance Basin, CO. Geological Soc. of America Bulletin, 87(2), 250-258.
42. Castillo, J. L. 1987. Modified fracture pressure decline analysis including pressure-dependent leakoff. In SPE/DOE Joint Symposium on Low Permeability Reservoirs, Denver, Colorado, USA.
43. Jin, P., Hu, Y., Shao, J., et al. 2019. Influence of different thermal cycling treatments on the physical, mechanical and transport properties of granite. Geothermics, 78, 118–128. https://doi.org/10.1016/j.geothermics.2018.12.008.
44. Johnson, B., Gangi, A.F., Handin, J.,1978. Thermal cracking of rock subjected to slow, uniform temperature changes. 19th US Symposium on Rock Mechanics (USRMS). American Rock Mechanics Association, Reno, Nevada.
45. Jones, C., Keaney, G., Meredith, P., Murrell, S. 1997. Acoustic emission and fluid permeability measurements on thermally cracked rocks. Physics and Chemistry of the Earth, 22(1), 13–17. https://doi.org/10.1016/S0079-1946(97)00071-2.
46. Jones, C., Simmons, S., Moore, J. 2024. Geology of the Utah Frontier Observatory for Research in Geothermal Energy (FORGE) Enhanced Geothermal System (EGS) Site. Geothermics, 122, 103054.
47. Jones, C.G., Moore, J.N., Simmons, S. 2019. Petrography of the Utah FORGE site and environs, Beaver County, Utah. In Allis, R., and Moore, J.N. (eds.), Geothermal characteristics of the Roosevelt Hot Springs system and adjacent FORGE EGS site, Milford, Utah. Utah Geological Survey Miscellaneous Publication 169-K, 23 p. https://doi.org/10.34191/MP-169-K.
48. Kurashige, M. 1989. A Thermoelastic Theory of Fluid-Filled Porous Materials. Int. J. Solids & Struct.
49. McTigue, D F. 1986. Thermoelastic Response of Fluid-Saturated Porous Rock. J. Geoph. Res: 9533-9542.
50. Kirby, S.M. 2019. Revised mapping of bedrock geology adjoining the Utah FORGE site. In Allis, R., and Moore, J.N. (eds.), Geothermal characteristics of the Roosevelt Hot Springs system and adjacent FORGE EGS site, Milford, Utah. Utah Geological Survey Miscellaneous Publication 169-A, 6 p. https://doi.org/10.34191/MP-169-A.
51. Knudsen, T., Kleber, E., Hiscock, A., Kirby, S.M. 2019. Quaternary geology of the Utah FORGE site and vicinity, Millard and Beaver Counties, Utah. In Allis, R., and Moore, J.N. (eds.), Geothermal characteristics of the Roosevelt Hot Springs system and adjacent FORGE EGS site, Milford, Utah. Utah Geological Survey Miscellaneous Publication 169-B, 21 p. https://doi.org/10.34191/MP-169-B.
52. Lin, W. 2002. Permanent strain of thermal expansion and thermally induced microcracking in Inada granite. JGR: Solid Earth, 107(B10), ECV-3. https://doi.org/10.1029/2001JB000648.

53. Lockner, D., Byerlee, J., Kuksenko, V., Ponomarev, A., Sidorin, A. 1991. Quasi-static fault growth and shear fracture energy in granite. Nature, 350(6313), 39–42.
54. McClure, M., Jung, H., Cramer, D., and Sharma, M. 2016. The fracture-compliance method for picking closure pressure from diagnostic fracture-injection tests. SPE Journal 21(4): 1321-1339.
55. McLennan, J. D., & Roegiers, J. C. 1981. Do instantaneous shut-in pressures accurately represent the minimum principal stress. In USGS Workshop on Hydraulic Fracturing Stress Measurements, Monterey, CA.
56. McTigue, D.F. 1986. Thermoelastic response of fluid-saturated porous rock. JGR, 91(B9), 9533–9542. https://doi.org/10.1029/JB091iB09p09533.
57. Moore, J., McLennan, J., Pankow, K., Simmons, S., Podgorney, R., Wannamaker, P., Jones, C., Rickard, W., Xing, P. 2020. The Utah Frontier Observatory for Research in Geothermal Energy (FORGE): A Laboratory for Characterizing, Creating and Sustaining Enhanced Geothermal Systems. 45th Workshop on Geothermal Reservoir Engineering, Stanford University. SGP-TR-216.
58. Nielson, D.L., Evans, S.H., Sibbett, B.S. 1986. Magmatic, structural, and hydrothermal evolution of the Mineral Mountains intrusive complex, Utah. Geol. Soc. Am. Bull., 97, 765–777.
59. Nolte, K. G. 1979. Determination of fracture parameters from fracturing pressure decline. In SPE Annual Technical Conference and Exhibition, Las Vegas, NV.
60. Nolte, K. G. 1991. Fracturing-pressure analysis for nonideal behavior. J. Pet. Tech., 43(02), 210-218.
61. Norris, A. 1992. On the correspondence between poroelasticity and thermoelasticity. J. Applied Physics, 71, 1138–1141.
62. Obert, L. 1977. The Microseismic Method: Discovery and Early History. Proceedings of the First Conference on Acoustic Emission/Microseismic Activity in Geologic Structures and Materials. Trans Tech Publications, Clausthal.
63. Raaen, A. M., Skomedal, E., et al. 2001. Stress determination from hydraulic fracturing tests: the system stiffness approach. Int. J. Rock Mech. and Min. Sci., 38(4): 529-541.
64. Reuschle, T., Haore, S.G., Darot, M. 2006. The effect of heating on the microstructural evolution of La Peyratte granite deduced from acoustic velocity measurements. Earth and Planetary Science Letters, 243(3–4), 692–700.
65. Rice, J.R., Cleary, M.P. 1976. Some basic stress diffusion solutions for fluid-saturated elastic media with compressible pore fluid. Reviews of Geophysics and Space Physics, 14(2), 227–241.
66. Rong, G., Peng, J., Cai, M., Yao, M., Zhou, C., Sha, S. 2018. Experimental investigation of thermal cycling effect on physical and mechanical properties of bedrocks in geothermal fields. Applied Thermal Engineering, 141, 174–185. https://doi.org/10.1016/j.applthermaleng.2018.05.126.
67. Safari, R. and Ghassemi, A. 2015. Three-dimensional thermo-poroelastic analysis of fracture network deformation and induced micro-seismicity in enhanced geothermal systems. Geothermics, 58, 1-14.
68. Scheidegger, A.E. 1974. The Physics of Flow Through Porous Media (3rd ed.). University of Toronto Press.
69. Tester, J.W., Drake, E.M., Richards, M. 2006. The Future of Geothermal Energy: Impact of Enhanced Geothermal Systems (EGS) on the United States in the 21st Century. MIT.
70. Tutti, F., Dubrovinsky, L.S., Nygren, M. 2000. High-temperature study and thermal expansion of phlogopite. Physics and Chemistry of Minerals, 27(9), 599–603. https://doi.org/10.1007/s002690000098.
71. Wang, F., Frühwirt, T., Konietzky, H. 2020. Influence of repeated heating on physical-mechanical properties and damage evolution of granite. Int. J. Rock Mech. and Min. Sci., 136, 104514. https://doi.org/10.1016/j.ijrmms.2020.104514.
72. Wang, H.F. 2000. Theory of Linear Poroelasticity with Applications to Geomechanics and Hydrogeology. Princeton University Press.
73. Wang, H.F. Bonner, B.P., Carlson, S.R., Kowallis, B.J., Heard, H.C., 1989. Thermal stress cracking in granite. JGR, 94, 1745–1758.

74. Wong, L.N.Y., Zhang, Y., Zhang, Y., Wu, Z. 2020. Rock strengthening or weakening upon heating in the mild temperature range? Engineering Geology, 272, 105619. https://doi.org/10.1016/j.enggeo.2020.105619.
75. Ye, Z., Fang, Y. Ghassemi, A., McLennan, J., 2022. A Preliminary Wellbore In-Situ Stress Model for Utah FORGE. 56th U.S. Rock Mechanics/Geomechanics Symposium. ARMA-2022-0272. https://doi.org/10.56952/ARMA-2022-0272.
76. Ye, Z., Ghassemi, A. 2018. Injection-induced shear slip and permeability enhancement in granite fractures. JGR: Solid Earth, 123, 24 p.
77. Ye, Z., Ghassemi, A. 2020. Heterogeneous fracture slip and aseismic-seismic transition in a triaxial injection test. Geophysical Research Letters, 47(14), e2020GL087739.
78. Ye, Z., Vachaparampil, A., Zhou, X., Ghassemi, A., Kneafsey, T. 2019. Failure behavior of the Poorman schist and its fractures from EGS Collab stimulation site. 44th Workshop on Geothermal Reservoir Engineering, Stanford. SGP-TR-214.
79. Yin, T., Li, X., Xia, K., Huang, S. 2012. Effect of thermal treatment on the dynamic fracture toughness of Laurentian granite. Rock Mechanics and Rock Engineering, 45(6), 1087–1094. https://doi.org/10.1007/s00603-012-0240-3.
80. Zhang, F., Zhang, Y., Hu, D., Shao, J. 2021. Modification of poroelastic properties in granite by heating–cooling treatment. Acta Geotechnica, 16, 2165–2173. https://doi.org/10.1007/s11440-021-01163-3.
81. Zhou, X., Ghassemi, A. 2017. Biot's Effective Stress Coefficient of Mudstone Source Rocks. 51st US Rock Mechanics/Geomechanics Symposium.
82. Zhou, X., Ghassemi, A. 2019. Biot's Effective Stress Coefficient Tensor Measurements on Mancos Shale. 53rd US Rock Mechanics/Geomechanics Symposium.
83. Zhou, X., Ghassemi, A. 2022. Experimental Determination of Poroelastic Properties of Utah FORGE Rocks. 56th US Rock Mechanics/Geomechanics Symposium.
84. Zhou, X., Ghassemi, A. 2024. Poroelastic Properties of Sierra White Granite. Rock Mechanics and Rock Engineering, 57, 7777–7793. https://doi.org/10.1007/s00603-024-03904-8.
85. Zhou, X., Vachaparampil, A. Ghassemi, A., 2015. A Combined Method to Measure Biot's Coefficient. 49th US Rock Mechanics/Geomechanics Symposium.

11. List of GDR datasets/reports

1. Utah FORGE 5-2615: Well 58-32 and 78-32 Poroelastic Properties. https://gdr.openei.org/submissions/1464
2. Utah FORGE 5-2615: Laboratory Data for Insights on Hydraulic Fracture Closure and Stress Measurement. https://gdr.openei.org/submissions/1615
3. Data on mechanical properties of rocks subjected to cyclic heating/cooling (URL In Process)
4. Data on volume expansion and thermal pore pressure coupling coefficient (URL: In Process)

12. List of Journal Publications & Conference Presentations

1. Ghassemi, A., Ye, Z. 2025. Thermo-poroelastic Effects on Wellbore Stability and Fracturing in EGS with Reference to Utah FORGE EGS. 59th ARMA. Santa FE, NM.
2. Zhou, X. Ghassemi, A. 2025. Dependence of the Poroelastic Properties of Utah FORGE Granitoids – Part I. 59th ARMA. Santa FE, NM.
3. Safari, R., Ghassemi, A. 2025. Development and application of 3D thermo-poroelastic fictitious stress boundary element method. Engineering Analysis with Boundary Elements, 179(A), 106327.
4. Ghassemi, A., Ye, Z., & Ratnayake, M. 2024. The Role of Thermo-poroelastic Effects on Drilling Induced Fractures in the Utah FORGE Well 16A (78)-32. Paper presented at 49th Workshop on Geothermal Reservoir Engineering.
5. Ye, Z., Ghassemi, A. 2024. Progressive Fracture Propagation and Seismic Response in Laboratory Hydraulic Fracturing Experiments. AGU.
6. Ye, Z., Ghassemi, A. 2024. The Role of thermo-poroelastic Effects on Transverse Fractures in the Utah FORGE Well 16-A. 49th Stanford Geothermal Workshop.
7. Ye, Z., Ghassemi, A. 2024. Analysis of the Stimulated Volume and Seismicity Migration in Utah FORGE Stimulations. GRC Transactions, V.48.
8. Zhou, X., Ghassemi, A. 2023. Poroelastic Properties of Sierra White Granite 8. Rock Mech. & Rock Eng. 57 (10). doi:10.1007/s00603-024-03904-8
9. Kumar, D., Ghassemi, A. 2023. 3D Modeling and Analysis of Utah FORGE Reservoir Stimulation. Unconventional Resources Technology Conference (URTeC).
10. Ghassemi, A., Kumar, D. 2023. Hydraulic Fracturing in Utah FORGE. 48th Workshop on Geothermal Reservoir Engineering (pp. 1-9). Stanford.
11. Kumar, D., Liu, B., & Ghassemi, A. 2023. 3D Modeling of the Utah Forge Reservoir Stimulation with Proppant Transport and Deposition. SPE Annual Technical Conference and Exhibition.
12. Kumar, D., Ghassemi, A., & Liu, B. 2023. 3D Modeling and Analysis of Utah FORGE Reservoir Stimulation. SPE/AAPG/SEG Unconventional Resources Technology Conference.
13. Zhou, X., Ghassemi, A. 2022. Experimental Determination of Poroelastic Properties of Utah FORGE Rocks. 56th US Rock Mechanics/Geomechanics Symposium.
14. Kumar, D., Ghassemi, A. 2022. Geomechanical controls on frac-hits. SPE International Hydraulic Fracturing Technology Conference & Exhibition.
15. Ratnayake, R and Ghassemi, A. 2022. The Role of Thermo-Poroelastic Effects in Utah FORGE Stimulation Experiments. GRC.
16. Ratnayake, R and Ghassemi, A. 2025. Where Is the Heart-shape Fiber Response? Impact of Poroelasticity on Strain and Frac Height Estimation. SPE Hydraulic Fracturing Technology Conference and Exhibition. SPE-223555-MS.
17. Ghassemi, A. and Ratnayake, R. 2025. Hydraulic Fracturing in Geothermal Reservoirs: The Utah FORGE EGS and Newberry Superhot Project. SPE Hydraulic Fracturing Technology Conference and Exhibition. SPE-223576-MS.